STRUCTURAL AND ELECTROCHEMICAL STUDIES OF NON-INTERCALATION TYPE ALTERNATIVE ANODE MATERIALS FOR LITHIUM-ION BATTERIES

A Thesis Submitted to the
Delhi Technological University
In fulfilment of the requirements for the degree of

DOCTOR OF PHILOSOPHY

in

APPLIED PHYSICS

by

SHIVANGI RAJPUT

(2K17/PHD/AP/16)

Under the Supervision of

Dr. Amrish K. Panwar
Assistant Professor
DTU

Prof. Amit Gupta
Professor
IIT Delhi

DEPARTMENT OF APPLIED PHYSICS

DELHI TECHNOLOGICAL UNIVERSITY

DELHI-110042, INDIA

JULY 2024

DECLARATION

This is to certify that the thesis entitled "***Structural and Electrochemical Studies of Non-intercalation Type Alternative Anode Materials for Li-ion Batteries***" submitted for the award of the degree of "**Doctor of Philosophy**" to Delhi Technological University India, embodies the original research work carried out by me under the supervision of Dr. Amrish K. Panwar, Department of Applied Physics, Delhi Technological University India and Prof Amit Gupta, Department of Mechanical Engineering, IIT Delhi. The results obtained in this thesis are original and have not been submitted to any other University or Institution for the award of any degree or diploma.

Date: 31/07/2024
Place: Delhi

Shivangi
31/07/2024
Shivangi Rajput

Registration No.: 2K17/PhD/AP/16

DELHI TECHNOLOGICAL UNIVERSITY

CERTIFICATE

This is to certify that the thesis entitled ***"Structural and Electrochemical Studies of Non-intercalation Type Alternative Anode Materials for Li-ion Batteries"*** with registration number **2K17/PhD/AP/16** being submitted by **Ms. Shivangi Rajput** to Delhi Technological University India, for the award of the degree of **"Doctor of Philosophy"** is based on the original research work under the supervision of Dr. Amrish K. Panwar and joint supervision of Prof. Amit Gupta, Department of Mechanical Engineering, IIT Delhi. It is further certified that the work embodied in this thesis has not been submitted partially or fully to any other University/Institution for the award of any degree or diploma.

Shivangi 31/07/2024

Shivangi Rajput

(Registration No.: 2K17/PhD/AP/16)

This is certified that the above statement made by the candidate is correct to the best of our knowledge.

31/07/2024

Dr. Amrish K. Panwar
(Supervisor)
Assistant Professor
Department of Applied Physics
Delhi Technological University
Delhi, India

Prof. Amit Gupta
(Joint Supervisor)
Professor
Department of Mechanical Engineering
IIT Delhi
Delhi, India

Rao 31/7/24

Prof. A.S. Rao
Head of Department
Department of Applied Physics
Delhi Technological University
Delhi, India

Dedicated to….

My beloved Family

ACKNOWLEDGEMENTS

My research journey has been greatly enriched by the invaluable support of many individuals. This work owes its essence to the academic, educational, psychological, and human support, as well as the belief in me as a writer and researcher, provided by the following people:

First and foremost, I would like to express my deepest gratitude to my supervisor, **Dr. Amrish K. Panwar**, for his timely guidance and encouragement throughout the research process. I am profoundly thankful for his patience, motivation, advice, and the invaluable time he dedicated to me during this period. Additionally, I am extremely grateful to my joint supervisor, **Prof. Amit Gupta**, for his invaluable suggestions and unwavering support during my research.

I am deeply grateful to **Prof. A.S. Rao**, **Head of the Department of Applied Physics** at DTU, for his support of my research and for providing an ideal working environment. My heartfelt appreciation goes to **Prof. S.C. Sharma, DRC Chairman**, and **Prof. Rinku Sharma**, former Head of the Department of Applied Physics and current Dean (PG) at DTU, for their valuable academic assistance and suggestions. I am also very thankful to all the faculty members of the Department of Applied Physics for their support and guidance. Additionally, I express my sincere gratitude to all non-teaching staff of the Department of Applied Physics for their cooperation and moral support throughout my research. I sincerely appreciate the support provided by the Lithium-ion Battery Lab at Delhi Technological University for offering the facilities necessary to conduct my research.

I gratefully acknowledge the kind support and continuous motivation from my seniors and colleagues **Dr. Abhishek Bhardwaj, Dr. Snigdha Sharma, Ms. Anchali Jain, Mr. Sharad Singh Jadaun, Mr. Rahul Kundra, Mr Deepak and Mr. Naveen** who helped me throughout my research work. I sincerely thank my dear friends **Mr. Rajat Gautam, Mrs. Konica Saxena, Mr. Ashish Singh** and **Mr. Devesh Yadav** for their support that helped in accomplishing my work.

I dedicate this thesis to my parents and family for their loving support, patience, and sacrifices that sustained me through both the best and the most challenging times. With heartfelt gratitude and love, I express my deepest appreciation to my father, **Mr. Shankar Lal Rajput**, and in loving memory of my late mother, **Mrs. Urmila Rajput**, for their unwavering encouragement and love throughout my life.

I would like to express my sincere gratitude to my husband **Mr. K P Shobhit** for his unwavering support, encouragement, and understanding throughout the duration of this research. His patience, love, and belief in me have been the cornerstone of my perseverance.

I am also deeply grateful to my in-laws, whose constant encouragement and support have been invaluable. Their belief in my abilities and their willingness to help in any way possible have been a source of strength and motivation.

Lastly, I extend my heartfelt gratitude to everyone who offered their help and support. Thank you immensely!

Date : 31/07/2024

Place : Delhi

Shivangi

Shivangi Rajput

ABSTRACT

As the global economy advances and populations expand, pressing issues like climate change and the rapid depletion of fossil fuel reserves have spurred considerable global interest in renewable energy storage solutions. Recently, Lithium-ion Batteries (LIBs) have surged in prominence within electronic and energy storage sectors due to their remarkable characteristics, including high energy density, minimal maintenance, negligible memory effect, and extremely low self-discharge rates. Moreover, LIBs have proven to be among the most effective methods for storing energy across a spectrum of applications, ranging from small portable devices like mobile phones and laptops to larger-scale systems such as digital electronics and electric vehicles. The electrode material plays a pivotal role in batteries, dictating the movement of charges and the storage of energy. Consequently, enhancing electrochemical performance hinges on optimizing the electrode material. Since the commercial introduction of LIBs in 1990-91, graphite has been the prevalent choice for anodes. However, its usage is hindered by drawbacks such as low gravimetric and volumetric capacity, along with safety concerns, rendering graphite unsuitable for the next generation of LIBs. Conversely, carbonaceous electrode materials exhibit low theoretical capacity and are insufficient on their own to meet contemporary power demands.

Hence, there is an urgent need to explore novel anode materials to enhance the storage capacity and safety of LIBs. Group IV elements such as Si, Ge, and Sn have emerged as promising candidates due to their superior specific capacities compared to carbon-based materials. Among these, Sn has garnered significant attention owing to its impressive theoretical capacity and safer thermodynamic potential when compared to carbon-based alternatives. Additionally, tin boasts a higher electrochemical potential compared to graphite, bolstering its security and reliability as an anode. Consequently, significant

research efforts have focused on tin-based anodes. However, commercialization remains elusive due to the substantial volume expansion during cycling, resulting in particle cracking and capacity degradation. To address these obstacles, diverse strategies have been implemented, such as nano structuring and the use of composite materials instead of pure metal. Nanosized anode materials offer a compelling solution by providing improved strain accommodation, leading to enhanced specific capacity and rate capability due to augmented interfacial area and accelerated kinetics of Li-ion diffusion. Tin readily forms binary or ternary compounds like Sn-M, Sn-M-M' by reacting with elements from groups VA and VI A elements. Consequently, one viable approach involves alloying tin with inert materials to mitigate volume expansion/shrinkage during charging or discharging, examples of which include Sn-Sb, Sn-Co, Sn-Ni, Sn-Cu, and similar alloys. Another strategy entails incorporating conductive materials like carbon, polypyrrole, or polyaniline into composites to enhance electrochemical performance.

Moreover, conversion-based transition metal oxides (TMOs) have undergone extensive investigation in recent years due to their excellent theoretical capacities (ranging from 600 to 1200 $mAhg^{-1}$). However, despite these promising attributes, TMOs have yet to be employed in commercial batteries due to issues such as capacity decay during cycling and inadequate conductivity. Consequently, there remains significant potential for further exploration of TMOs as anode materials for LIBs. Metal oxides with a binary composition ($A_xB_yO_z$, where A can be Zn, Mn, Fe, Co, Ni, or Cu; and B can be Zn, Mn, Fe, Co, Ni, or Cu) and operating via the conversion reaction mechanism possess two electrochemically active transition metal ions. These oxides exhibit promising electrochemical activity when used as anode materials for LIBs. When employed as anode in LIBs, AB_2O_4 type metal oxides are capable of delivering a very high theoretical specific capacity (nearly 1000 $mAhg^{-1}$). In recent times, there has been a notable focus on AB_2O_4 type transition metal oxides

(TMOs), owing to their attributes such as high energy density, environmental friendliness, and widespread availability Hence, the present research work mainly focuses on the synthesis, physicochemical and electrochemical analysis of tin-based alloy anodes and AB_2O_4 type transition metal oxides.

The research work conducted within this thesis demonstrates that the non-intercalation type alloy anode (SnSe) and conversion based TMOs anodes ($ZnFe_2O_4$, $CoFe_2O_4$ and $ZnCo_2O_4$) would be potential anodes when employed as an anode in Lithium-ion batteries. To perform the research work, low-cost and simple synthesis methods are employed to enhance the structural and morphological properties, resulting in stable and advanced anode materials with superior electrochemical performance. These newly developed anode materials have the potential to replace commercialized materials in lithium-ion batteries (LIBs)

The results of the current research work have been divided into seven chapters with the following brief details:

Chapter 1 introduces rechargeable batteries and provides an overview of Lithium-ion batteries (LIBs), along with an explanation of various types of anode materials investigated for use in LIBs. This chapter presents an extensive literature review focusing on non-intercalation types of anode materials, particularly alloy anodes and conversion-based anodes, proposed as alternative options for LIBs. Additionally, a succinct review comparing these materials and underscoring their advantages over other carbonaceous anode materials has been explored. Furthermore, the chapter delineates the objectives of the thesis, grounded in both current needs and the insights gleaned from the literature review.

Chapter 2 outlines the synthesis and experimental characterization techniques employed for the production of SnSe, AFe_2O_4 (A=Zn,Co) and $ZnCo_2O_4$ as well as their composites. Specifically, the sol-gel route, urea assisted combustion route and planetary ball milling

synthesis processes were primarily utilized for achieving pure phase of anode materials. This chapter provides concise details of experimental methodologies such as thermogravimetric analysis (TGA), X-ray diffraction (XRD), scanning electron microscopy/transmission electron microscopy/high-resolution transmission electron microscopy (SEM/TEM/HRTEM), Fourier-transform infrared spectroscopy (FTIR), DC conductivities, and Raman Spectroscopy. In addition, the cell fabrication and electrochemical measurement instruments used include an automatic coating unit, a calendaring machine, crimping machine in glove-box workstation for cell assembly, and an electrochemical analyser for cyclic voltammetry (CV), electrochemical impedance spectroscopy (EIS), and galvanostatic charge/discharge studies of the assembled coin cells.

Chapter 3 presents the physical and electrochemical studies for SnSe/C and SnSe/MWCNT composites effectively synthesized through a high-energy ball milling process utilizing Sn and Se metal powder, Super P, and MWCNT as precursors. XRD results confirm the proper phase formation of SnSe/C and SnSe/MWCNT as an orthorhombic structure with space group, pnma. The morphological analysis was conducted using FESEM and TEM to examine the shape, size, and distribution of particles. Additionally, Energy Dispersive Spectroscopy (EDS) and Raman spectroscopy were employed to validate the uniform mixing of SnSe with Super P and MWCNT. When utilized as anodes in Li-ion batteries, both SnSe/C and SnSe/MWCNT composites demonstrated superior reversible capacity, cycle life, and rate performance as compared to pure SnSe. Initial discharge capacities of 1069 $mAhg^{-1}$ and 1107 $mAhg^{-1}$ were achieved by SnSe/C and SnSe/MWCNT, respectively.

Chapter 4 reveals the effect of Mn doping on the physical and electrochemical properties of $ZnFe_2O_4$. $Zn_{1-x}Mn_xFe_2O_4$ (x = 0.0, 0.01, 0.03, 0.05) was synthesized through a straightforward and efficient high-energy ball milling process. Analysis via X-ray Diffraction (XRD) confirmed the highly crystalline nature with spinel structures across all

prepared samples, devoid of impurities except for x = 0.05, which exhibited a trace of α-Fe_2O_3. Morphological assessments conducted using SEM and TEM validated the shape and size of the prepared samples, with an average particle size ranging between 100 nm to 200 nm. Energy Dispersive Spectroscopy (EDS) analysis affirmed the uniform mixing of elements within the prepared samples. Electrochemical performance of the Mn-doped $ZnFe_2O_4$ was evaluated through Galvanostatic Charge-Discharge (GCD), Electrochemical Impedance Spectroscopy (EIS), and Cyclic Voltammetry (CV). The charge storage mechanisms, encompassing pseudocapacitive and diffusive contributions, were also investigated. Hence, the results demonstrated that the $Zn_{1-x}Mn_xFe_2O_4$ (x = 0.03) electrode exhibited superior electrochemical behavior as compared to other prepared electrodes. Specifically, $Zn_{1-x}Mn_xFe_2O_4$ (x = 0.03) showcased an initial charge-discharge capacity of 1405 $mAhg^{-1}$ and 900 $mAhg^{-1}$ with a coulombic efficiency of 64.2%. $Zn_{1-x}Mn_xFe_2O_4$ (x=0.03) sample maintained a discharge capacity of 502 $mAhg^{-1}$, with a capacity retention of 35%. after 200 cycles. Moreover, the rate capability of $Zn_{1-x}Mn_xFe_2O_4$ (x = 0.03) at a current density of 1000 mAg^{-1} was observed to be 434 $mAhg^{-1}$.

Chapter 5 deals with the synthesis of $ZnCo_2O_4$ via two different routes viz urea-assisted combustion method and ball milling method. The physicochemical characterization has been carried out with the help of XRD, FESEM, and EDX to confirm the phase, morphology, and elemental composition, respectively. The average crystallite size of $ZnCo_2O_4$ via urea-assisted combustion (ZCU) and the ball milled (ZCB) has been observed to be 57 nm and 70 nm as estimated from XRD. The average particle of $ZnCo_2O_4$ via urea combustion and the ball mill is 20 µm and 49 µm, respectively, as observed by FESEM. The diffusion coefficient calculated from EIS analysis for ZCB and ZCU has been estimated as 9.32 x $10^{-15}\ cm^2s^{-1}$ and 2.63 x $10^{-14}\ cm^2s^{-1}$, respectively.

Chapter 6 reveals the physical and electrochemical studies for CFO, CFO_MWCNT and CFO_rGO composites effectively synthesized through a sol gel auto combustion route. XRD results confirm the proper phase formation of CFO, CFO_MWCNT and CFO_rGO composites as inverse cubic spinel structure with space group, Fd3m. The morphological analysis was conducted using FESEM and TEM to examine the shape, size, and distribution of particles. Additionally, energy dispersive spectroscopy (EDS) and Raman spectroscopy were employed to validate the uniform mixing of CFO with rGO and MWCNT. When utilized as anodes in Li-ion batteries, both CFO_MWCNT and CFO_rGO composites demonstrated superior reversible capacity, cycle life, and rate performance compared to pure CFO. Initial discharge capacities of 1554 $mAhg^{-1}$ and 1314 $mAhg^{-1}$ were achieved for CFO_MWCNT and CFO_rGO, respectively. The Li-ion diffusion coefficient is calculated using EIS was found in the range of 0.26 $x10^{-17}$ cm^2s^{-1}, 0.95 $x10^{-17}$ cm^2s^{-1} and 1.00 $x10^{-15}$ cm^2s^{-1}, for CFO, CFO_MWCNT and CFO_rGO sample, respectively.

Chapter 7 encompasses the conclusion and summary of the research undertaken in this study. It outlines the findings of the optimized samples and discusses their implications. Additionally, this section delineates the potential avenues for future research based on the outcomes of the present investigation.

LIST OF PUBLICATIONS

- **Rajput Shivangi**, Panwar A.K., and Gupta Amit, "Study of Lithium diffusion properties and electrochemical performance of SnSe/C and SnSe/MWCNT composite anode for Li-ion Batteries", **Solid State Ionics**, 394, 116206. **(2023)**
- **Rajput Shivangi**, Panwar A.K., and Gupta Amit, **"**Impact of Synthesis Techniques on the Electrochemical Properties of $ZnCo_2O_4$ as Alternative Anode for Lithium-ion Batteries." **Indian Journal of Engineering and Material Sciences**, 30, 661-666 **(2023)**
- **Rajput Shivangi**, Panwar A.K., and Gupta Amit, "Facile Synthesis and Electrochemical Studies of Mn-Zn Ferrite as Anode for Li-ion Batteries." **Journal of Alloys and Compound**,976,173145 **(2024)**
- **Rajput Shivangi**, Jain Anchali, Jadaun S.S, Panwar A.K., Gupta Amit and Pastor Mukul, "Facile sol-gel auto-ignition synthesis of $CoFe_2O_4$/rGO and $CoFe_2O_4$/MWCNT as an alternative anode for Lithium-ion batteries." (To be Communicated)

Conference Attended

- Presented poster at "**International Meeting on Energy storage Devices, IMESD-2023**" on the topic, "Physical, Electrical and Electrochemical Studies of $Zn_{1-x}Mg_xFe_2O_4$ ($0 \leq x \leq 1.0$) prepared via solid state route as anode for Lithium-ion Batteries in IIT Roorkee, Uttarakhand.
- Oral presentation at "**International Conference on Advanced Materials for Emerging Technologies (ICAMET -2023)"** on the topic, "Impact of Synthesis Techniques on the Electrochemical Properties of $ZnCo_2O_4$ as Alternative Anode for Lithium-ion Batteries in NSUT, New Delhi.

- Presented poster at "**National Conference on Solid State Ionics, NCSSI-2019**" on the topic "Synthesis and electrochemical characterization of $ZnFe_2O_4$ as anode for LIB" in IIT Roorkee, Uttarakhand.
- Presented poster at "**International Conference on Atomic, Molecular, Optical, and Nano Physics, CAMNP-2019**" on the topic "Synthesis and Electrochemical characterization of $ZnCo_2O_4$ as anode for Lithium-ion batteries" at Delhi Technological University, Delhi.
- Presented poster at "**International Meeting on Energy storage Devices, IMESD-2018**" on the topic, "Development of novel ternary SnSb-ZnO nanocomposite as anode for Lithium-ion Batteries in IIT Roorkee, Uttarakhand.

Work not included in thesis

- **Rajput Shivangi**, Naveen, Jadaun S.S, Panwar A.K., Gupta Amit, and Singh Seema "Physical, Electrical and Electrochemical Studies of $Zn_{1-x}Mg_xFe_2O_4$ ($0 \leq x \leq 1.0$) prepared via solid state route as anode for Lithium-ion Batteries" (Communicated)
- **Rajput Shivangi** and Panwar A. K., **(2020),** Development of Novel Ternary SnSb-ZnO Nanocomposites as Alternative Anode Material for Lithium-Ion Batteries, published as a book chapter in **"Recent Research Trends in Energy Storage Devices: Select Papers from IMSED 2018"** Editors: Sharma, Y., Varma, G.D., Mukhopadhyay, A., Thangadurai, V., pp – 47-157, Publisher: Springer Nature.

List of Figures

List of Tables

Table of Contents

Chapter 1 : Introduction and Literature Review

This chapter provides an overview of Lithium-ion Batteries (LIBs) and the literature review on different types of anode materials. Chapter pertains the classification of various anode materials that have been investigated and developed by research. Among the developed anodes, tin-based alloy anode (SnSe) and AB_2O_4 type TMO's anode ($ZnFe_2O_4$, $CoFe_2O_4$, $ZnCo_2O_4$) are extensively explored as potential alternative anode material for the present study. The alternative anode materials for LIBs centres on achieving superior energy density, power density, and cycling performance. This pursuit aims to enhance the suitability of LIBs for various applications, including consumer electronics, communication devices, storage backup systems, and grid-scale battery storage systems.

1.1 Background

In the recent past, global energy economy is at stake due to the rapid consumption of fossil fuels in vehicles leading to the emission of toxic gases such as CO and CO_2. The continuous release of CO_2 gas has accelerated the global warming and eventually leading to the grievous changes in the climate system[1,2]. Thus, to reduce the emission of these harmful gases, utilization of green-energy sources such as wind, bioenergy, geothermal and solar energy is needed to replace the conventionally used fossil fuels [3,4]. It has been predicted that assuming the current rate of fossil fuel consumption, the energy demand will roughly be doubled by 2050. Hence, there is an utmost need of clean, sustainable, advanced and cost effective next generation energy storage devices[5,6]. In recent years, rechargeable batteries have proven themselves to be the most promising energy storage devices. Among all the different type of rechargeable batteries, Lithium-ion batteries (LIBs) are explored extensively to meet the increasing demand of electrochemical power devices for practical application like electric vehicles (EVs) and hybrid electric vehicles (HEVs). Hence, considerable research efforts are dedicated to comprehending and improving both the specific energy and long-term cycling stability[7,8]. LIBs are one of the most researched energy storage devices and used for various small to large applications viz. mobile phones, cameras, laptops, electric vehicles, aerospace and marines etc. owing to their superior electrochemical performance as compared to other energy storage devices[9–11].

1.2 History

The first ever battery was invented by Italian physicist Alessandro Volta in the year 1798. In this battery, the plates of zinc and copper metal were arranged in the form of a pile with brine-soaked cloth sandwiched between the plates which acted as the electrolyte. However, it had certain drawbacks such as short life span, electrolyte leakage and corrosion of zinc plates[12]. William Cruickshank of Scotland solved the leakage problem who proposed the

idea to lay the battery sideways, which led to invention of 'trough battery'. Short life span of this battery was due to the zinc degradation and build-up of hydrogen bubbles on copper[13,14]. Not many years later, John Fredrick Daniell invented a cell which eliminated the hydrogen bubble problem by using a second electrolyte and offered better voltage than Voltaic cell[15]. In 1836, John designed and devised Daniell cell. Hence, time to time, many more advancement took place in field of energy storage devices. In 1859, Gaston Planté, a French physicist, conceptualized the first rechargeable battery, known as the Lead-acid Battery. Until few years back, an improvised version of Lead Acid Battery is being used as Car Battery. With the gradual development, alkaline batteries came into existence. The increasing development in the field of energy storage devices leads to the requirement for high energy density and high-power density next generation rechargeable energy devices[16,17]. To fulfil these need Lithium-ion batteries came into existence, as the energy density and power delivered by LIBs are 2-3 times higher than that of other rechargeable Ni-Cd and Ni-MH batteries. The safety issue with the metallic lithium electrodes leads researchers and scientist to develop batteries using lithium compounds as electrodes. In 1974-76, Besenhard, discovered and proposed "the application of reversible intercalation in graphite and intercalation in cathodic oxides"[18,19]. In 1979, the Lithium-cobalt-oxide battery was discovered by John B. Goodenough. Initial rechargeable battery was made with $LiCoO_2$ as the positive electrode and lithium metal as the negative electrode. This development established the groundwork for the potential utilization of diverse and efficient electrode materials, eliminating the need for Lithium metal, as $LiCoO_2$ served as a supplier of Li-ions[20]. In the later years, various other compounds such as $LiMn_2O_4$, $LiMnO_3$, and $LiNiO_2$ were also investigated. In 1981, an experiment conducted by Samar Basu at Bell Labs showcased the intercalation of Li-ions into graphite, leading to the creation of the LiC_6 electrode[21]. In 1983, "John. B. Goodenough and co-workers" used the manganese spinel Mn_2O_4 as a cathode material for Li-ion batteries[22]. Akira Yoshino in the year 1995

developed a prototype cell with $LiCoO_2$ as the positive electrode and a carbon-based negative electrode[23]. Figure 1.1 shows the graph between volumetric and gravimetric energy of different batteries.

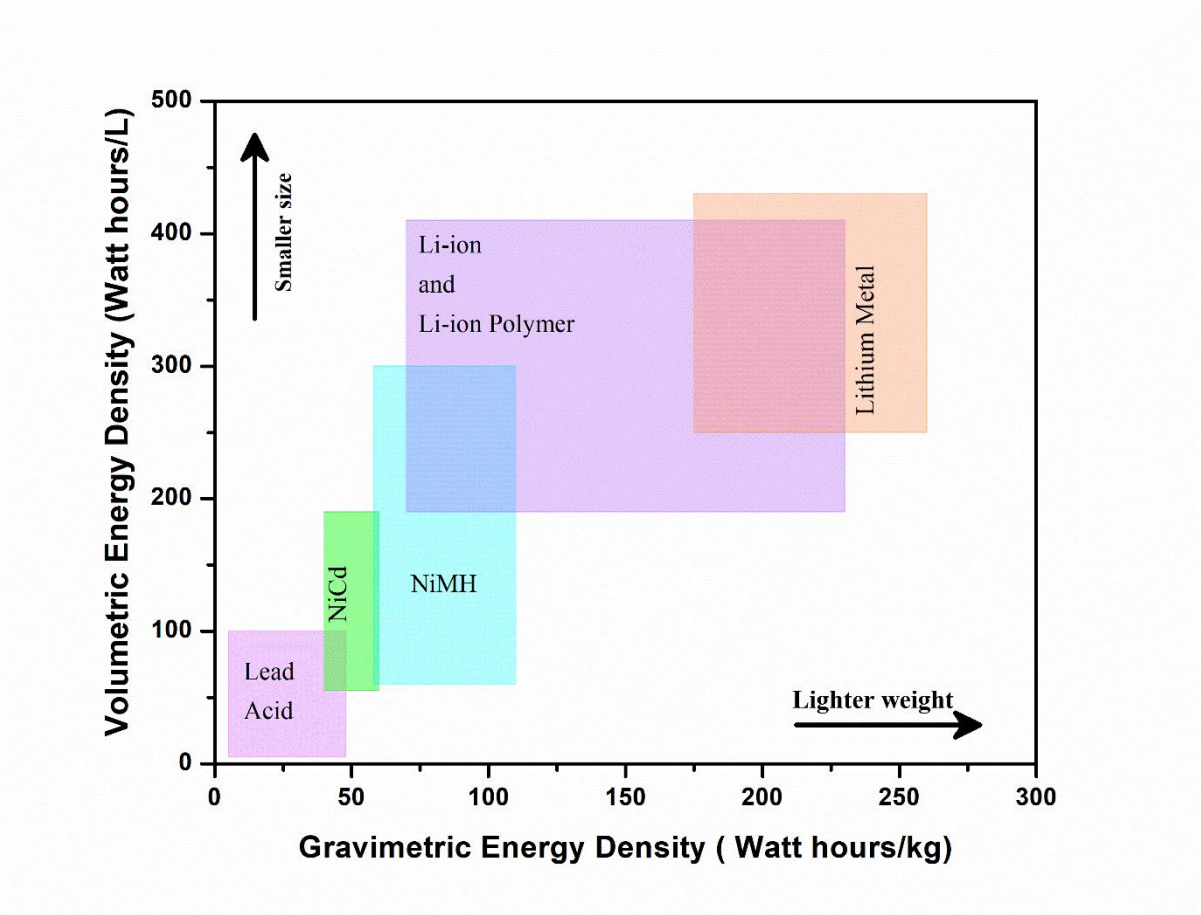

Figure 1.1 Graph between volumetric and gravimetric energy of different batteries [24].

1.3 Basics of Lithium-ion Batteries (LIBs)

A Li-ion cell is an electrochemical device that can produce energy via electrochemical reaction. A lithium-ion battery is manufactured by connecting Li-ion cells in parallel, series or both. Generally, a basic lithium-ion cell consists of four fundamental components viz. an anode, a cathode, electrolyte and separator. The electrodes (cathode and anode) are the charge carriers providing the electrochemical energy storage and release. The separator, functioning as a microporous membrane, facilitates the movement of Li-ions between the two electrodes while obstructing the flow of electrons, thus averting short circuits. The

electrolyte consists of ions (Li-ions). The cathode, serving as the positive electrode, contrasts with the anode, which acts as the negative electrode. The designation of cathode and anode is determined by the direction of the current flow[25,26]. Common commercially used cathodes are mainly lithium transition metal oxides or phosphates ($LiFePO_4$, $LiMn_2O_4$, $LiCoO_2$ etc) and at the anode side graphite is generally used[18,27–30]. While charging, Li-ions traverse from the cathode to the anode, traversing through the electrolyte and separator, before intercalating within the anode, transforming electrical energy into chemical energy. In contrast, during discharging, Li-ions travels back towards the cathode releasing chemical energy stored producing an electrical energy[31–33]. The schematic of working mechanism of LIB is shown in Fig. 1.2 using $LiCoO_2$ and graphite as cathode and anode, respectively. The electrochemical mechanism occurring in a LIB can be expressed as:

At cathode: $$Li_{1-x}CoO_2 + xLi^+ + xe^- \leftrightarrow LiCoO_2 \quad (1.1)$$

At anode: $$Li_xC_6 \leftrightarrow 6C + xLi^+ + xe^- \quad (1.2)$$

Overall reaction: $$Li_xC_6 + Li_{1-x}CoO_2 \leftrightarrow LiCoO_2 + 6C \quad (1.3)$$

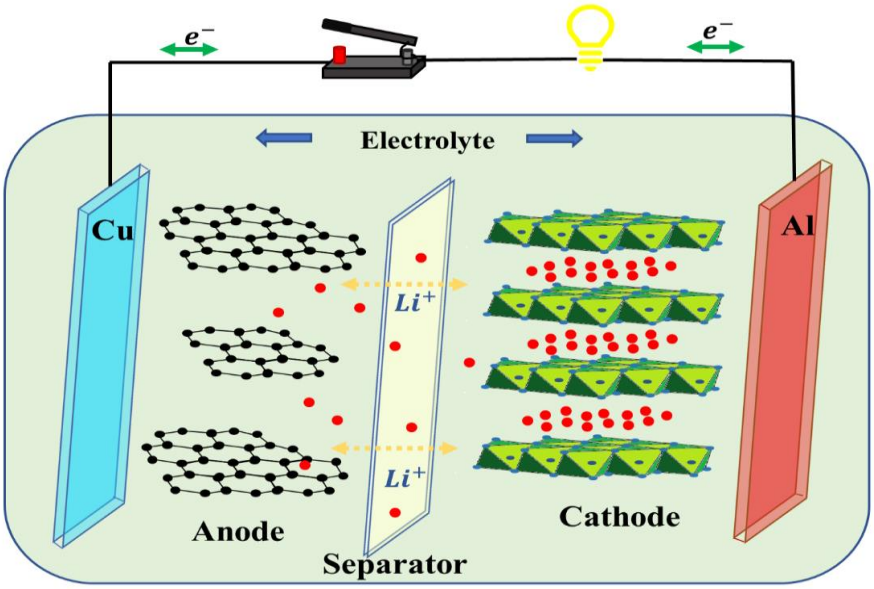

Figure 1.2 A schematic of a working lithium-ion battery (LIB) with an anode and cathode immersed in an electrolyte solution and separated by a separator.

1.4 Component of LIBs

1.4.1 Anode

The anode is the negative electrode in a battery which oxidizes during electrochemical mechanism releasing electrons to the external circuit. It is an important and essential component of a battery and has an effective contribution to a batteries overall electrochemical performance. There are various types of anode materials that are being used in LIBs such as, graphite, silicon, intermetallic or alloying materials. An ideal anode material must have a low density that can accommodate a greater number of Li-ion in its crystal structure, must yield stable and reversible gravimetric and volumetric capacity. It must be chemically stable in the presence of electrolyte; its potential must be near to that of Li metal[31,34–36]. A schematic representation of variation of average discharge potentials (Li/Li^+) and specific capacity for anode materials of LIBs are displayed in Fig.1.3.

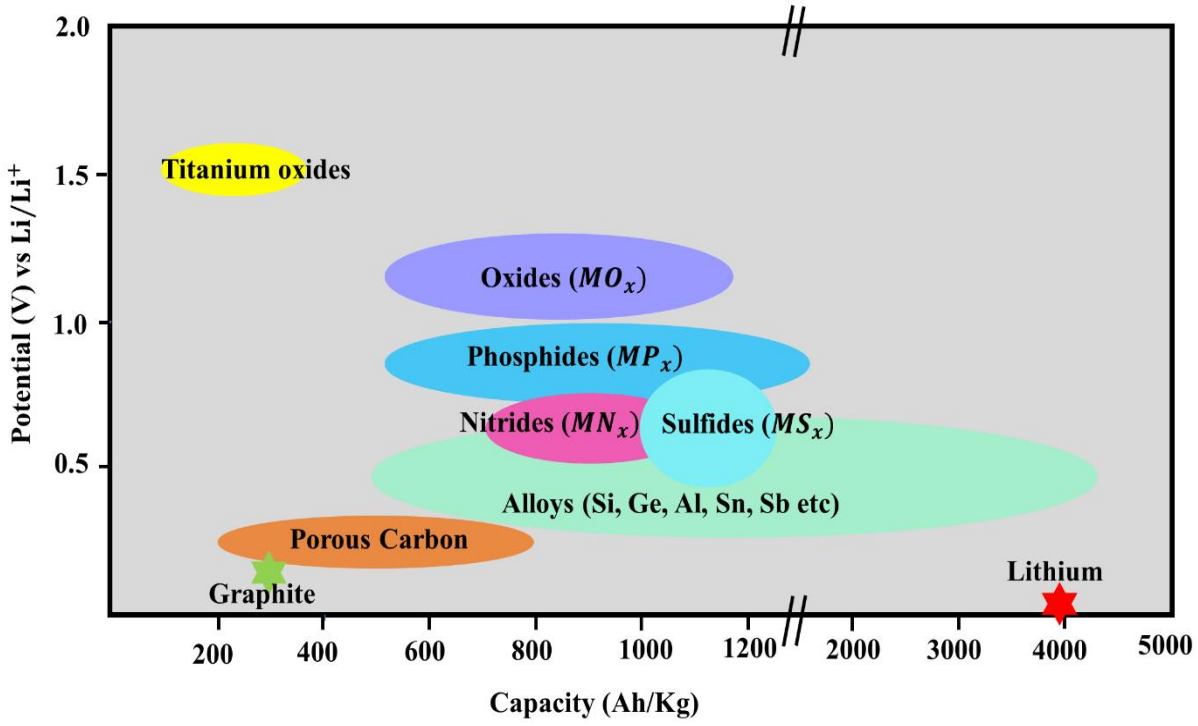

Figure 1.3 Variation of average discharge potentials (Li/Li^+) and specific capacity for anode materials of LIBs [37].

1.4.2 Cathode

The cathode is the positive electrode in a battery which reduces during discharge mechanism absorbing electrons from the external circuit. It is another vital and important component of a battery, which is also the active source of all the Li-ions. A cathode material that meets the criteria for an ideal lithium battery should possess a high discharge capacity, extended cycle longevity, minimal self-discharge, elevated voltage and pose no hazards. The initial layered transition metal oxide cathode to meet these criteria was $LiCoO_2$, initially discovered by John B. Goodenough[38–40]. It remains a staple in the majority of commercial Li-ion batteries till today. There is various cathode used in LIB such as $LiMn_2O_4$, $LiFePO_4$, vanadium oxide etc[41].

1.4.3 Electrolyte

An electrolyte comprises a lithium salt dissolved in an organic solvent, crucial for facilitating the transportation of Li-ion between the two electrodes. Ideally an electrolyte must have thermal stability, ionic conductivity, non-toxicity, electrochemical stability to high potential etc. Electrolytes can be liquid, solid or polymeric in nature. Commonly used electrolytes are liquid electrolyte and polymer electrolyte. Liquid electrolytes are mainly composed of a lithium salt dispersed in an organic solvent. Ethylene carbonate, di-methyl carbonate and di-ethyl carbonate are common organic solvent which are being used in electrolytes. $LiPF_6$ salt dispersed in Ethylene carbonate and di-methyl carbonate is the most used electrolyte in commercial LIBs[42–44].

1.4.4 Separator

Another pivotal component of a battery is separator, which allows the flow of Li-ions and restricts the flow of electrons between anode and cathode. Though separators do not engage in the electrochemical reactions in a battery, but they do play an important role in separating

the two electrodes while allowing the flow of Li-ions through electrolyte. Generally, a microporous polymer film is being used as separator in LIBs. However, the batteries with solid electrolyte or polymer electrolyte do not need any separator. The basic requirement of a separator is electrochemical stability, surface wettability, thickness less than 25 μm, pore size less than 1μm, porosity (40-60%), mechanical integrity etc. Microporous separators are made up of polyethylene (PE), Polypropylene (PP), Polyethylene terephthalate (PET) etc in LIBs[43,45,46].

All components in LIBs play crucial roles in determining the battery's overall capacity, which refers to the total charge that can be transferred, as well as its cyclability. The performance of LIBs, which encompasses aspects like energy density, charge/discharge rates, and thermal stability, is also influenced by these components.

In this research investigation, the focus is specifically on anode materials for LIBs. Anode materials are a critical component in the battery's architecture as they directly impact the battery's capacity, energy density, and rate capabilities. By studying and optimizing these materials, the research aims to enhance the overall efficiency and longevity of lithium-ion batteries, making them more reliable and effective for various applications. This focus includes exploring new materials, improving existing ones, and understanding the underlying mechanisms that contribute to the performance of the anode in LIB systems.

1.5 Types of Anode Materials

The anode in Lithium-ion batteries is divided into three distinguished groups of materials having different energy storage mechanism:

(a) Intercalation Anodes

(b) Conversion Anodes

(c) Alloy Anodes

According to the reaction mechanisms, anode materials are classified into three types as depicted in Fig 1.4.

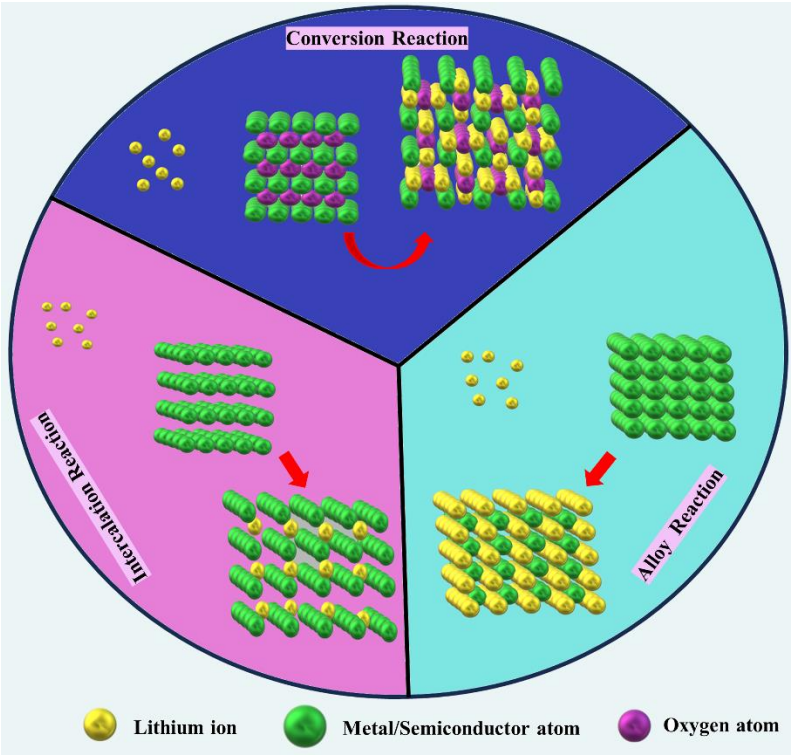

Figure 1.4 Schematic illustration of different types of anodes [47].

1.5.1 Intercalation Anodes

In this group of anode materials, the best representative material is graphite. Graphitic carbon has been thoroughly used as anode in LIBs for electronic devices. In an intercalation type anode, Li-ions are inserted or intercalated within the layers of electrode materials. The electrochemical intercalation reaction in graphitic carbon can be expressed as the follows:

$$xLi^{+} + C_6 \text{ (in graphite)} + xe^{-} \leftrightarrow Li_xC_6 \qquad (1.4)$$

Graphite has a practical reversible capacity of more than 360 $mAhg^{-1}$, the reversible process of lithiation/delithiation occurs at a potential of 0.25 V compared to Li/Li^{+}. and a discharge/charge efficiency approaching nearly 100%. Despite having these properties, there are certain drawbacks as well. One of the major drawbacks of graphitic anode is the low capacity. Therefore, many attempts were made to develop other advantageous carbon

materials to replace the graphite[37]. To attain higher capacity, one solution is to increase the surface area of the carbon-based materials in order to accommodate more lithium ion between the layers. Due to the large surface area as well as higher electronic conductivity, other forms of carbon materials such as graphene, Carbon nanofibers (CNFs), and carbon nanotubes (CNTs) are widely explored to replace graphite. Massive Artificial Graphite (MAG), Meso-carbon Micro bead (MCMB), and carbon fiber-vapor grown (VGCF) etc. are some of the commercially used graphitic material. Lately, carbon derived material such as nano-fibers, porous carbon, CNT, and graphene are widely studied to use as an anode in LIBs. Furthermore, these materials are expected to increase the electrochemical performance of the rechargeable batteries[47,48]. Yoo et al. fabricated graphene nanosheets (GNS) based anode materials and composite of GNS-C60 and GNS-CNT. The study showed that graphene could deliver a capacity of 540 $mAhg^{-1}$, which is quite higher than that of graphite. The study also revealed that the capacity could also be increased by introducing fullerene molecules or CNTs between the graphene sheets. Certain nanostructured materials or oxides when integrated with CNTs have the potential to improve the electrochemical performance and enhance the storage capacity of Li-ions in the battery[49]. Yang et al. stated that "CNTs with a coating of Fe_3O_4 displayed a capacity of 800 $mAhg^{-1}$ for 100 charge/ discharge cycles and also improved rate capability"[50].

Lithium titanium oxide (LTO) and titanium oxide (TiO_2) are another important intercalation/de-intercalation type anode materials. These two materials have proved themselves as a great anode material for LIBs owing to their cost feasibility, non-toxicity, very low volume change upon charging/discharging, but they suffer drawbacks like low theoretical capacity and electrical conductivity. Also from the safety perspective, LTO and TiO_2 could be considered as an attractive alternative to the graphitic anode, since the operating voltage for LTO and TiO_2 is above 0.8 V vs Li^+/Li. Also, the SEI layer on the LTO

and TiO_2 anode could also be prevented by elimination of the reducing electrolyte. Considering all the above-mentioned factors, it could be concluded that titanium-based anode materials displayed greater advantage over the carbon-based anode materials[51,52].

1.5.2 Alloy Anodes

The second category of anode materials after intercalation is the alloy/de-alloy materials. This group consist metal such as silicon, germanium, tin etc which can form alloy with lithium. In these type of anode materials, Li-ions insert into the anode material structure during charging, forming an alloy with the anode. The reversible alloying reaction can be expressed as follows:

$$M + x\ Li^+ + xe^- \rightarrow Li_xM \qquad \text{(where M is the anode material)} \qquad (1.5)$$

Alloying reaction-based materials gained much attention due to their high theoretical capacity, 4200 $mAhg^{-1}$ for Si; 1600 $mAhg^{-1}$ for Ge; 994 $mAhg^{-1}$ for Sn[53,54].

Germanium (Ge), silicon (Si), tin oxide (SnO), are some of the alloy anode materials which reacts with lithium via alloying/de-alloying mechanism and provides high specific capacity. Apart from these materials there are several other metals like Mg, Sb, Zn, Pt, Au, Al, etc. which participates in reaction with lithium via alloying/de-alloying mechanism. Nevertheless, tin, antimony, silicon, magnesium, and aluminium are extensively studied in research due to their non-toxic, cost-effective, and abundant nature. However, there are certain drawbacks of alloy anodes like they suffer from extreme volume change during charging and discharging which results in short cycle life. These materials also experience pulverization resulting in electrical isolation of the active material with the current collector and carbon black. The volume expansion and contraction also cause particle fracture. It has also been reported that the volume change in these materials may result in the degradation of the solid electrolyte interphase (SEI) layer and an increase in cell impedance due to

electrolyte decomposition. Recently, research have been devoted to elucidate the shortcomings of these alloy anodes. One of the solutions is to downsize the particles to nano scale and another is to make composite with lithium active/inactive materials[55].

1.5.3 Conversion Anodes

These type of anode materials comprises of transition metal compound in the form M_xX_y (where X can be oxides, phosphides, nitrides or sulphides and M is transition metal such as Mn, Fe, Zn, Co, Cu, Ni etc). The Conversion reaction-based anode materials are based on the faradaic reaction as represented by the following equation:

$$M_aX_b + (b \cdot n)Li^+ + (b \cdot n)e^- \leftrightarrow aM + bLi_nX \quad (1.6)$$

Where M could be Zn, Cu, Mn, Co, Ni, Mo etc and X may be N, S, O, F, P etc while n represents the oxidation state.

In this category of anode materials, a diverse array of anode materials can be achieved through a straightforward combination of M and X.

Transition metal oxides (TMOs) are notable as conversion reaction anode materials for their corrosion resistance, ease of use, and high specific capacity. However, practical application challenges persist. Binary metal oxides ($A_xB_yO_z$, where A and B can be elements like Ni, Fe, Zn, Co, Mn, Cu) are particularly interesting due to their electrochemical activity in LIBs, which involve a conversion reaction mechanism with two active metal ions. During the initial discharge, these metals reduce to nanoparticles and disperse within a Li_2O matrix. After complete delithiation, a mixture of two metal oxides (AO_x and BO_y) is formed by replacing the original binary metal oxides ($A_xB_yO_z$)[56,57].

The electrochemical reaction can be succinctly summarized as follows:

$$A_xB_yO_z + 2zLi^+ + 2ze^- \rightarrow xA + yB + zLi_2O \quad \text{(first lithiation)} \quad (1.7)$$

$$A + B + (x + y)Li_2O \rightarrow AO_x + BO_y + 2(x + y)Li^+ + 2(x + y)e^- \quad \text{(first delithiation)} \quad (1.8)$$

$$AO_x + BO_y + 2(x + y)Li^+ + 2(x + y)e^- \leftrightarrow A + B + (x + y)Li_2O \quad (1.9)$$

Binary metal oxides of the AB_2O_4 type generally have a spinel structure and are notable for their high electrochemical activity and electrical conductivity, making them appealing for use in LIBs. As anodes in LIBs, AB_2O_4 type metal oxides can achieve a high theoretical specific capacity of nearly 1000 $mAhg^{-1}$ by transferring 8 electrons. However, a significant volume expansion during lithiation can lead to poor cycling performance[58,59].

1.6 Material to be Investigated

1.6.1 Alloying/de-alloying anode

Group IV elements like silicon, germanium, and tin are perceived as potential anode materials for LIBs owing to their significantly higher specific capacities compared to carbon-based anodes. Recent reviews show that alloy anodes offer theoretical capacities 2-10 times greater than carbon anodes (372 $mAhg^{-1}$) and 4-20 times higher than lithium titanate (LTO) anodes (175 $mAhg^{-1}$). These materials also operate at moderate potentials versus lithium, reducing the risk of lithium deposition and associated safety concerns.

1.6.1.1 Sn-Se

Metallic tin alloys with lithium to form $Li_{4.4}Sn$, achieving a high theoretical capacity of 994 $mAhg^{-1}$ and a higher potential vs Li/Li^+, thereby improving stability and safety[60,61]. Despite extensive research on tin-based anodes, commercialization is hindered by significant volume expansion during cycling, leading to particle cracking and capacity loss. Strategies to address these issues include nano-structuring and using intermetallics or composites instead of pure tin. Nanosized anode materials offer improved strain accommodation, specific capacity, and rate capability due to enhanced interfacial area and Li-ion diffusion kinetics[62]. Tin readily reacts with elements from groups VA and VIA to form binary or

ternary compounds (Sn-M, Sn-M-M'), such as Sn-Se, Sn-Sb, Sn-Co, Sn-Ni, and Sn-Cu[63–67]. This approach involves alloying tin with inactive materials to reduce volume changes during charging and discharging. Some intermetallic compounds include electrochemically inactive elements like Ni and Cu, which do not react with lithium. These elements help mitigate the volume expansion and contraction during lithiation and delithiation, thereby improving the cycling performance of tin-based anodes. Intermetallic compounds like Sn-Sb and Sn-Bi contain electrochemically active elements, offering higher initial capacities than those with inactive components. This is due to the formation of multiple lithiated phases from the active components at different potentials relative to Li/Li^+ within the electrode[68–73]. However, in some compounds, such as Sn-Se, while initial lithiation occurs, the resulting lithiated phases, except Li_xSn, remain electrochemically inert in subsequent cycles[74]. Micro-sized $Sn_{0.9}Se_{0.1}$ particles demonstrated a higher capacity of 500 $mAhg^{-1}$ compared to pure Sn particles (200 $mAhg^{-1}$) after 100 cycles at 0.50 Ag^{-1} within a voltage range of 0.01-1.2 V vs. Li/Li^+. This improvement is due to the buffering against volumetric change in tin and enhanced Li-ion diffusivity, facilitated by the inert lithiated Se phase (Li_2Se)[75]. In the SnSe system, Se is crucial for mitigating volume changes, as the Li-Se phase, forming at a higher lithiation potential than Li-Sn, acts as a buffer matrix. This matrix absorbs volume expansion, reducing internal strain and enhancing electrode stability. Unlike tin oxides, which are insulators, tin selenide exhibit properties of a narrow band gap semiconductor, rendering it as a promising material for various applications like solar cells, optoelectronics, and memory switching devices. Tin selenide exists in two phases: hexagonal-phase $SnSe_2$ and orthorhombic-phase SnSe [76].

Initial studies on SnSe thin films as anodes, prepared via reactive pulsed laser deposition, showed reversible discharge capacities between 400 and 681 $mAhg^{-1}$ during first 40 cycles. However, SnSe faces issues like significant volume change, particle aggregation, and low

conductivity, which impair its electrochemical performance[77]. A colloidal composite of $SnSe_2$ nanoplates and graphene demonstrated excellent storage capabilities, with a reversible discharge capacity of 470 to 640 $mAhg^{-1}$ over 30 cycles. However, solution-based synthesis methods for tin selenide are limited. SnSe nanocrystals, produced via gas-phase photolysis, exhibited capacities of 510 to 412 $mAhg^{-1}$ over 70 cycles[78]. A SnSe/carbon black nanocomposite, also synthesized by ball milling, showed an initial capacity of 1097.6 $mAhg^{-1}$, which decreased to 633.1 $mAhg^{-1}$ after 100 cycles[79].

1.6.2 Conversion based anodes

Following the influential research by Poizot et al., nanoparticles of TMOs have been investigated as potential anode materials for LIBs. These investigations demonstrated remarkable electrochemical characteristics, attaining a capacity of 700 $mAhg^{-1}$ while maintaining full capacity retention even after 100 cycles. It was proposed that the remarkable electrochemical reactivity of TMOs could enhance the overall performance of these batteries[80]. The electrochemical reactions of TMOs are given as:

$$M_xO_y + 2yLi^+ + 2ye^- \rightarrow yLi_2O + xM \text{ (M = Zn, Mn, Fe, Ni and Co)} \quad (1.10)$$

Herein, the redox interactions between metal oxides and lithium ions exhibit thermodynamic favourability, involving multiple electron transfers per metal atom. This results in notable specific capacities ranging from 500 to 1000 $mAhg^{-1}$[81,82]. Despite their high reversible capacities and energy densities, simple metal oxides encounter challenges such as low coulombic efficiencies during the initial cycle, instability in forming the solid electrolyte interface (SEI) layer, limited capacity retention, and significant voltage hysteresis[83]. Therefore, these challenges could be addressed by considering mixed-metal oxides like $ZnCo_2O_4$, $ZnFe_2O_4$, $CoFe_2O_4$ and $MnCo_2O_4$ as potential anode materials for lithium-ion batteries. Their rapid ionic-transport properties, excellent electronic conductivities and

straightforward synthesis routes make them promising candidates. Furthermore, their diverse architectures and controllable crystallinity suggest that these mixed-metal oxides could serve as effective materials for storing electrochemical energy in lithium-ion batteries. Mixed-metal oxides possess unique characteristics such as complex chemical compositions and synergistic effects at interfaces, which contribute to improved electrochemical performance and electronic conductivity[84,85]. The spinel structure, represented by the formula AB_2O_4, comprises divalent cations (A) and trivalent cations (B) along with oxygen ions. It comprises 32 oxygen ions arranging tetrahedrally and 32 octahedral cations within a unit cell, totalling 64 tetrahedral and 32 octahedral cations. The spinel structure can be categorized as normal, inverse, and mixed spinel, depending upon the arrangement of cations within the structure[85–87].

1.6.2.1 AFe_2O_4 (Metal Ferrites)

AFe_2O_4-based spinel ferrites are renowned for their favourable electrical and magneto-optical properties, determined by the distribution of cations on the A- and B-sites. They have been extensively explored across various fields, including ferrofluids, magnetic resonance imaging and electronics[88–90]. Ferrite-based materials, such as spinel-ferrite MFe_2O_4 (where M represents Zn, Mg Co, Ni, Mn, and Cu), offer several advantages as they are abundant, cost-effective, and eco-friendly. These materials demonstrate significant discharge capacities, reaching up to 1000 $mAhg^{-1}$, which is notably higher than those of commercially employed graphite anodes, typically two to three times greater[91].

1.6.2.1.1 $ZnFe_2O_4$

$ZnFe_2O_4$ displays a characteristic normal-spinel structure, in which Zn^{2+} occupies tetrahedral site and the octahedral site are occupied by Fe^{3+} [92,93]. This configuration makes $ZnFe_2O_4$ a promising option as anode materials, attributed to its notable theoretical capacity of approximately 1000 $mAhg^{-1}$. The primary charge-storage mechanism in $ZnFe_2O_4$ mainly

entails alloying-dealloying and conversion-reaction mechanisms[94]. Teh et al. developed 1D $ZnFe_2O_4$ nanofibers that demonstrated an impressive initial specific capacity of 925 $mAhg^{-1}$ at a 0.6 C-rate which stabilized to 733 $mAhg^{-1}$ after 30 cycles. These nanofibers also maintained a high capacity of 400 $mAhg^{-1}$ at 800 mAg^{-1}, surpassing the performance of commercially used graphite anodes. The enhanced capacity is attributed primarily to the unique morphology of the $ZnFe_2O_4$ nanofibers[95]. Yao and colleagues developed a mesoporous composite of $ZnFe_2O_4$ and graphene that demonstrated outstanding electrochemical properties. This superior performance is due to the collaborative effect of the large surface area of $ZnFe_2O_4$ combined with the flexibility and high electronic conductivity of graphene. After 100 cycles, the mesoporous composite exhibited specific capacity of 870 $mAhg^{-1}$ at 1 Ag^{-1} and showed excellent rate performance. It maintained a specific capacity of 713 $mAhg^{-1}$ at 2 Ag^{-1}, highlighting its ultrafast charging capability and good cycling stability[96]. Table 1.1 provides a summary of the electrochemical performance of $ZnFe_2O_4$ and its hybrid, synthesized using different techniques.

Table 1.1 A summary of electrochemical investigations of $ZnFe_2O_4$ and its hybrid, synthesized using different techniques for LIBs.

Sample	**Synthesis Route**	**Specific Capacity**	**Rate Capability**	**Reference**
$ZnFe_2O_4$	Combustion route	615 $mAhg^{-1}$ at 60 mAg^{-1}, 50 cycles	-	[94]
$ZnFe_2O_4$ nanofibers	Electrospinning	733 $mAhg^{-1}$ at 60 mAg^{-1}, 30 cycles	400 $mAhg^{-1}$at 0.8 C	[95]

$ZnFe_2O_4$ nano-octahedrons	Hydrothermal method	910 $mAhg^{-1}$ at 60 mAg^{-1}, 80 cycles	730 $mAhg^{-1}$ at 1 C	[97]
$ZnFe_2O_4$/C hollow sphere	Solvothermal synthesis	625 $mAhg^{-1}$ at 500 mAg^{-1}, 30 cycles	450 $mAhg^{-1}$ at 0.7 C	[98]
$ZnFe_2O_4$/graphene hybrid	Solvothermal synthesis	600 $mAhg^{-1}$ at 200 mAg^{-1}, 90 cycles	400 $mAhg^{-1}$at 0.8 C	[99]
$ZnFe_2O_4$–C nanocomposite	Sol–gel technique	681 $mAhg^{-1}$at 0.1C, 100 cycles	469 $mAhg^{-1}$ at 4C	[100]
Carbon coated $ZnFe_2O_4$ nanoparticles	Carbonothermal method using sucrose	1300 $mAhg^{-1}$at 40 mAg^{-1}, 100 cycles	525 $mAhg^{-1}$ at 4C	[101]

1.6.2.1.2 $CoFe_2O_4$

Considerable research has been conducted on cobalt ferrite as an anode for LIBs owing to its non-toxicity, strong chemical stability, and affordability. $CoFe_2O_4$ stores Li-ions via a conversion reaction and boasts a high theoretical specific capacity of 914 $mAhg^{-1}$[102,103]. Despite its potential, $CoFe_2O_4$ suffers from significant drawbacks such as substantial volume fluctuations, which cause the active material to crumble and clump together, and poor conductivity. These issues result in unsatisfactory cycling durability and low-rate capabilities of the $CoFe_2O_4$ particles[104,105]. To enhance its performance, researchers have synthesized $CoFe_2O_4$ nanoparticles with various morphologies as well as composites with different conductive matrices. Xiong and coworkers synthesized $CoFe_2O_4$ via a hydrothermal method obtaining various morphologies such non-uniform particles, microspheres, and flower-like microspheres. Among all the microstructures, the

microspheres resembling flowers exhibited a larger surface area, measuring 51.0 m^2g^{-1}, surpassing that of regular microspheres. Moreover, the microspheres resembling flowers exhibited an impressive reversible capacity of 790 $mAhg^{-1}$ at 0.2 C-Rate. Even when subjected to higher C-rate (1C), they retained a considerable discharge capacity of 744 $mAhg^{-1}$. The achievement of excellent capacity and rate capability is attributed to the effective electronic conductivity of the electrode. This facilitates a swift charge-transfer process while charging and discharging[106]. Zhang and coworkers reported on the remarkable electrochemical performance of mesoporous $CoFe_2O_4$ nanospheres integrated with carbon nanotubes (CNTs). The nanospheres were incorporated with varying weight ratios of CNTs, including 10%, 20%, and 30%. Among these compositions, the $CoFe_2O_4$ with 20% CNTs exhibited the capacity of 1137 $mAhg^{-1}$ after 10 cycles at 0.2 C rate. Furthermore, when C rate was increased to 1.2 C , it maintained a specific capacity of 648 $mAhg^{-1}$ with stable cycling and outstanding rate performance, surpassing the performance of the $CoFe_2O_4$ -graphene composite[105]. Conversely, Kumar et al. demonstrated that the porous $CoFe_2O_4$-rGO, when combined with an alginate binder, exhibited exceptional electrochemical performance, surpassing that of both CNTs and graphene composites[102]. This underscores the critical roles played by innovative binders and conductive matrices in enhancing both the cycling stability and rate capability of an electrode material.

1.6.2.2 ACo_2O_4 (Metal Cobaltite)

Spinel cobaltite represent a significant category of spinel-type materials that have garnered considerable attention for their potential applications across various fields, including supercapacitors, sensors, and LIBs[107–111]. ACo_2O_4 has shown remarkable performance in LIBs, exhibiting high specific capacities, extended cycle life, and favourable rate performance. Moreover, it is considered to be marginally less toxic compared to Co_3O_4. In general, spinel cobaltite primarily stores lithium ions via a conversion-reaction mechanism,

with the exception of $ZnCo_2O_4$, which employs both the conversion and alloying-dealloying mechanisms.

1.6.2.2.1 $ZnCo_2O_4$

$ZnCo_2O_4$ and its composites have garnered significant interest as promising materials for anodes in lithium-ion batteries. In $ZnCo_2O_4$ spinel structure, tetrahedral coordinated sites are occupied by Zn^{2+} ions, while Co^{3+} ions occupy octahedral coordinated sites. This structural arrangement entails an overarching electrochemical process, which includes an alloying reaction between the Zn and Li and a conversion event involving the Co and Zn ions, which collectively contribute to the overall charge-storage capacity[112–114]. The reaction mechanism is expressed as follows:

$$ZnCo_2O_4 + 8Li^+ + 8e^- \rightarrow Zn + 2Co + 4Li_2O \quad (1.11)$$

$$Zn + Li^+ + e^- \leftrightarrow LiZn \quad (1.12)$$

$$Zn + Li_2O \leftrightarrow ZnO + 2Li^+ + 2e^- \quad (1.13)$$

$$2Co + 2Li_2O \leftrightarrow 2CoO + 4Li^+ + 4e^- \quad (1.14)$$

$$2CoO + \frac{2}{3}Li_2O \leftrightarrow \frac{2}{3}Co_3O_4 + \frac{4}{3}Li^+ + \frac{4}{3}e^- \quad (1.15)$$

$ZnCo_2O_4$ has been extensively explored, with researchers investigating its electrochemical performance using various morphologies. These include nanotubes, uniform mesoporous microspheres, yolk–shelled microspheres and 3D hierarchical nanowires[113–116]. Additionally, it has been grown on different current collectors, such as Ni foam and carbon cloth. Table 1.2 lists the electrochemical performances of $ZnCo_2O_4$.

Table 1.2 A summary of electrochemical investigations of $ZnCo_2O_4$ and its hybrid, synthesized using different techniques for LIBs.

Sample	**Synthesis Route**	**Specific Capacity**	**Rate Capability**	**Reference**
Nanophase $ZnCo_2O_4$	Combustion route	894 $mAhg^{-1}$ at 60 mAg^{-1}, 60 cycles	400 $mAhg^{-1}$ at 0.7C	[112]
$ZnCo_2O_4$ nanowires/carbon cloth	Hydrothermal synthesis	1278 $mAhg^{-1}$ at 200 mAg^{-1}, 100 cycles	605 $mAhg^{-1}$ at 5C	[114]
Yolk–shelled $ZnCo_2O_4$ microsphere	Refluxing method	949 $mAhg^{-1}$ at 200 mAg^{-1}, 100 cycles	331 $mAhg^{-1}$ at 1000 mAg^{-1}	[116]
$ZnCo_2O_4$/graphene nanosheets	Auto-combustion route	755 $mAhg^{-1}$ at 0.1C, 70 cycles	302 $mAhg^{-1}$ at 4.5C	[117]
Flake-by-flake $ZnCo_2O_4$	Co-precipitation	1275 $mAhg^{-1}$ at 100 mAg^{-1}, 50 cycles	730 $mAhg^{-1}$ at 3000 mAg^{-1}	[118]
Flower-like $ZnCo_2O_4$ nanowires	Hydrothermal method	900 $mAhg^{-1}$ at 200 mAg^{-1}, 50 cycles	347 $mAhg^{-1}$ at 800 mAg^{-1}	[119]
Porous $ZnCo_2O_4$ Nanowires	Sacrificial Template route	1197 $mAhg^{-1}$ at 100 mAg^{-1}, 20 cycles	-	[120]

1.7 Objective of the Thesis

The aim of the proposed research work is to develop novel anode materials for lithium-ion batteries (LIBs). In spite of the rigorous research work on AB_2O_4 spinel transition metal oxides (TMO's) and tin-based alloy anode materials, still there are certain drawbacks reported in these anode materials like low electronic conductivity, volume expansion which prompted us to carry out the present research work on tin-based alloy anode and AB_2O_4 type TMO's anode.

- Synthesis of conversion reaction based AB_2O_4 type transition metal oxides like AFe_2O_4 (A=Zn, Co) and ACo_2O_4 (A=Zn) and tin-based alloy anode Sn-M (M=Se) using different synthesis routes such as solid-state method, combustion route, etc.
- Physico-chemical characterizations of synthesized anodes for structural and morphological analysis using XRD, SEM, EDX, TEM, FTIR, etc.,
- Improvement in the electronic/ionic conductivity of synthesized anode materials on doping at anionic or cationic sites with Mn, Mg etc elements.
- Enhancement in the electronic/ionic conductivity of synthesized anode materials by the hybrid structures of synthesized materials with carbon-based material (Super P, CNTs or graphene)
- Electrochemical analysis such as cyclic voltammetry (CV), galvanostatic charge-discharge (GCD), cyclability, rate performance, and electrochemical impedance spectra (EIS) of synthesized anode materials.

Chapter 2 : Experimental and Characterization Techniques

This chapter provides a comprehensive detail of the synthesis and characterization methodologies employed in this study. It also outlines the preparation of anode electrode materials, and the assembly of coin cells for electrochemical evaluation. Additionally, it delves into the principles and methodologies of the characterization techniques used to assess both the physicochemical and electrochemical properties of the anode materials.

2.1 Synthesis Technique

This section deals with details of the diverse synthesis methodologies employed to fabricate anode materials in this study. Synthesis technique such as solid-state reaction route, sol-gel route, and combustion method were utilized to prepare the electrode materials. The specific techniques and precursor materials utilized for synthesis are outlined below.

2.1.1 Solid State Route

Solid state method using high-energy ball mill (HEBM) stands out as a prevalent choice in both industrial, academic research and development laboratories(R&D). Its widespread adoption owes to its simplicity and cost efficiency, making it suitable for synthesizing metal and alloy powders across various applications. This method involves high-speed mixing and grinding of precursors over an extended period, ensuring thorough blending and synthesis. Subsequently, the prepared samples undergo high-temperature calcination to yield the desired electrode materials. The final product is highly crystalline as observed by HEBM method and it attains a smaller particle size in comparison to other synthesis methods. Figure 2.1 illustrates the schematic depicting the sample preparation process and the corresponding equipment employed. SnSe, $ZnFe_2O_4$, $ZnCo_2O_4$ were synthesized using solid state HEBM route. However, a drawback of this approach is the high-temperature calcination, which can lead to increased crystallite size and irregular particle shapes. All chemicals utilized in this research were of high purity (98% to 99.9%) and analytical grade.

2.1.1.1 Preparation of SnSe

SnSe material was prepared using high energy ball mill (HEBM). Initially, Sn powder (99.9% purity) and Se powder (99.5% purity) were first grounded and then added to a stainless-steel vial containing steel balls. The vial was sealed in glove box in order to create an inert atmosphere. Milling was done effectively for 15 hours at a rotary speed of 350 rpm. After the milling, SnSe particles were obtained. Similarly, SnSe/C and SnSe/MWCNT

composite were synthesized using Sn metal powder, Se metal powder, Super P and MWCNTs under the same conditions as mentioned above. Figure 2.1 illustrates the schematic diagram of the synthesis route.

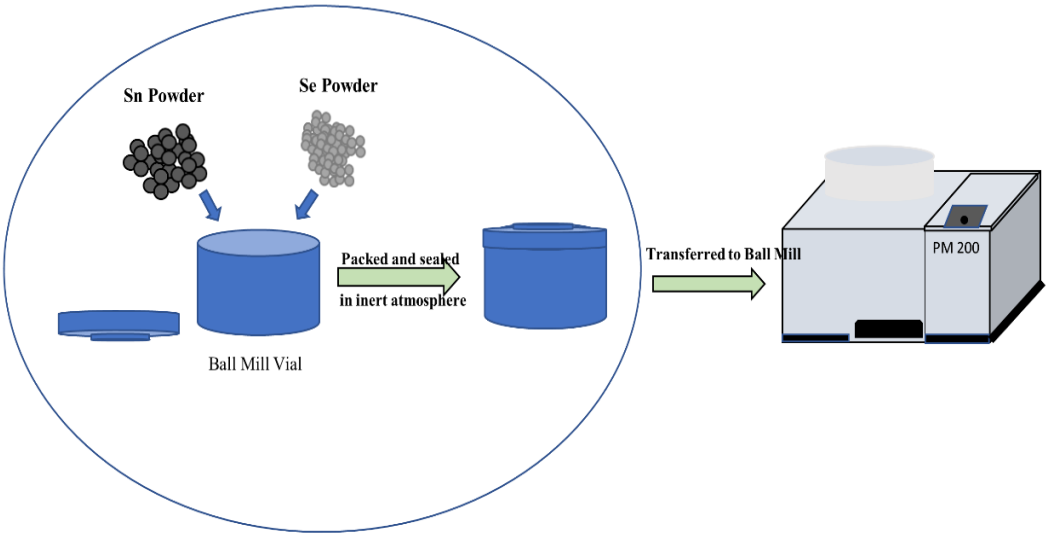

Figure 2.1 Schematic diagram for synthesis of SnSe, SnSe/C and SnSe/MWCNT composite

2.1.1.2 Preparation of $ZnFe_2O_4$

Synthesis of $Zn_{1-x}Mn_xFe_2O_4$ (x= 0.0,0.01,0.03,0.05) has been carried out using HEBM technique. The schematic diagram for the synthesis of $Zn_{1-x}Mn_xFe_2O_4$ (x= 0.0,0.01,0.03,0.05) is shown in Fig 2.2. The stoichiometric amount of the precursors Fe_2O_3 (Sigma-Aldrich, grade ≥ 99%), ZnO (Sigma-Aldrich, grade ≥ 99%), and MnO (Sigma-Aldrich, grade ≥ 99%) were ball milled together using a Retsch make model PM 100 Ball Mill machine. A stainless-steel vial of volume, 50 cm^3 and balls of 10 mm diameter were used to ball mill the precursor. In order to obtain proper mixing, the weight of the ball to the weight of the powder ratio was maintained as 10:1, and the mixing of precursors was done for 12 hours effectively at 350 rpm. The homogenously mixed precursors were then sintered at a temperature of 800 ^oC for 4 hours.

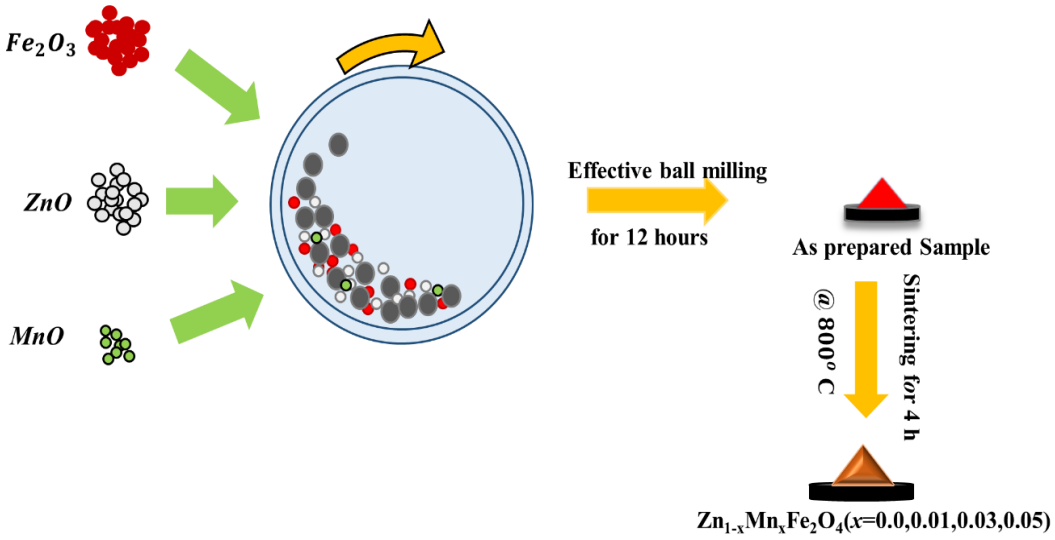

Figure 2.2 Schematic diagram for the synthesis of $Zn_{1-x}Mn_xFe_2O_4$ (x= 0.0,0.01,0.03,0.05) sintered at 800 °C for 4 hours.

2.1.1.3 Preparation of $ZnCo_2O_4$

All the precursors used in the synthesis of $ZnCo_2O_4$ are of laboratory grade made by Sigma Aldrich. In high energy ball milling method, Co $(CH_3COO)_2$ and Zn $(CH_3COO)_2$ were weighed in the molar ratio 1:2 and $C_6H_8O_7$ (120% mole fraction) were added to the ball mill, along with a little amount of de-ionized water. The effective ball milling time was kept 12 hours at 300 rpm to obtain the as-prepared sample. The sample was kept in a vacuum oven to dry out the moisture, and a pink coloured sample was collected. The sample was further treated at 800 °C in a muffle furnace to finally obtain $ZnCo_2O_4$. Figure 2.3 illustrates the schematic diagram of the synthesis route of $ZnCo_2O_4$.

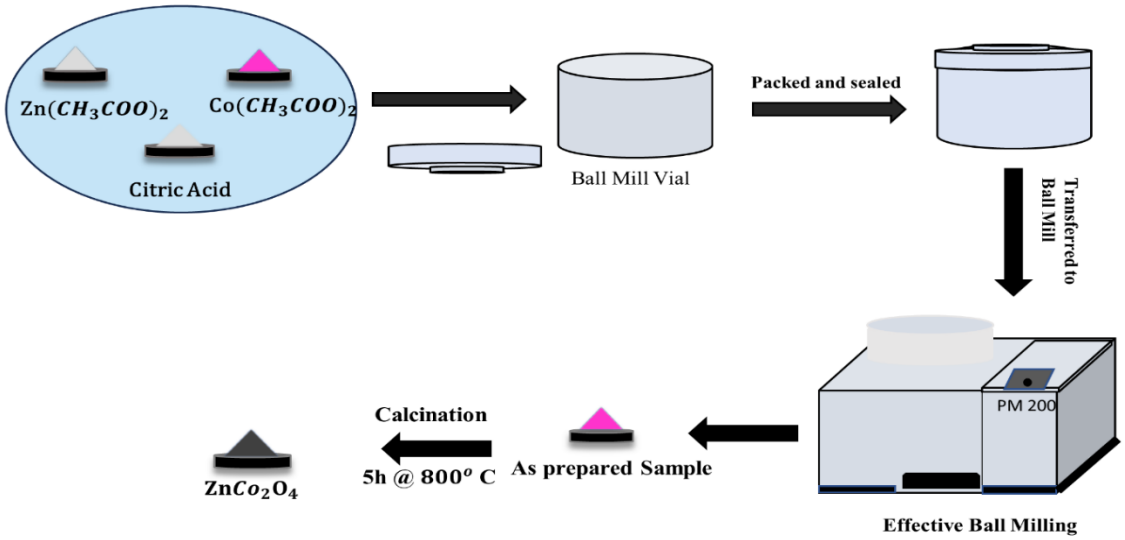

Figure 2.3 Schematic diagram for the synthesis of $ZnCo_2O_4$ via solid state route at 800 °C for 5 hours.

2.1.2 Synthesis by Combustion method

Combustion synthesis (CS) is an energy-efficient method enabling straightforward scalability and continuous technology for producing a diverse range of materials. The combustion synthesis (CS) method relies on self-sustaining exothermic reactions that occur without the need for external heat sources. Solution combustion synthesis (SCS) is a adapted form of combustion synthesis in which precursors are mixed in molar ratio within an aqueous solution. SCS is known for its adaptability and cost-effectiveness in generating a wide array of materials. This method can be used to tailor the characteristics, such as particle size, surface area, and chemical composition. The properties of the resulting materials can be precisely control by adjusting the type of fuel and the combustion conditions. Additionally, SCS produces a significant release of gases during synthesis, resulting in the formation of nanomaterials with a large surface area, thereby improving their overall performance. Considering its cost-effectiveness, versatility, and ability to control material properties, SCS emerges as an attractive method for producing materials for various applications. Initial

precursors typically include different oxidizers (mainly metal nitrites) and fuels such as urea, citric acid and glycine, which exhibit high solubility in solvents like water.

2.1.2.1 Synthesis of $ZnCo_2O_4$

Sigma Aldrich make precursors of $Zn(NO_3)_2.6H_2O$ and $Co(NO_3)_2.6H_2O$ were used in a stoichiometric ratio of 1:2 and were added in the de-ionized water and mixed under continuous stirring at room temperature. Then, both the solutions were combined in an aqueous solution of Urea, NH_2CONH_2 (Sigma-Aldrich, >99%). For regulated combustion, urea and metal nitrates were kept at a ratio of 10:6. The obtained final solution was kept under vigorous stirring at 80 ^oC for 30 minutes. Then, the excess D.I. water was removed by gradually raising the temperature to 300 ^oC. While stirring, the homogenously mixed solution turned thick and formed a gel. The viscous gel turns into the form of foam and eventually burned on its own at 300 ^oC. The as-prepared sample was collected and calcinated in a furnace at 700 ^oC for 5 hours. The schematic diagram for the synthesis of $ZnCo_2O_4$ via urea assisted combustion has been shown in Fig. 2.4.

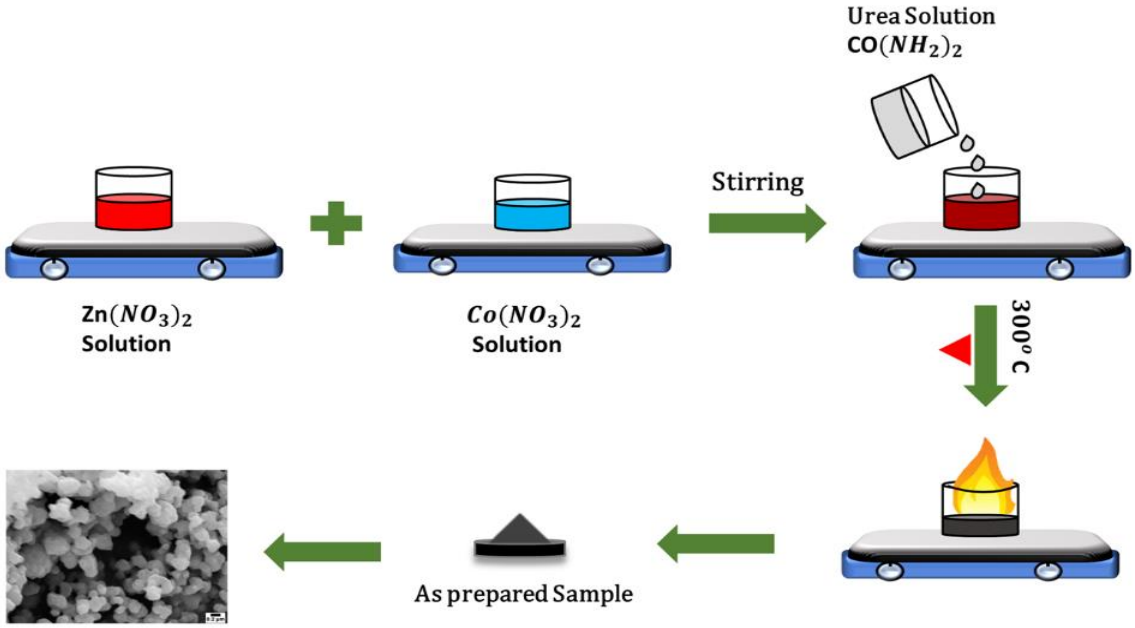

Figure 2.4 Schematic diagram for the synthesis of $ZnCo_2O_4$ via urea assisted combustion route

2.1.2.2 Preparation of $CoFe_2O_4$

Nanoparticles of cobalt ferrite were synthesized via an auto-combustion reaction, employing high-purity chemicals including iron nitrate ($Fe(NO_3)_3 \cdot 9H_2O$, 99.99%, Aldrich), cobalt nitrate ($Co(NO_3)_2 \cdot 6H_2O$, 98%, Aldrich), citric acid ($C_6H_8O_7$, 99.5%, Aldrich), and ammonium hydroxide (NH_4OH, 28-30%, Aldrich). The metal nitrates were dissolved simultaneously in a small quantity of D.I water until a transparent solution was achieved, while maintaining a molar ratio of 1:2 for Co:Fe. The metal nitrates solution was then mixed with an aqueous citric acid solution, resulting in a 1:1 molar ratio between total metal ions and citric acid. The resultant mixture, comprising salts, deionized water, and citric acid, underwent stirring to achieve homogeneity before heating at 80°C using a hot plate magnetic stirrer. The pH of the solution was maintained around 7 by adding ammonia.

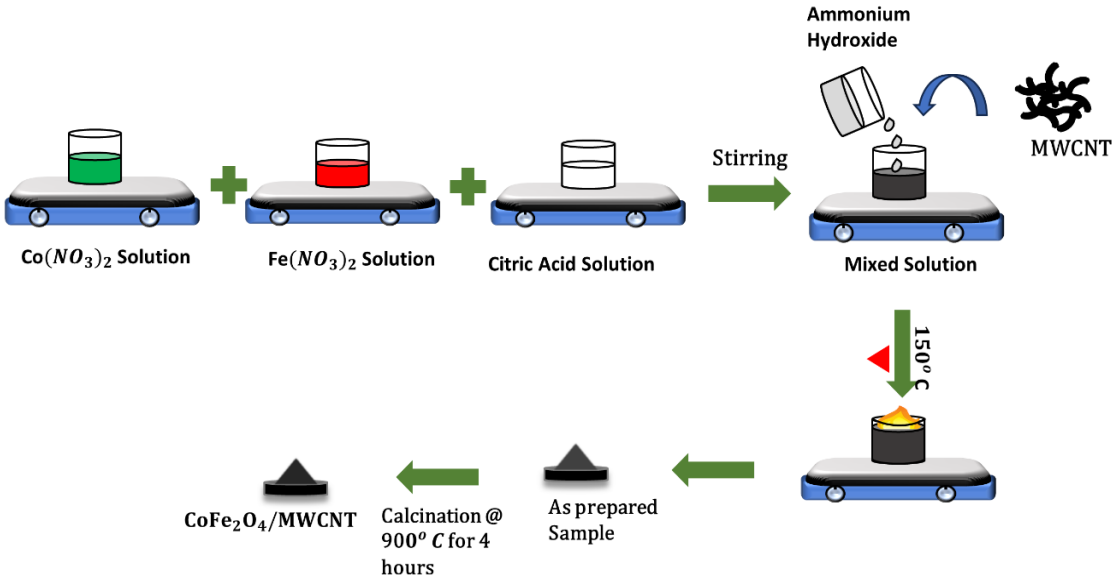

Figure 2.5 Schematic diagram for the synthesis of $CoFe_2O_4$ via sol-gel auto combustion route.

Stirring at a constant rate, the temperature was increased to 150°C, causing water evaporation and resulting in the formation of a viscous gel. As the water was entirely evaporated, the gel started foaming and ignited, burning vigorously with glowing flints. This

auto-ignition process continued until the entire citrate complex was consumed, completing within a minute and leaving behind brown-colored ashes termed as a precursor. The schematic illustration for the synthesis of $CoFe_2O_4$ is shown in Fig. 2.5.

2.2 Characterization Techniques

In order to explore the properties of the synthesized materials, a range of characterization techniques have been employed to encompassing structural, morphological, surface, electrical, and electrochemical analysis. This section provides an introduction, operational principles, and an overview of these characterization methods. The specific techniques utilized in this research are detailed in Fig. 2.6.

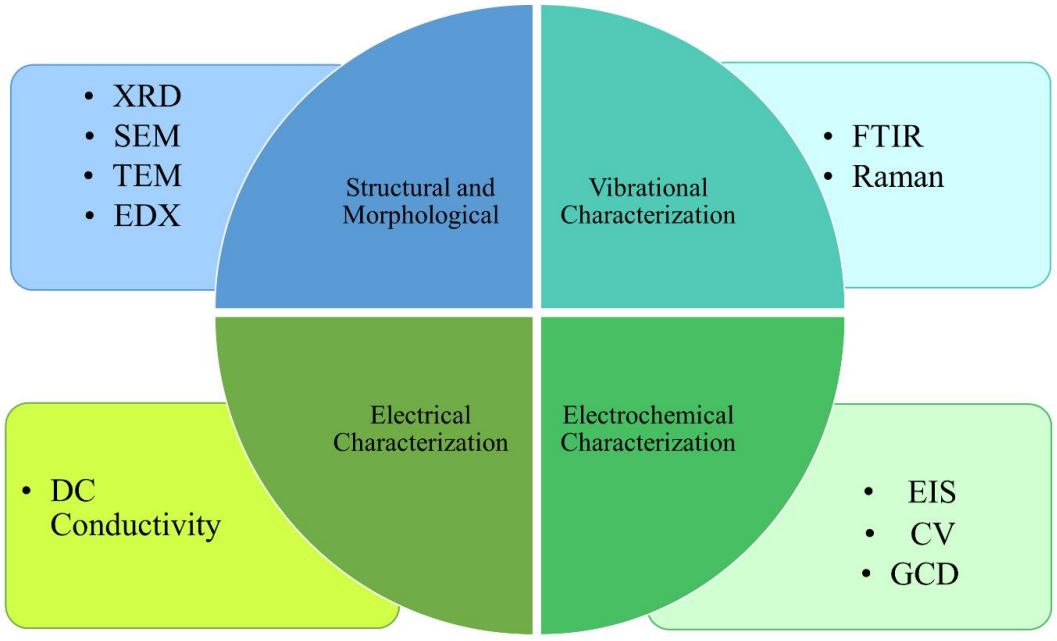

Figure 2.6 Schematic of various types of characterization techniques used in this research work.

2.2.1 Thermal Characterization

2.2.1.1 Thermogravimetric and Differential Thermal Analysis (TGA and DTA)

Thermogravimetric analysis (TGA) and differential thermal analysis (DTA) constitute crucial thermal characterization techniques wherein the variation in sample mass is monitored relative to temperature over time. TGA offers insights into the physical properties

of the sample, including phase transitions, absorption, purity, decomposition temperature, and adsorption. Furthermore, it enables the investigation of chemical processes such as oxidation, reduction, or decomposition. In TGA, the sample is positioned on a thermobalance, and its mass is continuously measured as temperature increases in the presence of air/inert or another specified gaseous environment. Throughout the experiment, the mass of the sample is meticulously recorded. In contrast, differential thermal analysis (DTA) entails monitoring temperature difference between the sample and a reference sample either with respect to temperature or time. This technique offers insights into exothermic or endothermic reactions, crystallization, melting, and sublimation points of materials.

In this study, a PerkinElmer make TGA analyzer Model: TGA 4000 was utilized for TGA and DTA study. The heating rate for all prepared samples was set at 10^{o} C/min, reaching a maximum temperature of 900^{o} C in an air environment.

2.2.2 Structural and Morphological Characterizations

2.2.2.1 X-ray Diffraction (XRD)

X-Ray Diffraction (XRD) serves as a reliable characterization method employed for the examination of crystalline solids, characterized by an orderly arrangement of atoms or molecules. When X-rays of Cu $K_{\alpha 1}$ of wavelength, 1.540 Å are directed onto the crystal lattice, they induce wave scattering. This scattering results in the constructive or destructive interference of waves in specific directions. Through the analysis of these interference patterns, lattice structures, d-spacing, and the arrangement of atoms or molecules can be elucidated. These directional reflections are determined using Bragg's law:

$$n\lambda = 2d \sin\theta \qquad (2.1)$$

where, "n" represents the order of the reflecting plane, "λ" stands for the wavelength of the X-rays, "d" signifies the lattice spacing, and "θ" denotes the angle of incidence.

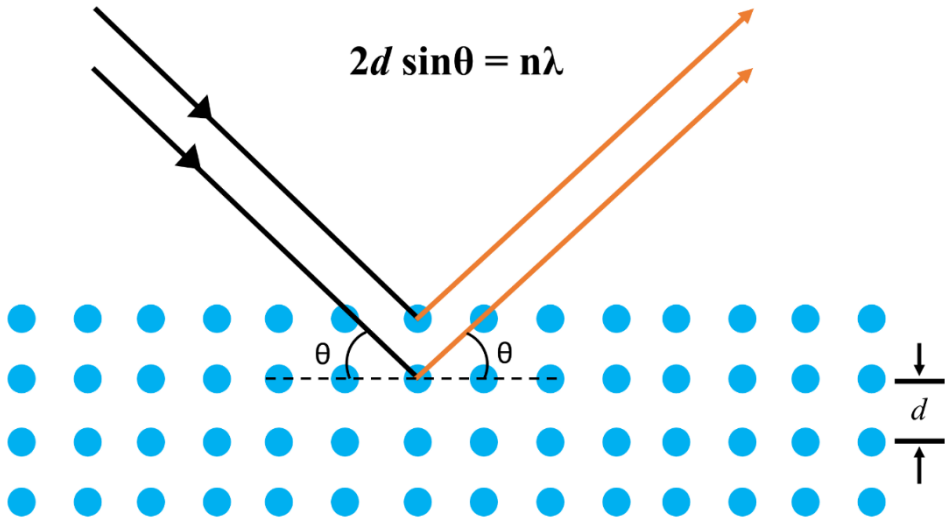

Figure 2.7 Schematic of X-ray diffraction using Bragg's law.

2.2.2.2 Scanning Electron Microscopy (SEM)

A scanning electron microscope (SEM) uses an electron beam to scan across the surface of a specimen, creating an image. Interactions between the sample's atoms and the electrons produce various detectable signals, unveiling details about the sample's surface texture and composition. These electron-induced signals offer insights into the sample's crystalline structure, exterior morphology, and chemical composition. Typically, a selected portion of the sample's surface is examined, and a 2-D image is constructed to depict spatial variations. The scanning pattern of the electron beam provides information about its position. In this study, microstructural analysis of the synthesized specimens was conducted using the FEI model 'Quanta 200F' scanning electron microscope. The electron gun functioned at an acceleration voltage of 15 KV using 40 nA probe current. The working distance was kept at 10 mm. Micrographs were captured in the scattered electron (SE) mode, ranging from low to high magnification. The average grain size of the synthesized samples was determined using "ImageJ software".

2.2.2.3 Energy-dispersive X-ray Spectroscopy (EDX)

Energy-Dispersive X-ray Spectroscopy (EDX) involves the quantitative analysis of various elements present in prepared samples. Typically, integrated with SEM or TEM microscopes, EDX functions by directing a high-energy electron beam onto the sample surface. This action energizes the atoms, causing electrons in their inner shells to be excited and ejected. Consequently, outer shells electron fills these vacancies, emitting characteristic X-rays. These emitted X-rays are specific to the atomic structure of each element and facilitate element identification. The energy of emitted X-rays is captured by a detector and plotted as an EDX spectrum. In this study, EDX results are coupled with SEM microscopy analysis.

2.2.2.4 Transmission Electron Microscopy (TEM)

Transmission electron microscopy (TEM) is a technique employed to scrutinize the size, shape, and morphology of samples at higher magnifications. It employs a high-voltage, high-energy electron beam directed onto the sample surface. Transmitted electrons are gathered and scrutinized to generate images. Transmission electron microscopy (TEM) utilizes a beam of electrons transmitted through the material to generate an image and diffraction pattern. The sample is typically a suspension on a grid in the form of thin film of thickness approximately less than 10 μm. As the electron beam traverses the specimen, interactions with the electrons produce an image. An imaging device, such as a fluorescent screen coupled to a charge-coupled device, is employed to magnify and focus the resulting image. TEM utilizes electrons as the "light source," leveraging their significantly smaller de Broglie wavelength to achieve a resolution thousands of times finer than that attainable with a light microscope.

In this study, the FEI make model ‘FEI Tecnai G220 s-Twin’ TEM machine operated at 300 KV was employed to examine the morphology, selected-area electron diffraction (SAED)

patterns, and fringes images of the synthesized samples using carbon-coated grids (CF200-Cu).

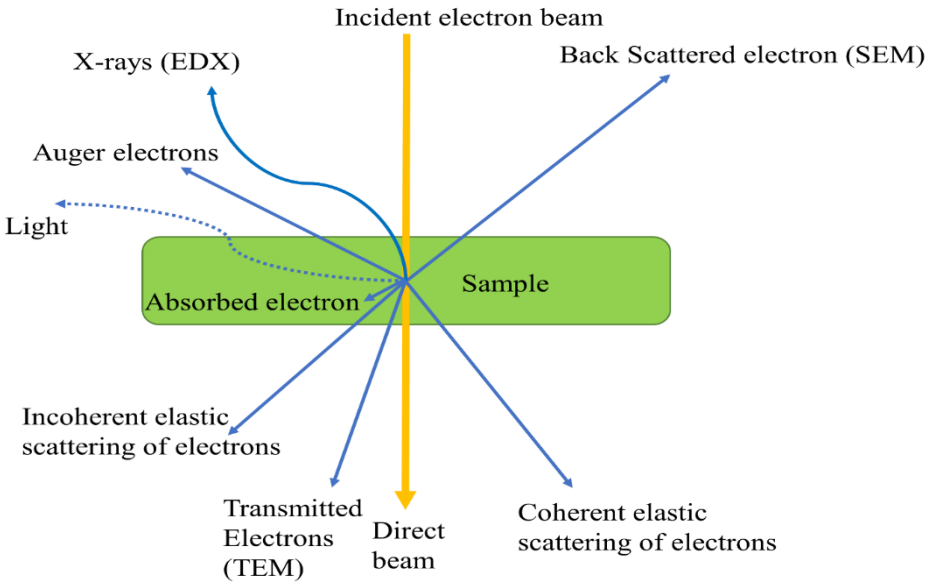

Figure 2.8 Representation of electron beam and sample interaction.

2.2.3 Vibrational Characterization

2.2.3.1 Raman spectroscopy

Raman spectroscopy serves as a highly dependable spectroscopic technique for examining phase purity and the composition of chemical species based on their vibrational modes. The Raman Effect in solids stems when incident light scatters due to the vibrations of bonds within the material, which are also referred to as phonons or modes of the medium. In Raman scattering, a light photon with a certain frequency (ω_i) and wave vector (K_i) interacts with the lattice, it exchanges energy (electron-radiation interaction) and generate an electron-hole pair. These electrons recombine with the hole, producing (or annihilating) a phonon of frequency ω (and wave vector K) via electron-lattice interaction. As a consequence, the scattered light undergoes a change in energy, either losing or gaining it, based on whether a phonon is created or destroyed. If the frequency of the scattered photon is ω_s and

corresponding wave vector is K_s , then energy and wave vector conservation lead to the following relation:

$$\omega_i = \omega_s \pm \omega \tag{2.2}$$

$$K_i = K_s \pm K \tag{2.3}$$

If ω_s is smaller (or larger) than the incident photon frequency (ω_i), it is termed stokes (or anti-Stokes) scattering. The difference in the incident photon frequency (often expressed in wavenumber, cm^{-1}), (ω_i - ω), is referred to as the Raman shift. By measuring the Raman shift, which is the change in energy of the scattered light compared to the incident laser, characteristic vibrational energy values of a solid can be obtained and represented in its Raman spectrum. The basic principle of Raman spectrum has been shown in Fig. 2.9. A Raman spectrum typically exhibits sharp peaks corresponding to different vibrational frequencies. However, in complex molecules, identifying these peaks becomes challenging as multiple peaks may merge into complex bands. Analyzing frequency shifts in the spectrum reveals characteristic vibration frequencies of atoms, aiding in determining the chemical composition and structure of the material.

In this study, Raman scattering measurements were conducted in the backscattering geometry on multiferroic thin film samples using a Raman Spectrophotometer, Renishaw Invia make Raman Microscope, equipped with a charge-coupled device (CCD) detector.

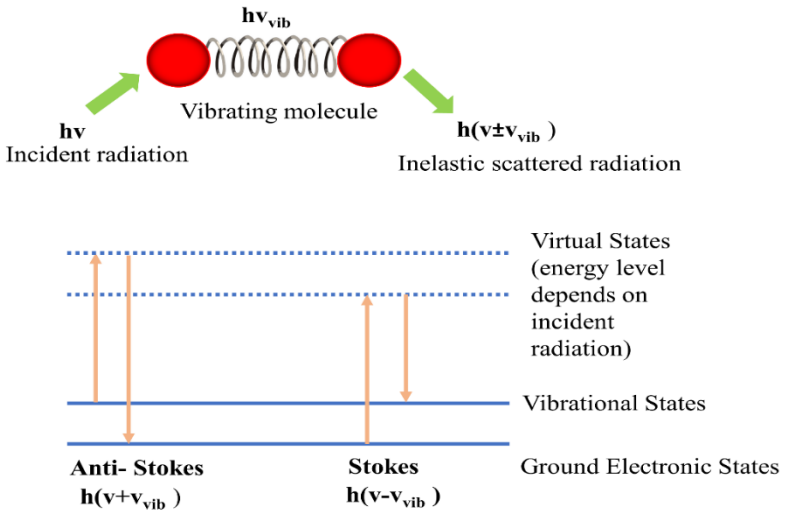

Figure 2.9 Principle of the Raman Spectra.

2.2.3.2 Fourier Transform Infrared Spectroscopy (FTIR)

Fourier Transform Infrared Spectroscopy (FTIR) enables the acquisition of infrared spectra from solids, liquids, or gases. FTIR spectrometers collect comprehensive spectral data over a wide range of wavelengths at once, providing a notable advantage compared to dispersive spectrometers. Absorption spectroscopy quantifies the light absorbed by a sample at various wavelengths. The term "Fourier transform infrared spectroscopy" refers to the mathematical procedure used to transform raw data into a true spectrum.

Alternatively, Fourier Transform Spectroscopy emits a beam containing multiple frequencies of light simultaneously and analyzes the absorption by the sample. This method differs from shining a monochromatic beam of light on the sample. Multiple data points are generated by varying the frequencies in the beam, and this process is rapidly repeated several times. Subsequently, a computer utilizes this information to calculate absorbance at each wavelength in reverse. In this study, FTIR spectra were recorded under an attenuated total reflectance (ATR) mode using a PERKIN ELMER make Spectrum 2 spectrometer in the wide range of spectrum 4000–400 cm^{-1}.

2.2.3.3 Electrical Characterizations

Electrical conductivity describes the flow of current in a material in response to an applied electrical field. Conduction in materials can transpire through one of three processes contingent upon the type of carriers within the material;

• Ionic conduction entails the movement of ions (atoms with positive or negative charges) from one site to another via point defects known as vacancies in the crystal lattice. Typically, at ambient temperature, ion hopping is minimal as atoms are in low-energy states. However, at elevated temperatures, vacancies become mobile, leading to fast ionic conduction in certain ceramics.

• Molionic conduction involves the movement of molecular ions (molions). This type of conduction is commonly observed in amorphous or liquid dielectrics.

• Electronic conduction arises from the movement of free charges (holes and/or electrons) within the solid.

Conduction in metals and resistors adheres well to Ohm's Law (V=IR). In these materials, electrical conductivity may involve both electronic and ionic charge carriers.

The total conductivity (σ) of a material comprises both DC conductivity (σ_{DC}) and AC conductivity (σ_{AC}), expressed as:

$$\sigma = \sigma_{DC} + \sigma_{AC} \tag{2.4}$$

The DC conductivity (σ_{DC}) and DC resistance (R_{DC}) were measured at room temperature using the Kiethley 6430 sub-Femtoamp source meter. Temperature-dependent studies were conducted using the same setup to determine the activation energy (Ea) for all prepared samples. Voltage and current values for all samples were recorded within the range of -10

to 10 V at room temperature, and I-V curves were plotted to calculate DC resistances. These I-V curves adhere to Ohm's law, represented by the equation:

$$V = I * R \tag{2.5}$$

Where, V denotes the applied voltage across the sample, I represents the current flowing through the sample, and R stands for resistance. The slope of the I-V curves provides the value of DC resistance, while DC conductivity (σ_{DC}) is calculated using the equation:

$$\sigma_{DC} = \frac{L}{R\,A} \tag{2.6}$$

where L denotes the thickness of the pellet, R signifies the DC resistance, and A represents the area of the pellet in cm, ohms, and cm^2, respectively.

2.2.4 Electrochemical Characterization

2.2.4.1 Electrode Preparation

For electrochemical investigations, the synthesized anode materials were combined with conductive carbon (Super P) and binder (polyvinylidene difluoride, PVDF) in a weight ratio of 70:15:15 in N-methyl-2-pyrrolidinone (NMP) solvent. The resulting slurry was then applied onto a thin sheet of Cu-foil, serving as a current collector, using the automatic coating unit. After drying, the disk electrodes of 16 mm diameter were punched and, then the electrodes were pressed between two stainless steel twin rollers to improve adherence between active material and current collector. The schematic diagram for slurry and electrode preparation has been shown in Fig. 2.10.

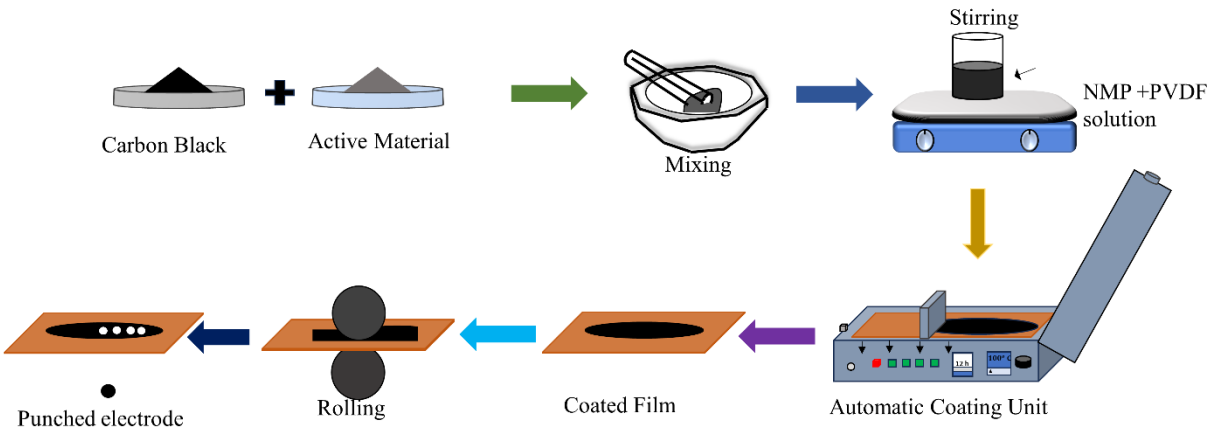

Figure 2.10 Schematic for the slurry and electrode preparation.

2.2.4.2 Coin Cell Assembly

The punched electrodes were then dried in vacuum oven and transferred into the Mbraun make glove box workstation keeping the O_2 and H_2O levels ≤0.5 ppm. Coin cells (CR2016) were fabricated to conduct electrochemical tests of the prepared electrodes. A microporous polypropylene sheet (Celgard 2400) served as a separator, and 1 M in EC: DMC 1:1 v/v was utilized as the electrolyte. High-purity Li chips were employed as reference electrode.

The coin cell assembly is followed by the sequence as: active material electrode, separator soaked in electrolyte, and Li metal chip. A spacer was placed on top of the electrode. Finally, the coin cell lid was crimped using manual crimper. Subsequently, all the cells were allowed to rest until a stable open circuit voltage (OCV) was reached to further test electrochemical performance like EIS, CV, GCD, etc. Figure 2.11 shows the schematic diagram illustrating the coin-cell assembly.

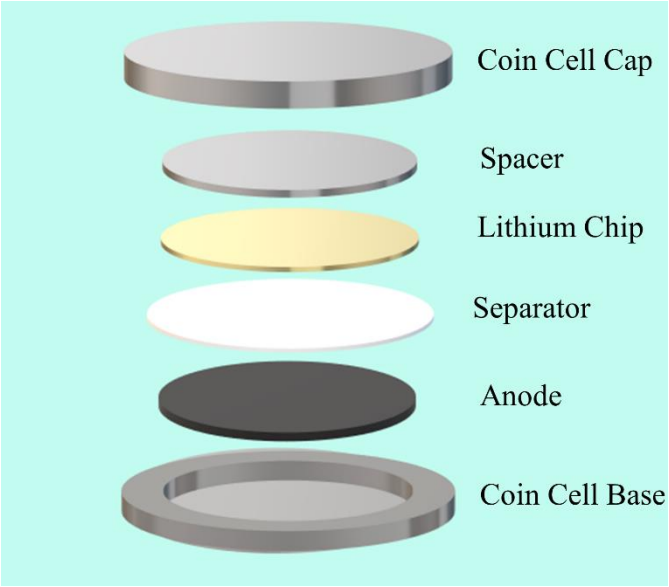

Figure 2.11 Representation of Coin cell assembly.

2.2.4.3 Galvanostatic Charge-Discharge (GCD)

Li metal has been used as a counter electrode due to its potential stability and abundant Li source, when characterizing anode material in half-cell coin batteries, Lithium metal is used for reference. In galvanostatic mode, a steady electric current with reversing direction at cut off potential is provided to the half-cell, while the voltage is monitored as lithium ions are inserted in and out of the electrodes. The direction of current is reversed at cut off potentials. This technique allows determination of electrode characteristics such as discharge capacity and rate capability. Anode materials are characterized in CR2016 half-cells using a VMP3 multichannel potentiastat supplied by Biologic and Neware Battery Testing System from voltage 0.01 to 3.0 V vs. Li metal counter electrode (anode).

2.2.4.4 Cyclic Voltammetry (CV)

Cyclic Voltammetry (CV) is a potentio-dynamic electrochemical technique widely used for its simplicity and informational richness. During CV testing, a cyclic linear potential scan is applied to the electrode, and the resulting current is monitored as shown in Fig. 2.12 (a). This scan rate is typically denoted in volts per second (V/s). The cyclic voltammogram

illustrates the response of cell as current with change in voltage as shown in Fig. 2.12 (b), providing insights into the kinetics and thermodynamics of the electrode reaction. The technique operates on the principle of linear sweep voltammetry, where the relation of working electrode and reference electrode are linearly dependent. The resulting current at the working electrode is measured. In cyclic voltammetry (CV) testing, the voltage is scanned from E_1 to E_2, (where, $E_1<E_2$) and then reversed back to E_1, with the current being recorded across multiple cycles. CV is particularly useful for revealing diffusion-controlled processes, such as the insertion of electro-active species into the electrode. In summary, CV is a convenient tool for qualitatively assessing reduction potentials and formation constant assessing electron transfer processes.

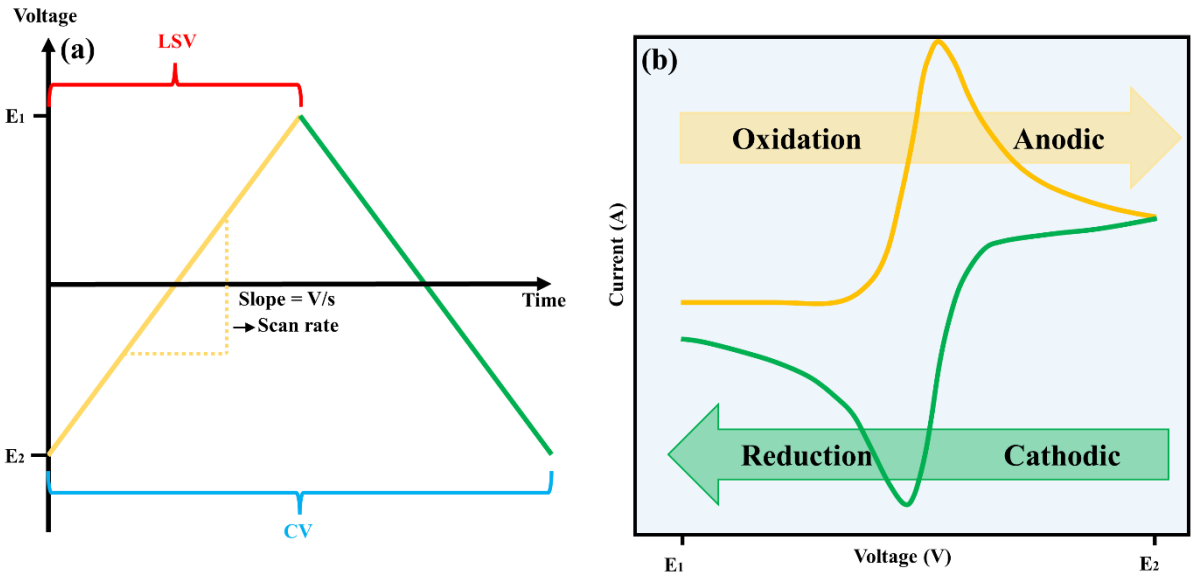

Figure 2.12 (a) Potential as a function of time (b) Current as a function of voltage for a typical cyclic voltammogram.

2.2.4.5 Electrochemical Impedance Spectroscopy (EIS)

EIS serves as a potent tool for analyzing electrochemical systems of considerable complexity. This characterization gauges the impedance across a spectrum of frequency, relying on the frequency-dependent nature of electrochemical cell impedance, by opposing

the flow of AC current within a complex system. EIS data is typically expressed as a combination of real and imaginary parts. Plotting the real component on the x-axis and the imaginary component on the y-axis generates a "Nyquist plot." These plots can be interpreted using equivalent circuits (EC), providing the kinetic behavior and diffusion parameters within an electrochemical system.

EIS analysis has found extensive application in investigating the reversible lithium intercalation into electrodes for Lithium-ion Batteries (LIBs). Nyquist plots typically consist of a semicircle at high to medium frequencies and an inclined straight line at lower frequencies. R_s (intercept at x-axis) denotes the resistance due electrolyte and electrode material, whereas Z_W represents the Warburg impedance and it corresponds to the tail at low frequency. The semicircle in the mid-frequency range predominantly reflects the electrochemical reactions transpiring at the interface, signifying the charge transfer resistance (R_{ct}) of the electrochemical system. A Constant Phase Element (CPE) represents the non-ideal behavior of a capacitor formed between the electrode and the electrolyte. Finally, the inclined line in the low-frequency region represents the Warburg impedance (Z_w), associated with Li-ion diffusion within the electrode's active material. The fundamental circuit model, known as the Randles model, consists of a polarization resistor (R_s) and a bulk resistor (R_{ct}) connected in series, along with a parallel connection of double layer capacitance (C). A Biologic make multi-channel cycler was utilized for EIS characterization. In this study, EIS data was collected using 5 mV AC pulses over a frequency range of 100 kHz to 10 MHz.

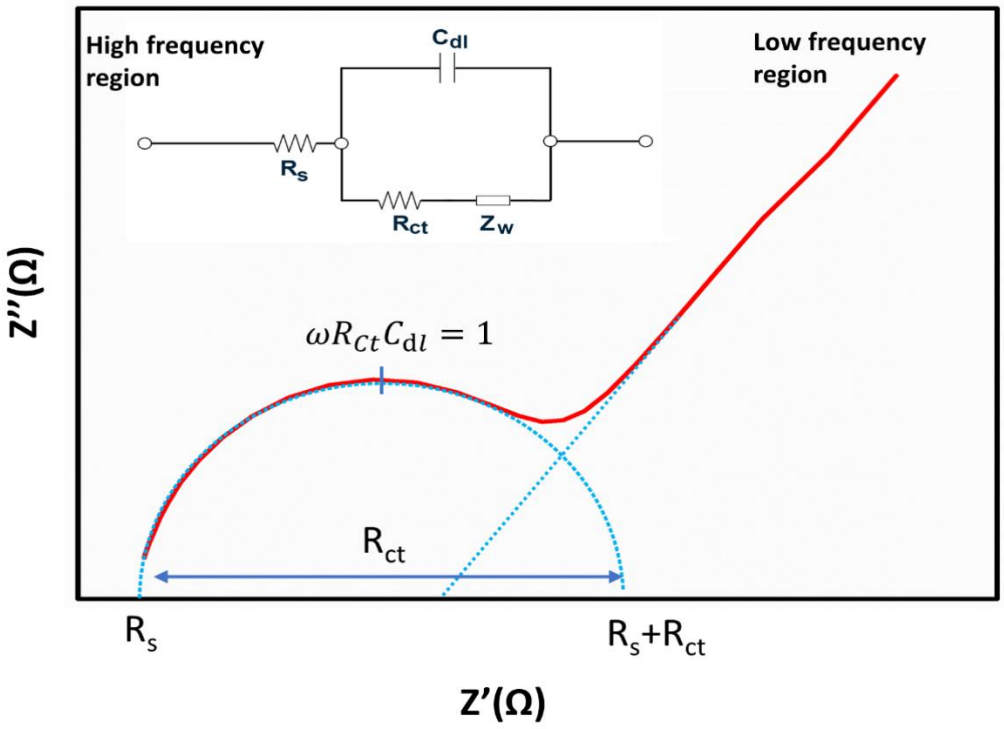

Figure 2.13 Simple Randles equivalent circuit and Nyquist plot for an electrochemical cell.

Chapter 3 : Electrochemical performance and Li-ion diffusion analysis of SnSe/C SnSe/MWCNT composite as anode materials

In this chapter, synthesis and electrochemical analysis of SnSe based alternative alloy type anode and its composites with Super P (SnSe/C) and MWCNT (SnSe/MWCNT) have been attempted via a facile high-energy ball milling method. Among all three developed anode materials, SnSe/MWCNT showed higher values of Li-ion diffusion coefficient, indicating that the SnSe/MWCNT electrode has superior kinetics over SnSe/C and bare SnSe.

3.1 Introduction

The elements belonging to group IV like Si, Ge and Sn have proven themselves among the favourable anode materials owing to their higher specific capacities in comparison with carbon-based anode material. Out of these anode materials, tin has gained immense attention due to its theoretical capacity of 994 $mAhg^{-1}$, high packaging density and safer thermodynamic potential in comparison to carbonaceous anode materials[121–123]. Metallic Sn undergoes an alloying reaction with lithium leading to the formation of $Li_{4.4}Sn$, incorporating 4.4 Li-ions per unit formula and it also has a higher electrochemical potential vs Li/Li^+ as compared to graphite, resulting to enhances its stability and safety as anode in Li-ion batteries. Furthermore, its relatively low cost and environmental friendliness make it ideal for commercial production. However, like many other anode materials, tin-based anodes experience significant volume changes of 250–300% during Li-ion intercalation and de-intercalation. This can result in grain degradation, electrical disconnection, and significant capacity fading[123–125]. Nanosized materials could present a viable solution by better accommodating strain and enhancing specific capacity and rate capability, owing to their increased interfacial area and improved Li-ion diffusion kinetics[126]. Sn easily reacts with elements of group VA and group VI A to form binary or ternary compounds (Sn-M, Sn-M-M'). Hence, one such approach is to make alloy of Sn with inactive materials that could hinder the expansion/shrinkage of volume during charging or discharging such as Sn-Sb, Sn-Co, Sn-Ni, Sn-Cu etc. Another approach could be composites with conductive materials such as carbon, polypyrrole, polyaniline to enhance electrochemical performance[126,127].

In this chapter, SnSe alloy and its composites with Super P and multi walled carbon nanotubes (MWCNTs) have been synthesized via high energy ball mill method using Tin and Selenium metal powder, Super P and MWCNTs as precursors. Super P and MWCNTs are among the most carbonaceous materials with characteristics like high electronic conductivity, high thermal stability and mechanical properties. MWCNTs are widely used to make composites with anode materials owing to its excellent properties which enhances the cyclic performances of LIBs by preventing them from collapsing after long cycles and decreasing the volume expansion during cycling maintaining structural integrity. Super P acts as a buffer when used in anode material to suppress the volume change during lithiation/de-lithiation process.

Synthesis of SnSe, SnSe/C and SnSe/MWCNT has been carried out via High Energy Ball Mill (HEBM) route as mentioned in Chapter 2 section 2.1.1.1. Moreover, physicochemical, electrical and electrochemical characterizations of SnSe, SnSe/C and SnSe/MWCNT materials are performed and explained in Chapter 2 section.

3.2 Results and Discussion

3.2.1 Structure and Morphological Analysis

3.2.1.1 X-ray Diffraction (XRD) Analysis

The wide scan XRD patterns of synthesized SnSe, SnSe/C and SnSe/MWCNT samples are shown in Fig. 3.1 along with the individual super P and MWCNT XRD patterns. All obtained peaks in the XRD pattern are assigned to 25.20^{o} (201), 26.45^{o} (210), 29.42^{o} (011), 30.40^{o} (111), 31.08^{o} (400), 37.20^{o} (311), 43.34^{o} (411), 47.30^{o} (302), 49.60^{o} (511) and 54.47^{o} (420) planes of SnSe. These peaks match well with the peaks in JCPDS file: 00-048-1224 and confirm an orthorhombic structure with space group, pnma. No extra diffraction peaks are noticed. Hence, the XRD patterns confirm the high purity of the SnSe/C and SnSe/MWCNT

composite in proper phase. It also indicates that the addition of Super P or MWCNT has no effect on the phase formation of SnSe and does not affect the crystal structure of SnSe. Also, no oxidation reaction took place during the synthesis process[128]. The average crystallite size of the SnSe, SnSe/C and SnSe/MWCNT composites has been estimated using Scherrer's formula given as:

$$D = \frac{k\lambda}{\beta cos\theta} \tag{3.1}$$

where D, β, λ, k and θ represents crystallite size, FWHM, wavelength of the X-rays radiation, $CuK_{\alpha 1}$ (0.154nm), shape constant (~ 0.9) and Bragg's angle, respectively[79]. The dislocation density, δ represents the deficiency in the particles can be calculated using the formula given below;

$$\delta = \frac{1}{D^2} \tag{3.2}$$

Table 3.1 summarizes the calculated values obtained from the XRD analysis.

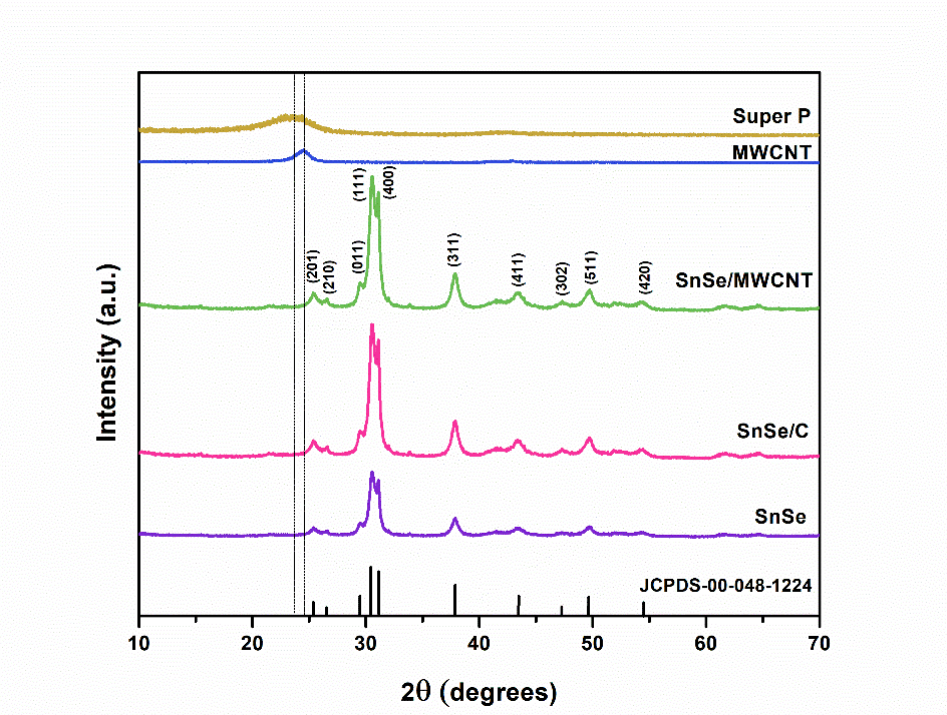

Figure 3.1 XRD patterns of SnSe, SnSe/C and SnSe/MWCNT along with super P and MWCNT prepared using solid state HEBM method.

Table 3.1 Average Crystallite size for SnSe, SnSe/C and SnSe/MWCNT.

Parameter	SnSe	SnSe/C	SnSe/MWCNT
D(nm)	42	23	26
δ (nm^{-2})×10^{-3}	0.56	1.89	1.47

3.2.1.2 Scanning Electron Microscopy (SEM) and Energy Dispersive X-ray Spectroscopy (EDX) Analysis

Figure 3.2 shows the FESEM images of the SnSe, SnSe/C and SnSe/MWCNT. As displayed in Fig. 3.2 (a-b), SnSe consist of irregularly shaped micro-sized particles with the average particle size of 0.65 μm consisting of agglomerated primary nanoparticles. However, the addition of Super P enhances the morphology and regularity of SnSe particles as shown in Fig. 3.2(c-d). The SnSe/C composite also showed the aggregated and nearly spherical shaped particles with an average particle size of 0.1 μm with the agglomerated nanoparticle. Such morphology is quite good for electrode materials because the agglomeration of primary nanoparticles may increase the adherence between the electrode and the electrolyte, hence enhancing the battery performance. Whereas, SnSe/MWCNT composite shows slightly larger irregular shaped micro-sized particles. The average size of particles was found to be 0.3 μm. MWCNTs have cylindrical thread-like structure which gives large interlayer spacing hence promoting better exchange of Li-ion in/out of the electrode material. Furthermore, the structure of MWCNTS is such that it does not deform even after multiple charge-discharge, making it as an excellent anode. As can be seen from Fig. 3.2 (d-e), the SnSe/MWCNT composite consist of SnSe particles well surrounded by clusters and bundles of MWCNT and some of the SnSe particles are well covered by MWCNT. Hence, the composite structure may help to reduce the damage of SnSe structure during cycling giving excellent electrochemical performance as compared to bare SnSe[79].

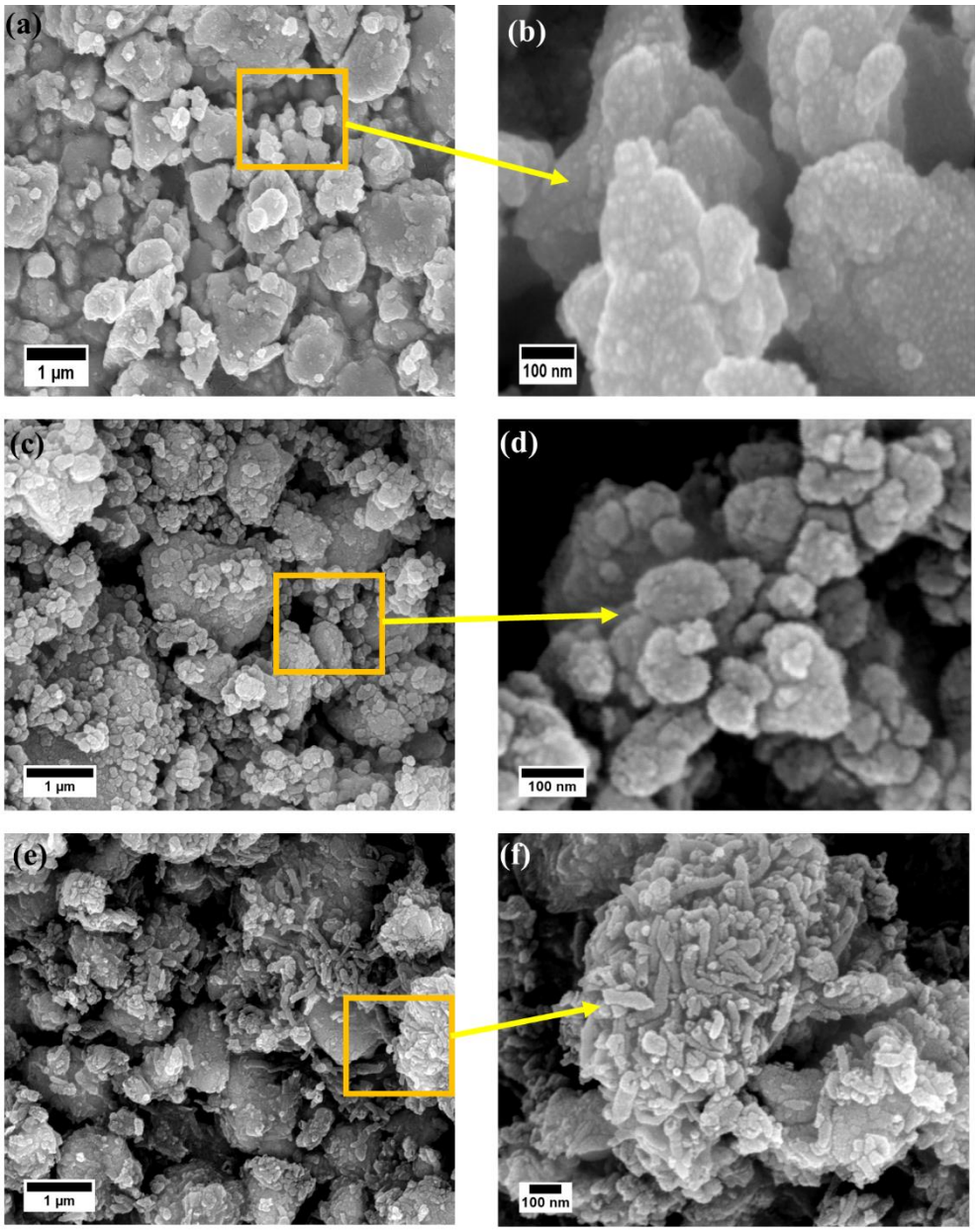

Figure 3.2 FESEM micrographs of (a-b) SnSe, (c-d) SnSe/C, (e-f) SnSe/MWCNT prepared using solid state HEBM method.

Figure 3.3 (a-e) depicts the elemental mapping of SnSe/C, images of the EDS mapping proves that SnSe and Super P was homogeneously mixed in the sample. Figure 3.3 (f-j) shows elemental mapping of SnSe/MWCNT confirming the uniform distribution of Sn, Se and MWCNT throughout the prepared sample.

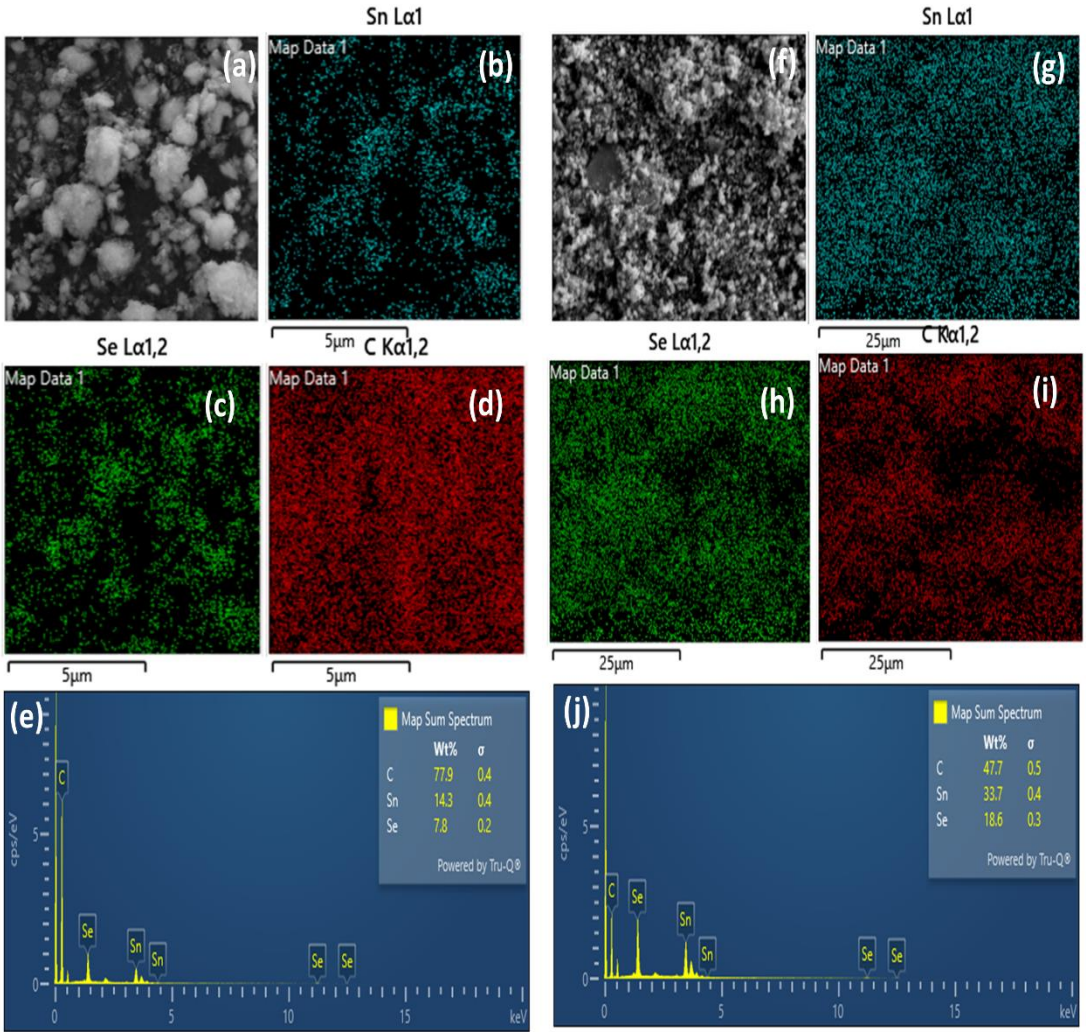

Figure 3.3 Elemental mapping images of Sn(blue), Se(green), C (Red) of (a-d) SnSe/C composite, (f-i) SnSe/MWCNT, (e) the result of EDS analysis for SnSe/C, (j) the result of EDS analysis for SnSe/MWCNT.

3.2.1.3 Raman Analysis

To further confirm the presence of carbon and MWCNT in the composites of SnSe, Raman spectra for the prepared sample were carried out. Raman spectrum of SnSe, SnSe/C, SnSe/MWCNT, Super P and MWCNT are shown in Fig. 3.4. It can be depicted from the

Fig. 3.4, the Raman spectra of Super P and MWCNT shows two broad peaks close to 1340 cm^{-1} and 1580 cm^{-1}. The carbon D band at 1340 $cm^{-1}$is due to the disordered structure or defects in carbon, whereas G band at 1580 cm^{-1} is attributed to the stretching of carbon-carbon bond and is found in all sp^2 carbon materials. Hence, the Raman spectra of SnSe/C and SnSe/MWCNT composite indicate the presence of two D and G bands, while these bands are absent in bare SnSe confirming the presence of carbon in SnSe/C and SnSe/MWCNT composites[129].

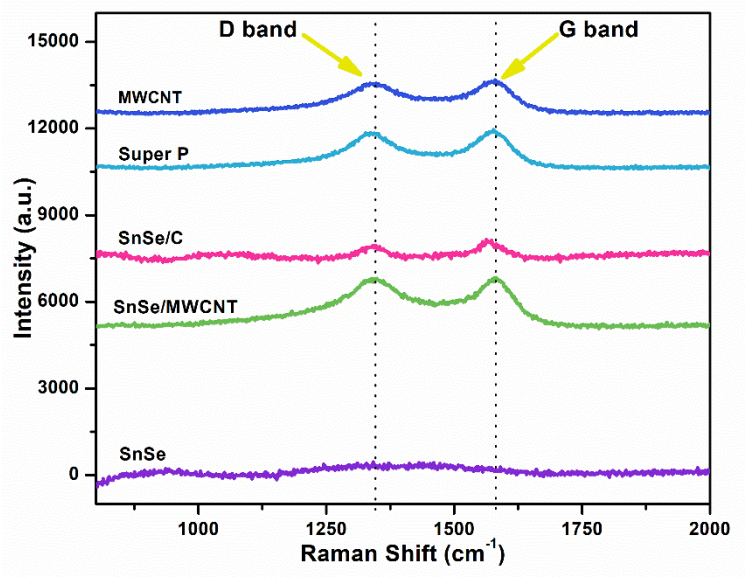

Figure 3.4 Raman Spectra of MWCNT, Super P, SnSe, SnSe/C and SnSe/MWCNT Composite.

3.2.1.4 Conductivity Measurement

The effect of temperature on electrical conductivity was investigated for the synthesized samples. Figure 3.5 (a) illustrates an Arrhenius plot, in which ln (σ_{DC}) is plotted against the reciprocal of temperature for SnSe, SnSe/C and SnSe/MWCNT. The slope of curves yields the activation energy for the synthesized samples. The Arrhenius equation in its functional form can be expressed as:

$$\sigma_{DC} = \sigma_o exp \frac{-E_a}{K_B T} \tag{3.3}$$

Here, K_B, T, and E_a denotes Boltzmann constant, absolute temperature and activation energy, respectively.

The electronic conductivity, σ_{DC} was calculated at room temperature using the following equation:

$$\sigma_{DC} = \frac{1}{R}\left(\frac{L}{A}\right) \tag{3.4}$$

Where, R, L and A represents resistance of the sample, thickness of the pellet and the area of the pellet, respectively[130]. Figure 3.5 (b) shows I-V characteristic curve for SnSe, SnSe/C and SnSe/MWCNT at room temperature. The DC resistance value has been calculated using the slope of the I-V Curve. Hence, the DC conductivity has been estimated. It has been observed that conductivity increases with an increase in temperature, showing a semiconducting behaviour. Among the three tested materials, SnSe/MWCNT have the lowest activation energy and the highest conductivity. This may help in enhancing the electrochemical performance of developed SnSe/MWCNT as anode material. The calculated values of DC resistance, DC conductivity and activation energy are shown in Table 3.2.

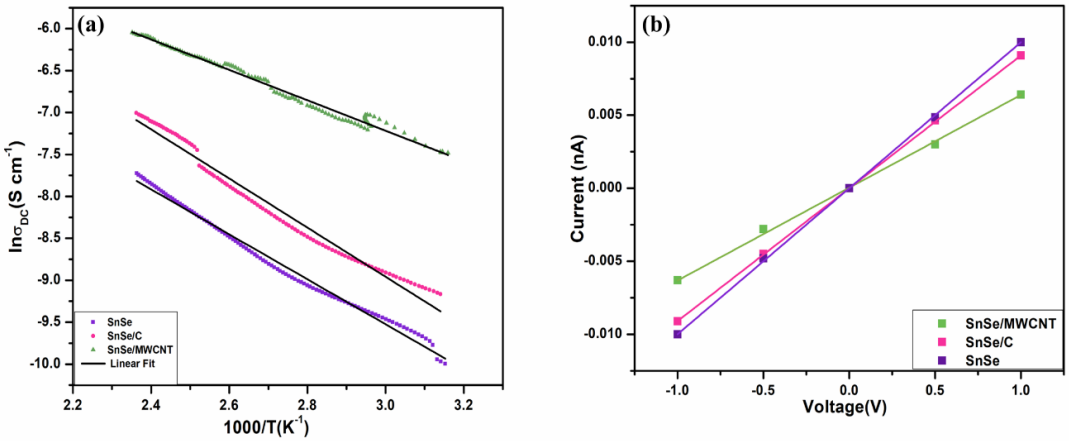

Figure 3.5 (a) Variation of conductivity ($\ln\sigma_{DC}$) with temperature (1000/T) for SnSe, SnSe/C and SnSe/MWCNT (b) I-V curve at room temperature for SnSe, SnSe/C and SnSe/MWCNT.

Table 3.2 Calculated DC conductivity values of SnSe, SnSe/C and SnSe/MWCNT.

Sample	Activation Energy (meV)	DC resistance (Ω)	DC Conductivity (S/cm)
SnSe	232	10×10^{6}	9.76×10^{-9}
SnSe/C	229	9.1×10^{6}	2.44×10^{-8}
SnSe/MWCNT	157	6.36×10^{6}	1.86×10^{-7}

3.2.2 Electrochemical Analysis

3.2.2.1 Cyclic Voltammetry (CV) Analysis

Cyclic voltammetry measurements of SnSe, SnSe/C, SnSe/MWCNT anodes are obtained at 0.2 mV/s scan rate in the voltage window of 0.01 to 2.5 V for the first four cycles and are shown in Fig. 3.6 (a-c). During the initial cathodic scan, SnSe, SnSe/C and SnSe/MWCNT show a sharp peak at around 1.02V, 1.21V and 1.05V, respectively. This could be due to the conversion reaction of SnSe into Sn and Li_2Se. However, in the proceeding cycles this cathodic peak is shifted to 1.26V for SnSe/C and SnSe/MWCNT and vanishes in the case of bare SnSe indicating that this conversion reaction is irreversible in bare SnSe anode. On further discharging, another reduction peak is observed around 0.5 V- 0.6 V, it occurs probably due to the decomposition of electrolyte and hence forming Solid Electrolyte Interface (SEI) layer on the electrode surface. The peak around 0.06-0.21V may be ascribed possibly due to the alloying of Sn with Li to form Li_xSn (where $x \geq 4.4$). For initial oxidation scan, the observed peaks between 0.5V to 0.63V can be attributed to the de-alloying process of Li_xSn. However, small peaks arising in SnSe/C and SnSe/MWCNT electrodes at 1.8V and 2.2V could be due to the re-oxidisation of Sn and Li_2Se to form SnSe and extraction of Li-ion. This is supplemented by the reduction peak at 2.02V and repetition of these anodic peaks in the subsequent cycles. Hence, it implies that in composite anodes, the

decomposition of SnSe is a reversible process which is occurring due to the addition of Super P and MWCNT[131]. It is well known that carbon source in the composite can decreases the polarisation promoting the better insertion/de-insertion of Li-ions in the electrode[132]. Moreover, the CV profile of SnSe/C shows suppression of Li_2Se phase as compared to SnSe and SnSe/MWCNT, this could indicate that at the equilibrium potential range, there is little retardation of the decomposition reaction. It could be due to the amorphous carbon (Super P) used in the composition SnSe/C. Moreover, there are only few reports related to this mechanism[133]. As can be seen from CV graphs, SnSe/MWCNT shows the best repeatability as compared to SnSe and SnSe/C.

The lithiation and de-lithiation reaction mechanism of SnSe, SnSe/C and SnSe/MWCNT are as follows:

Lithiation process for SnSe, SnSe/C and SnSe/MWCNT

$$SnSe + 2Li^+ + 2e^- \rightarrow Sn + Li_2Se \quad (3.5)$$

$$Sn + xLi^+ + xe^- + Li_2Se \rightarrow Li_xSn + Li_2Se \ (0 \leq x \leq 4.4) \quad (3.6)$$

De-lithiation for SnSe,

$$Li_xSn + Li_2Se \rightarrow Sn + Li_2Se + xLi^+ + xe^- \quad (3.7)$$

De-lithiation for SnSe/C and SnSe/MWCNT,

$$Li_xSn + Li_2Se \rightarrow Sn + Li_2Se + xLi^+ + xe^- \quad (3.8)$$

$$Sn + Li_2Se \rightarrow Li_{2-y}SnSe + yLi^+ + ye^- \quad (3.9)$$

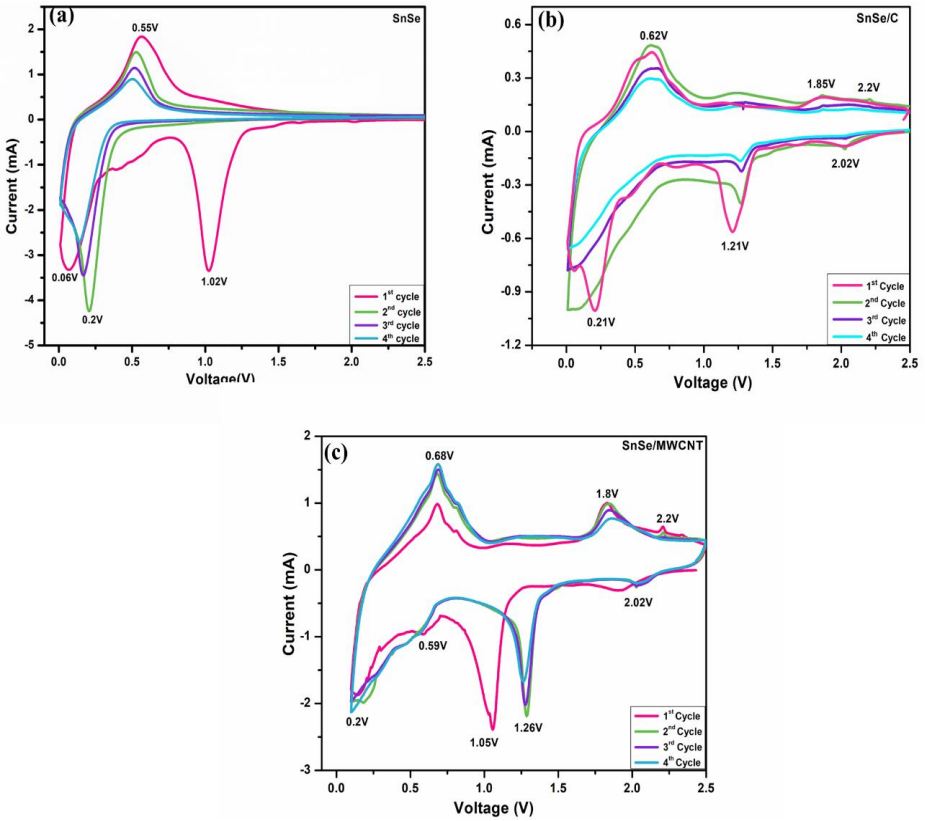

Figure 3.6 Cyclic voltammograms (CV) curves of (a) SnSe (b) SnSe/C (c) SnSe/MWCNT at 0.2mV/s scan rate from 0.01 to 2.5 V.

3.2.2.2 Scan Rate Analysis

Figure 3.7 (a-c) shows CV data of SnSe, SnSe/C and SnSe/MWCNT, respectively, at different scan rates of 0.05mV/s, 0.1mV/s and 0.2 mV/s. This test is used to study the dynamic behaviour, and to calculate the Li-ion diffusion coefficient in SnSe, SnSe/C and SnSe/MWCNT electrodes. On increasing scan rate, the peak intensities of cathodic and anodic reaction are also increased[134].

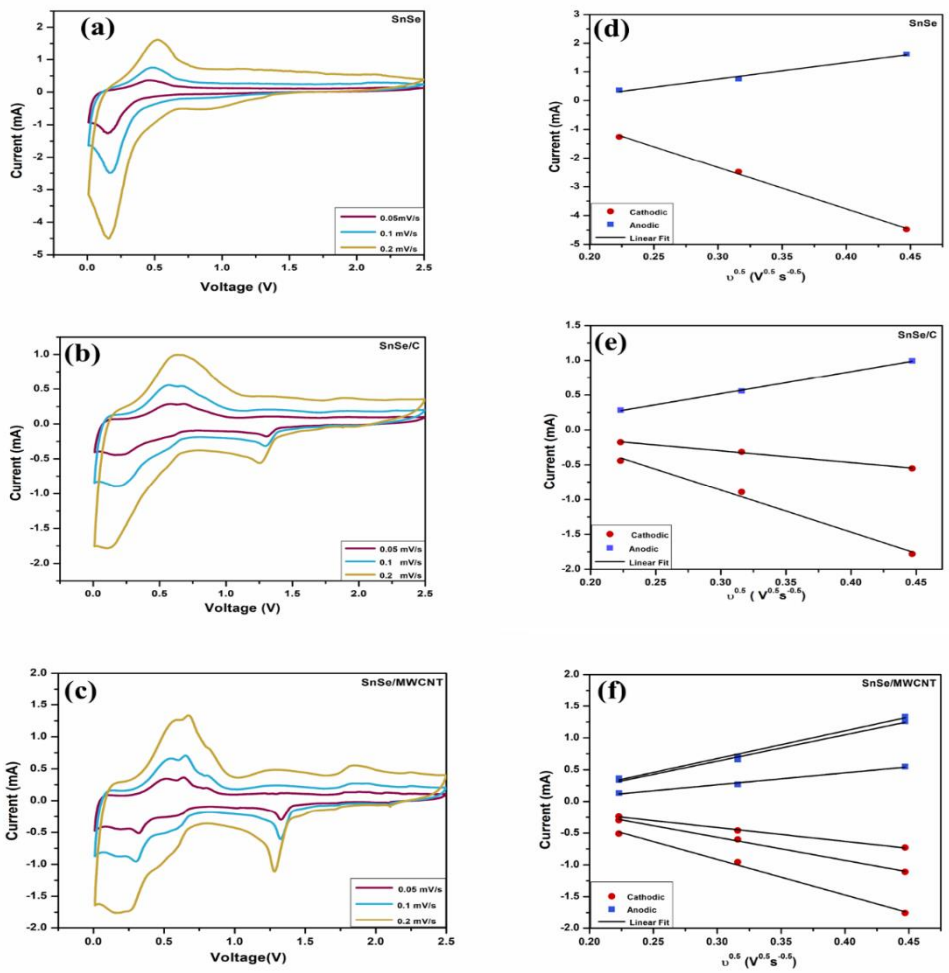

Figure 3.7 Cyclic Voltammetry at various scan rate of (a) SnSe (b) SnSe/C and (c) SnSe/MWCNT, cathodic and anodic peak current versus $\upsilon^{0.5}$, (d) SnSe (e)SnSe/C and (f) SnSe/MWCNT

For a diffusion-controlled process, the relation between the square root of scan rate ($\upsilon^{0.5}$) and peak current density (I_P) should be a linear one as shown in Fig. 3.7 (d-f). The Randles-Sevcik equation (3.10) is used to determine the relationship between scan rate and peak current density as well as the value of chemical diffusion coefficient[135].

$$I_P = 0.4463n^{3/2}F^{3/2}C_{Li^+} + AR^{-1}T^{-1}D_{(Li^+)^{1/2}}v^{1/2} \quad (3.10)$$

Where I_P, n, C_{Li^+}, A , F , R, T , υ and D_{Li^+} represents peak current density, charge transfer number, Li-ion concentration in electrodes, electrode area, Faraday's Constant, Gas Constant, absolute temperature, scan rate and diffusion coefficient, respectively[134].

Diffusion coefficient (D_{Li^+}) has been calculated around cathodic and anodic peaks for SnSe, SnSe/C and SnSe/MWCNT samples. All the calculated values of diffusion coefficient are given in Table 3.3. From the calculated values, it can be seen SnSe/MWCNT shows the higher diffusion coefficient as compared to SnSe/C and SnSe indicating the best diffusion properties.

Table 3.3 Calculated D_{Li^+} values of SnSe, SnSe/C and SnSe/MWCNT from Cyclic Voltammetry.

SnSe	**Anodic peak**			**Cathodic Peak**		
D_{Li^+} **(cm^2s^{-1})**	9.67×10^{-15}			2.44×10^{-15}		
SnSe/C	**Anodic Peak**			**Cathodic Peak**		
D_{Li^+} **(cm^2s^{-1})**	3×10^{-15}			0.83×10^{-15}	1.08×10^{-14}	
SnSe/MWCNT	**Anodic Peak**			**Cathodic Peak**		
D_{Li^+}**(cm^2s^{-1})**	1.05×10^{-15}	5.65×10^{-14}	5.11×10^{-14}	3.9×10^{-15}	1×10^{-14}	1.4×10^{-14}

3.2.2.3 Electrochemical Impedance Spectroscopy (EIS) Analysis

In order to investigate kinetic behaviours of bare SnSe, SnSe/C and SnSe/MWCNT, EIS was performed before cycling. EIS measurement is carried out to examine the prepared electrodes materials since the internal impedance of a cell is a vital characteristic that has a direct effect on its electrochemical performance. Figure 3.8 (a) shows the Nyquist plots of SnSe, SnSe/C and SnSe/MWCNT at open circuit voltage (OCV) measured in the frequency range of 10 mHz to 100kHz. Each spectrum at high to medium frequencies consists of a semicircle and a inclined straight line at lower frequencies. EIS analysis has been performed

using equivalent circuits with R, C and Q combination to fit the impedance data. The equivalent circuit is shown in Fig. 3.8 (inset), where R_s denotes the resistance due electrolyte and electrode material. R_{ct} represents the resistance due to electrode-electrolyte interface. R_{SEI} and C_{SEI} may arises due to the transfer of Li-ions through SEI layer and C_{dl} is the double layer capacitance, whereas Z_W represents the Warburg impedance and it corresponds to the tail at low frequency[79,128,136]. From EIS graphs, it can be seen that the SnSe/MWCNT has the smallest diameter of the semicircle as compared to SnSe/C and bare SnSe revealing that the charge transfers resistance (R_{ct}) for SnSe/MWCNT composite is much smaller than the SnSe, whereas the R_{ct} value of SnSe/C lies in between SnSe/MWCNT and SnSe. For SnSe/C composite, obtained R_{ct} value could be due to the conducting nature and dispersing effect of carbon, whereas for SnSe/MWCNT there is the easy transfer of Li-ions in the charge transfer process due to the tubular structure of MWCNT which may also improve the electrochemical performance of SnSe/MWCNT.

Figure 3.8 (b) shows the relationship plot between Z' and $\omega^{-0.5}$. The fitting results are shown in Table 3.4.

The diffusion coefficient in the bulk material can be calculated using the given equation:

$$D_{Li^+} = \frac{0.5R^2T^2}{A^2n^4F^4C^2{\sigma_\omega}^2} \tag{3.11}$$

Where D_{Li^+} , R , A, n, T, C, F and σ_ω is the Diffusion Coefficient (cm^2s^{-1}), Boltzmann Constant(8.314 J mol^{-1} K^{-1}), Electrode Area (cm^2), no. of electrons, absolute temperature (K), Li-ion concentration (mol $/cm^3$), Faraday's Constant and Warburg Factor ($\Omega\ s^{-1/2}$), respectively. The relationship of Z' and σ_ω is given below:

$$Z' = R_s + R_{ct} + \sigma_\omega\omega^{-1/2} \tag{3.12}$$

Equation (3.12) has been used to calculate the Warburg factor, σ_ω by using the slope of Bode plot. By substituting the values in equation (3.11), diffusion coefficient is

estimated[137,138]. The calculated values of D_{Li^+} have been listed in Table 3.4. The estimated values of D_{Li^+} from EIS are in accordance with the values observed from cyclic voltammetry. Hence, it supplements that the values of D_{Li^+} obtained from CV and EIS are in good agreement.

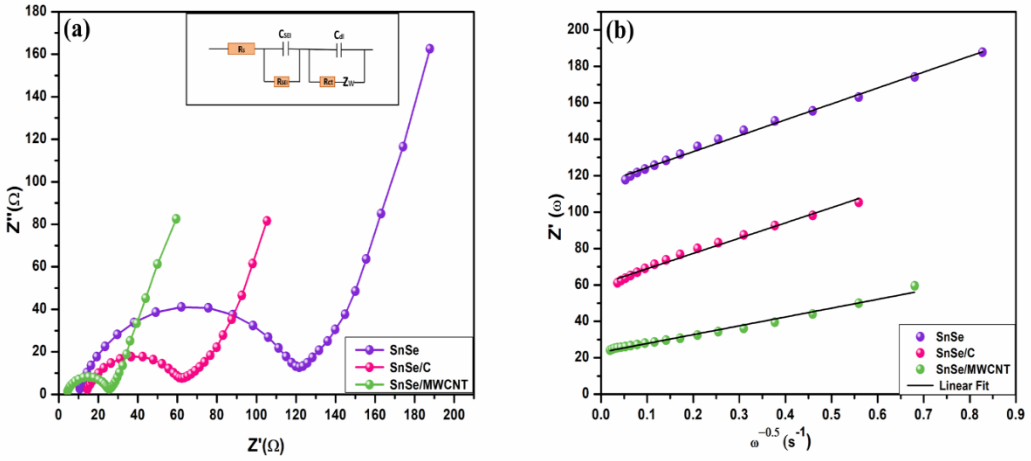

Figure 3.8 (a) Nyquist plots of SnSe, SnSe/C and SnSe/MWCNT (b) relationship between real part of resistance (Z') and inverse square root of angular frequency ($\omega^{-0.5}$).

Table 3. 4 Calculated D_{Li^+} values of SnSe, SnSe/C and SnSe/MWCNT from EIS Results.

Parameter	**SnSe**	**SnSe/C**	**SnSe/MWCNT**
R_s (Ω)	12	15	4
R_{ct} (Ω)	110	43	19
$D_{Li^+}(cm^2s^{-1})$	2×10^{-15}	2.19×10^{-15}	6.55×10^{-15}

3.2.2.4 Galvanostatic Charge Discharge (GCD) Analysis

Figure 3.9 (a) displays initial galvanostatic charge-discharge profiles of SnSe, SnSe/C and SnSe/MWCNT measured in the range 0.01 to 2.5 V at current density of 50 mAg^{-1}. During initial discharging, a common plateau is observed around 1.25 V in all three electrodes attributing to the decomposition of SnSe into Li_2Se and Sn followed by a slope at ~0.6 V

arising due to the development of the SEI layer. The slope around 0.3V is formed due to the alloying reaction of metallic Sn with Li. Whereas, during charging a slope at ~0.5V was noted in all three electrodes attributing to the de-alloying reaction of Li_2Sn. However, another slope is noticed at around 1.9 V arising due to the oxidation process of Sn and Li_2Se to form SnSe. After initial discharge cycle, the plateau at 1.25 V vanished in SnSe but not in SnSe/C and SnSe/MWCNT indicating that the decomposition of SnSe is reversible in SnSe/C and SnSe/MWCNT. The SnSe/MWCNT electrode showed highest initial discharging-charging capacity of 1107mAhg^{-1} - 955 mAhg^{-1} with coulombic efficiency of 86 %, while SnSe/C and SnSe electrode shows an initial discharging-charging capacity of 1069 mAhg^{-1} - 865 mAhg^{-1} and 910mAh/g-724 mAh/g with coulombic efficiency of 80 % and 79%, respectively. Figure 3.9 (b) shows the charge discharge curve of 10th cycle. SnSe discharge and charge capacity after 10 cycles were recorded as 384 mAhg^{-1} and 328 mAhg^{-1}, whereas SnSe/C and SnSe/MWCNT shows much higher values of charge-discharge of 617 mAhg^{-1} - 647 mAhg^{-1} and 678 mAhg^{-1} - 700 mAhg^{-1}, respectively even after 10 cycles. The higher capacity of SnSe/C and SnSe/MWCNT electrodes could be due to the lithiation/de-lithiation of Super P and MWCNT and reversible decomposition of SnSe in the composite.

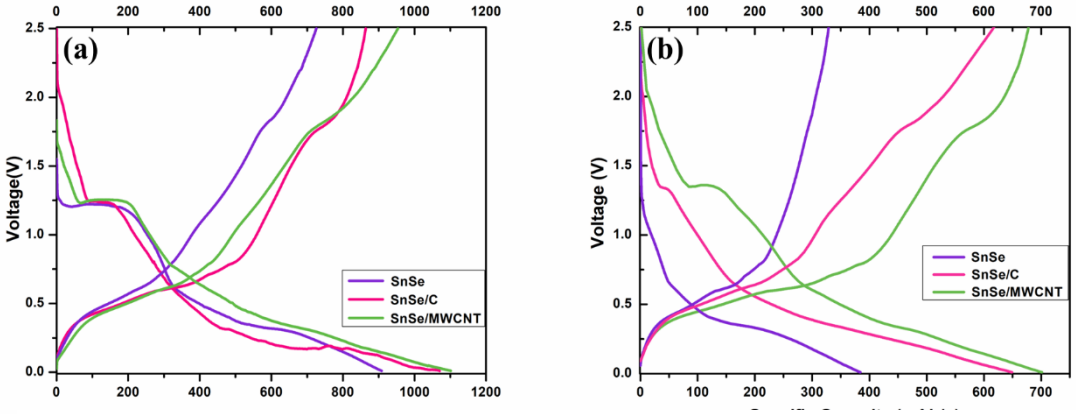

Figure 3. 9 Galvanostatic charge-discharge profiles of SnSe, SnSe/C and SnSe/MWCNT for (a) 1st cycle (b) 10th cycle.

Figure 3.10 (a) shows the rate performance of SnSe, SnSe/C and SnSe/MWCNT electrodes at different C-rates and the obtained discharge capacities are tabulated in Table 3.5. It can be observed, SnSe/MWCNT demonstrate best rate capability among all three electrodes at each current density. Figure 3.10 (b) shows the comparison of cycling behaviour of SnSe, SnSe/C, SnSe/MWCNT, Super P and MWCNT half cells at 500 mAg^{-1}. The SnSe electrode shows a rapid decay in capacity maintaining a capacity of 229 $mAhg^{-1}$ after 100 cycles. The reason of poor performance could be due to the structural and volumetric change during lithiation/de-lithiation of SnSe. Whereas, SnSe/C and SnSe/MWCNT shows better cycling performance maintaining capacity of 405 $mAhg^{-1}$ and 564 $mAhg^{-1}$ even after 100 cycles, respectively. The reason of improved cycling behaviour of SnSe/C could be attributed to the good dispersion of SnSe within Super P and the conducting, buffering effect of Super P. Whereas, the reason for better cycling behaviour of SnSe/MWCNT could be attributed to the tubular structure of MWCNTs that can alleviate volume change during cycling and reduce the pulverization of SnSe particles, thus preserving the connectivity of SnSe particles[131].

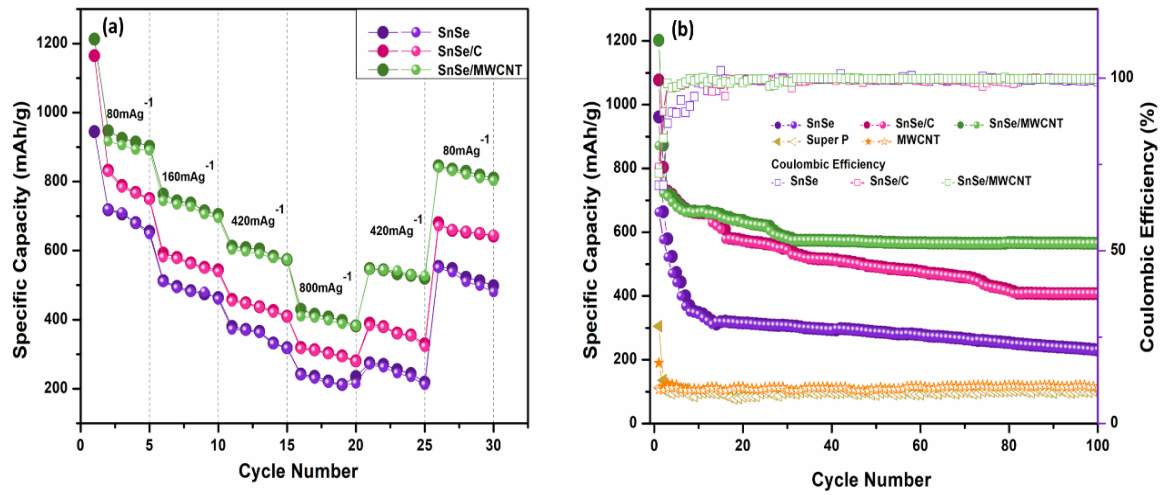

Figure 3.10 (a) Rate performance (b) Cycling performance of SnSe, SnSe/C and SnSe/MWCNT.

Moreover, the structure of MWCNTs is such that it decreases the Li-ion diffusion length which leads to enough electrode and electrolyte interphase to absorb Li-ions and lead to better kinetics.

Table 3.5 Specific discharge capacity of SnSe, SnSe/C and SnSe/MWCNT at various current density.

Specific Discharge Capacity ($mAhg^{-1}$)			
Current Density (mAg^{-1})	**SnSe**	**SnSe/C**	**SnSe/MWCNT**
80	557	648	799
160	462	537	697
420	315	409	575
800	213	282	381

To further investigate the cycling effect on the morphologies of the electrode, FESEM was carried out after cycling performance. Fig. 3.11(a-f) shows the FESEM images of SnSe, SnSe/C and SnSe/MWCNT after 100 cycles. It can be seen from the Fig. 3.11(a-b), there are major cracks appearing in the SnSe electrode and SnSe particles have been completely destroyed after 100 cycles. For SnSe/C electrode after 100 cycles, there are minor cracks appeared on the SnSe/C electrode as compared to bare SnSe electrode and particle morphology have not changed much, whereas SnSe/MWCNT electrode shows no cracking and remains integral, though the presence of MWCNT is not visible in the image but there is a presence of a very thin gel like layer on the SnSe/MWCNT electrode after cycling which could be related to the increased capacity[139].

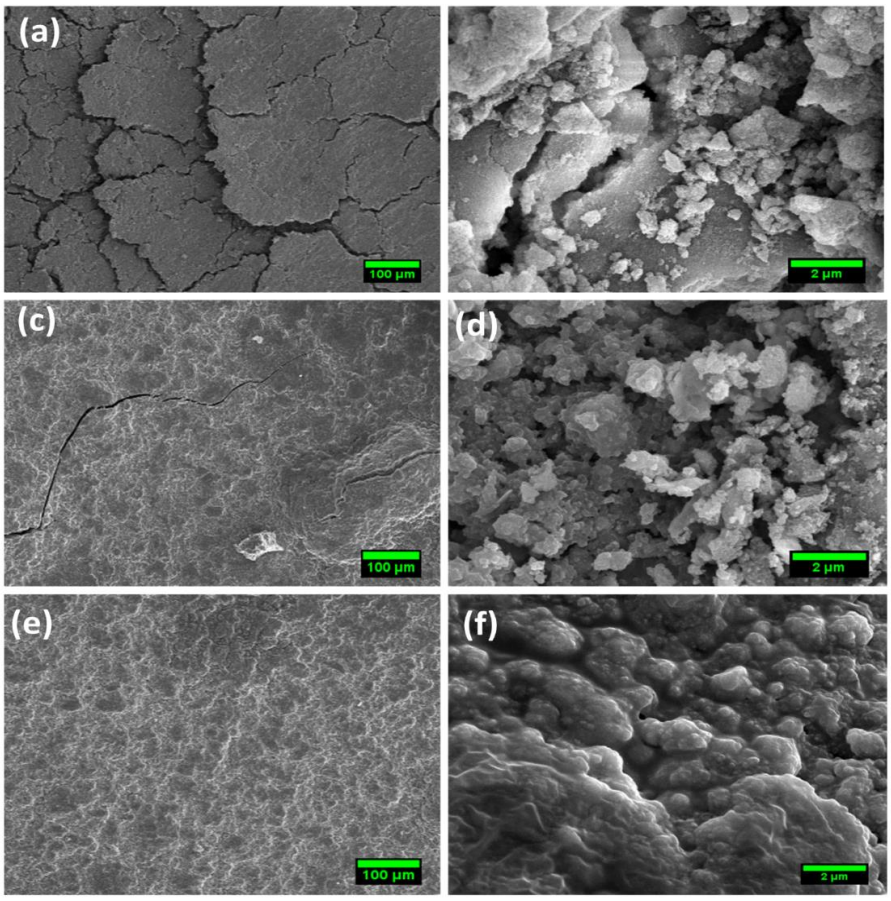

Figure 3.11 FESEM micrographs of (a-b) SnSe, (c-d) SnSe/C, (e-f) SnSe/MWCNT after 100 cycles.

3.2.2.5 Galvanostatic Intermittent Titration Technique (GITT) Analysis

Another method, Galvanostatic Intermittent Titration Technique (GITT) has been studied to understand Li-ion insertion and extraction kinetics of electrodes and hence used to determine Li-ion diffusion coefficient using GITT analysis[140]. Figure 3.12 (a-c) shows GITT curves of SnSe, SnSe/C and SnSe/MWCNT between 0.01 and 2.5 V. For titration process, initially the cells were first discharged for 10 minutes at a current density of 40 mAg^{-1} and then kept on rest for 30 minutes. The obtained GITT curves shows plateaus which is in accordance with obtained CV curves for the same electrode. The Li-ion diffusion coefficient has been calculated using the given equation which is based on Fick's second law[141];

$$D_{Li^+} = \frac{4}{\pi}\left(\frac{m_B V_M}{M_B A}\right)^2 \left(\frac{\Delta E_S}{\tau(\frac{dE_\tau}{d\sqrt{\tau}})}\right)^2 \left(\tau \ll \frac{L^2}{D_{Li^+}}\right) \quad (3.13)$$

Where τ, L, A, m_B, V_M and M_B is the duration in which electrode stays at rest, thickness of the electrode, surface area of the electrode, mass, volume and molecular weight of the active material, respectively. When the change in cell potential exhibit a linear relationship when plotted against square root of duration time (τ) as shown in Fig. 3.12(d-f), then equation (34) can be re-written as:

$$D_{Li^+} = \frac{4}{\pi\tau}\left(\frac{m_B V_M}{M_B A}\right)^2 \left(\frac{\Delta E_S}{\Delta E_\tau}\right)^2 \left(\tau \ll \frac{L^2}{D_{Li^+}}\right) \quad (3.14)$$

Where, ΔE_S represents the steady-state voltage change during the current pulse, after eliminating the iR drop occurring from the electrical internal resistance and ΔE_τ is the change in potential for the charge/discharge during the constant current pulse, and can be directly acquired from GITT curves[135,142].

The Li-ion diffusion coefficients are calculated from the GITT curve at all steps for discharging except for 1st discharge due to large variation and plot of log (D_{Li^+}) as a function of Voltage (V) as shown in Fig. 3.12 (g-i). As can be seen from Fig. 3.12(g-i), the three electrodes showed three minimum Li-ion diffusion coefficient points at voltage shown in graph. These obtained minimums are due to a phase transition from strong attractive interaction between the host matrix and the intercalation species. On Comparing with the cyclic voltammetry results, these potentials are the redox potentials. The lithium-ion diffusion coefficient from these three points for SnSe, SnSe/C and SnSe/MWCNT are summarized in Table 3.6. The obtained lithium diffusion coefficient may not be completely accurate considering the calculation error in dE/dx and deviation in parameter V_M. Therefore, the calculated D_{Li^+} values showed slight variation when compared to the results obtained from EIS and CV.

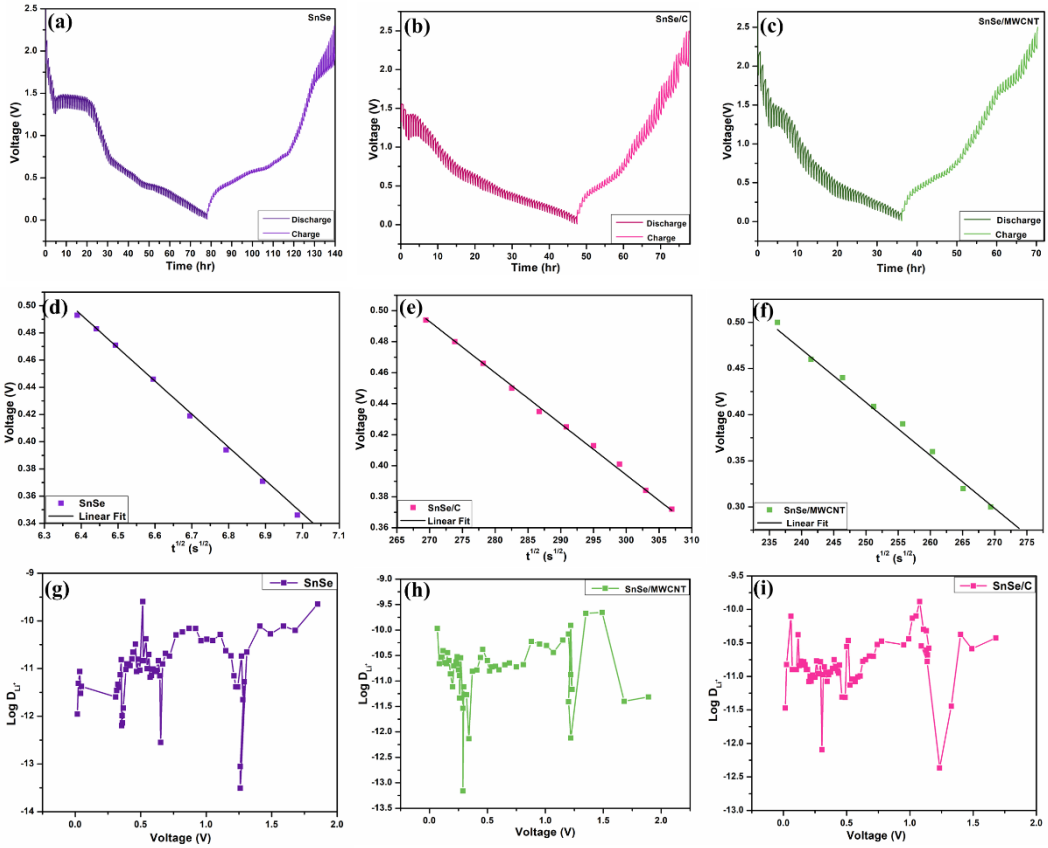

Figure 3.12 Discharge/charge GITT curve of (a)SnSe (b) SnSe/C and (c) SnSe/MWCNT, the plot of V vs $\tau^{0.5}$ for (d) SnSe (e) SnSe/C and (f) SnSe/MWCNT, lithium diffusion coefficient as a function of voltage for (g) SnSe (h) SnSe/C and (i) SnSe/MWCNT.

Table 3.6 Calculated D_{Li+} values of (a) SnSe (b) SnSe/C (c) SnSe/MWCNT from GITT measurements.

Potential (V)	D_{Li^+} $(cm^2 s^{-1})$		
	SnSe	**SnSe/C**	**SnSe/MWCNT**
1.68	---	---	3.98×10^{-12}
1.2-1.3	3.12×10^{-14}	4.73×10^{-13}	7.57×10^{-13}
0.652	2.82×10^{-13}	---	---
0.3-0.5	7.3×10^{-14}	3.44×10^{-13}	7.33×10^{-13}
0.28	---	---	2.9×10^{-12}

Hence, in this section, structural, morphological and electrochemical studies of SnSe and its composite with Super P and MWCNT have been studied. The X-ray diffraction (XRD) of the synthesized materials has been observed as an orthorhombic structure with space group, pnma without any impurities. The morphological studies have displayed irregularly shaped micro-sized particles of SnSe with the average particle size of 0.65 μm. SnSe/C and SnSe/MWCNT composite SEM shows that the super P and MWCNT are well anchored with the SnSe particles. Among all three anode materials, SnSe/MWCNT showed higher values of Li^+ diffusion coefficient, indicating that the SnSe/MWCNT electrode has superior kinetics over SnSe/C and SnSe.

Chapter 4 : Electrochemical Studies of Mn-Zn ferrite as alternative anode material

In this chapter, structural, morphological, and electrochemical studies of Mn-Zn ferrite-based spinel structural material $Zn_{1-x}Mn_xFe_2O_4$ (x = 0.0, 0.01, 0.03, 0.05) has been investigated as alternative anode using a simple and facile solid-state ball-milling route

4.1 Introduction

Transition metal oxides (TMOs) have been rigorously studied for a few years now owing to their high theoretical capacity (600-1200 $mAhg^{-1}$) and still haven't been used for commercial batteries due to their limitation of capacity damping upon cycling and poor conductivity. So, there is a lot more to explore in the field of TMOs as anode materials for LIBs[31,143]. Recently, among the Transition metal oxides (TMOs), Fe-based anodes have been studied and reported materials with high energy density, environmental benignity, and easier availability. Fe_2O_3 is one of the iron-based TMO anode materials that has gained much attention in the last few years due to its high theoretical capacity of ~1000 $mAhg^{-1}$[144]. Lately, MFe_2O_4 (M=Zn, Mg, Ni, etc) type TMOs have been rigorously studied owing to their high theoretical reversible capacities. Spinel ferrites (MFe_2O_4) as an anode material have proven themselves to be potential ordinates, when it comes to delivering high energy density[145,146].

Among all spinel ferrites, $ZnFe_2O_4$ stands out the most owing to its low price, low toxicity, abundance, short lithium-ion diffusion path, high surface-to-volume ratio, environment benignity, and pre-eminently it possesses high theoretical capacity (`1072 $mAhg^{-1}$). However, despite having these excellent properties, the practical application of $ZnFe_2O_4$ is still unattainable because of the fast capacity fading during the discharge-charge process, low electronic conductivity, and high working voltage[147]. Doping with other transition metals is one of the effective ways to overcome these obstacles. Doping with transition metal ions provides the potential benefit of enabling additional redox reactions within the same potential range as Zn and Fe ions[148–151].

In this chapter, synthesis of $Zn_{1-x}Mn_xFe_2O_4$ (x= 0.0, 0.01, 0.03, 0.05) has been attempted via a simple and cost-effective ball milling route. The physical and electrochemical properties have been investigated. Since, the primary benefits of the ball milling method is its capability for large-scale production. Herein, Manganese (Mn) stands out as the preferred dopant among a

range of transition metals, primarily due to its abundance, cost-effectiveness, and minimal environmental impact. Furthermore, Mn-doped anodes demonstrate a notably consistent voltage profile throughout the lithiation and de-lithiation processes, contributing to stable battery performance.

Synthesis of $Zn_{1-x}Mn_xFe_2O_4$ (x= 0.0, 0.01, 0.03, 0.05) has been carried out using solid state route as mentioned in Chapter 2 section and the synthesized samples are abbreviated as ZF0, ZF1, ZF2 and ZF3 corresponding to x= 0.0, 0.01, 0.03 and 0.05, respectively. Physicochemical characterization and electrochemical performance of $Zn_{1-x}Mn_xFe_2O_4$ (x= 0.0, 0.01, 0.03, 0.05) have been investigated as mentioned in experimental details in Chapter 2 section.

4.2 Results and discussion

4.2.1 Structural and Morphological Characterization

4.2.1.1 X-ray Diffraction (XRD) Analysis

Figure 4.1(a-b) demonstrates the XRD patterns of $Zn_{1-x}Mn_xFe_2O_4$ (x = 0.0, 0.01, 0.03, 0.05) obtained after the calcination process at 800 ^oC for 4 hours. The observed peaks in the XRD pattern of the prepared ZF0, ZF1, ZF2, and ZF3 samples (Fig.4.1(a)) match well with the standard pattern of cubic spinel structure (JCPDS card no. 01-79-1150). The XRD peaks at angle (2θ) positions 18.17^o, 29.90^o, 35.36^o, 36.84^o, 42.811^o, 53.10^o, 56.5^o, and 62.35^o can be assigned the (111), (220), (311), (222), (400), (422), (511), and (440) planes of the cubic spinel structure, respectively.

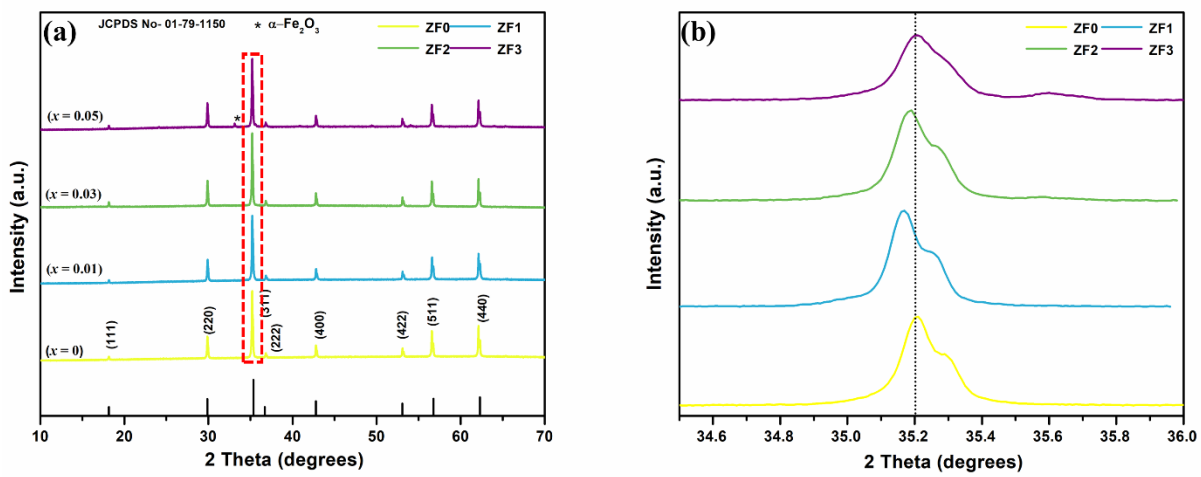

Figure 4.1 wide range XRD patterns of (a) $Zn_{1-x}Mn_xFe_2O_4$ (x = 0.0, 0.01, 0.03, 0.05), (b) narrow range magnified peak (311) of $Zn_{1-x}Mn_xFe_2O_4$ (x = 0.0, 0.01, 0.03, 0.05).

The enlarged narrow range diffraction peak corresponds to the (311) plane as shown in Fig. 4.1 (b), it indicates the substitution of Mn^{2+} at the Zn^{2+} site. As can be seen from Fig.4.1 (b), there is a slight shift in the position of the peak towards the lower angle (2θ) for x = 0.0 to 0.03 and when x increases to x = 0.05 there is a sudden shift towards higher angle(2θ) values. This shift in the 2θ values could be ascribed to the variation in the value of ionic radii of Mn^{2+} (83pm) and Zn^{2+} (74pm). Since the ionic radii of Mn^{2+} are greater than Zn^{2+}, it is anticipated that the XRD peak might move towards the lower angle (2θ) values[152–154]. Moreover, a peak splitting is observed in the (311), (422), (511), and (440) peaks, which could be due to the strain produced in the synthesized samples due to the site occupancy of Mn ions[155]. Moreover, for x = 0.05 there is a presence of an extra impurity peak of α-Fe_2O_3 (marked as *), the presence of this impurity peak has been interpreted due to the heating of the ferrites in an oxygen-rich environment which could generate this hematite phase. A similar presence of the hematite phase in Mn-doped zinc ferrite has been reported by Abdel Maksoud et al.[156]. Rohit et al. have also reported the formation of α-Fe_2O_3 for Mn-doped Mg-Zn ferrite[157]. The crystallite

size for the prepared samples was estimated by the Scherrer formula (36) using the most intense peak (311);

$$D = 0.9\lambda/\beta\cos\theta \quad (4.1)$$

Where D, λ, β, and θ are crystallite size, X-ray diffraction wavelength (Cu-$k_{\alpha 1}$ radiation) 0.154 nm, FWHM of (311) peak, and Bragg's diffraction angle, respectively. The lattice parameter "a" was calculated using the following relation (37);

$$a = d_{hkl}\sqrt{h^2 + k^2 + l^2} \quad (4.2)$$

Where 'a' and 'd_{hkl}' represents lattice parameter, d-spacing, respectively and h, k, and l represents Miller indices. The value of lattice parameter "a" for Mn-doped $ZnFe_2O_4$ is higher than the bare $ZnFe_2O_4$. This could be attributed to the substitution of Zn^{2+} (74pm) with Mn^{2+} (83pm). An increase in the lattice parameter may lead to the shift towards lower diffraction angles in the XRD peaks, whereas a decrease in lattice parameter would result in shift towards higher diffraction angles. It can be seen from Fig. 4.1 (b), for x = 0.01 there is a slight shift towards lower 'θ' values and shows higher value of lattice constant (a = 8.447 Å), and for x = 0.03 the peak is shifted slightly towards higher '2θ' value and indicate a decrement in lattice constant (a=8.445 Å). For x = 0.05, the peak is shifted slightly more towards higher diffraction angle and shows increment in lattice parameter value (a = 8.451Å). This shift in diffraction peak and variation in lattice parameter within Mn-doped $ZnFe_2O_4$ samples could be due to the site occupancy of Mn ions. Moreover, the broadening of the XRD peak may ascribed to the generation of intrinsic microstrain, which arises from the changes in the lattice parameter induced by crystal imperfections and dislocations. Hence, microstrain (ε) for the prepared samples has been estimated using the Hall-Williamson method as given[158]:

$$\beta\cos\theta = 4\varepsilon\sin\theta + \frac{0.9\lambda}{D} \quad (4.3)$$

Figure 4.2 (a) shows the Hall-Williamson plots for ZF0, ZF1, ZF2 and ZF3 samples. The slope between $4sin\theta$ and $\beta cos\theta$ gives the value of microstrain (ε). The variation of Mn doping (x = 0, 0.01, 0.03, 0.05) with lattice parameter and average crystallite size are also shown in Fig. 4.2(b). The estimated values of crystallite size (D), lattice parameter(a), and microstrain (ε) from the XRD analysis are summarized in Table 4.1. Hence, it can be seen from the obtained values that the introduction of Mn in the $ZnFe_2O_4$ has resulted in increment of lattice parameter and decrement in microstrain (ε) as compared to bare $ZnFe_2O_4$. Among all the doped samples, ZF2 shows lowest value of lattice parameter and crystallite size, and highest value of microstrain. Microstrain induced lattice distortions and defects may create more active sites for insertion and extraction of Li-ions which could potentially increase the charge storage capacity. Moreover, smaller crystallite size and lattice constant of ZF2 could result in a higher surface area, increased number of electrochemical active sites and shorter distance between crystal planes, facilitating faster ion diffusion within the electrode material.

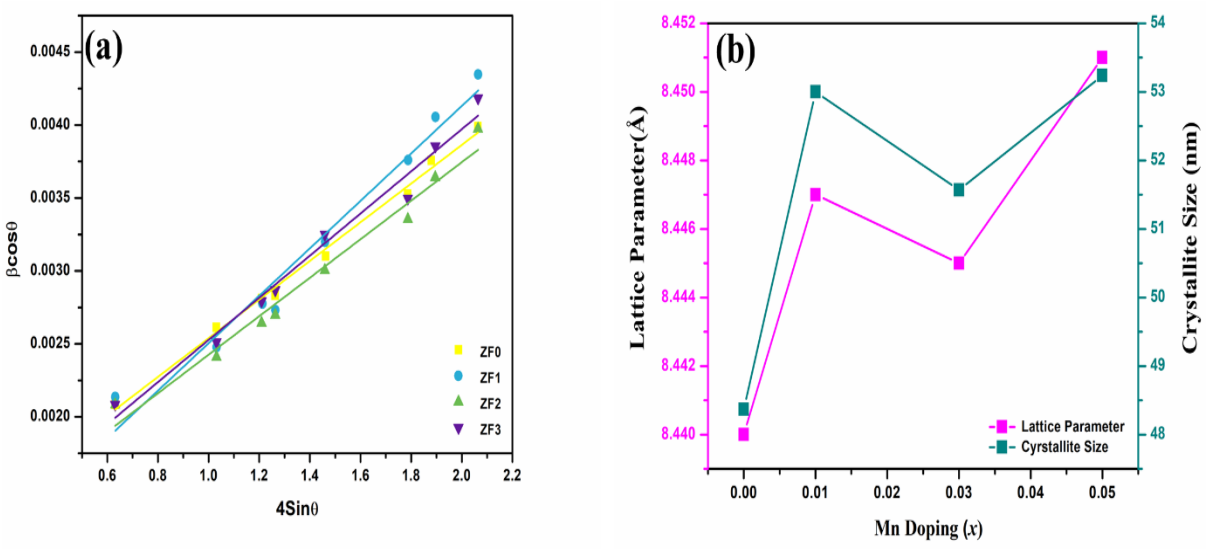

Figure 4.2 (a) Variation of lattice parameter 'a' and crystallite size 'D' as a function of Mn doping (x), (b) Hall-Williamson plot of $Zn_{1-x}Mn_xFe_2O_4$ (x = 0.0, 0.01, 0.03, 0.05).

Table 4.1 Lattice Parameter and Crystallite size of samples ZF0, ZF1, ZF2, and ZF3.

Sample	Lattice Parameter (Å)	Crystallite size (nm)	Microstrain (ε) ($x10^{-3}$)
ZF0	8.44	48.37	1.21
ZF1	8.447	53	0.97
ZF2	8.445	51.57	1.11
ZF3	8.451	53.24	1.08

4.2.1.2 Scanning Electron Microscopy (SEM) and Energy Dispersive X-ray Spectroscopy (EDX) Analysis

The SEM micrographs of ZF0, ZF1, ZF2, and ZF3 samples are displayed in Fig. 4.3 (a-d). It can be observed from the SEM micrographs that all sample shows polyhedron-shaped agglomerated particles. The average particle size is found nearly to be 0.2 μm as estimated from ImageJ software for ZF0 sample. It is observed that with an increase in Mn doping, there is a reduction of ~ 80-100 nm in the size of the particles. The average particle size of Mn doped samples ZF1, ZF2, and ZF3 has been found as found to be 0.12 μm, 0.10 μm and 0.11 μm, respectively as observed from SEM micrographs (Fig.4.3(a-d)).

Moreover, the introduction of Mn is observed to mitigate agglomeration among $ZnFe_2O_4$ particles. The particle uniformity improves with the rise in Mn concentration within $ZnFe_2O_4$, progressing from x=0.01 to x=0.05. Particle agglomeration in ferrites is commonly attributed to the magnetic dipole-dipole interactions between them. This agglomeration observed among ferrites particles, has also been documented by other researchers. P. Falak et al.[159] and M. Ansari et al.[160] have similarly reported the agglomeration of $ZnFe_2O_4$ particles due to magnetic interaction between them. Additionally, particles often agglomerate in an effort to reduce their surface energy[161]. Among all the Mn concentrations, the ZF2 sample shows the smallest particle size (0.10 μm) and least agglomeration. The reduced agglomeration and the

sub-micron sized polyhedron particles may significantly impact the electrochemical performance of the electrode material. Smaller particle size and minimized agglomeration of ZF2 could lead to increased surface area, improved electrode-electrolyte contact, and ultimately, better electrochemical performance due to more efficient charge transfer processes and kinetics.

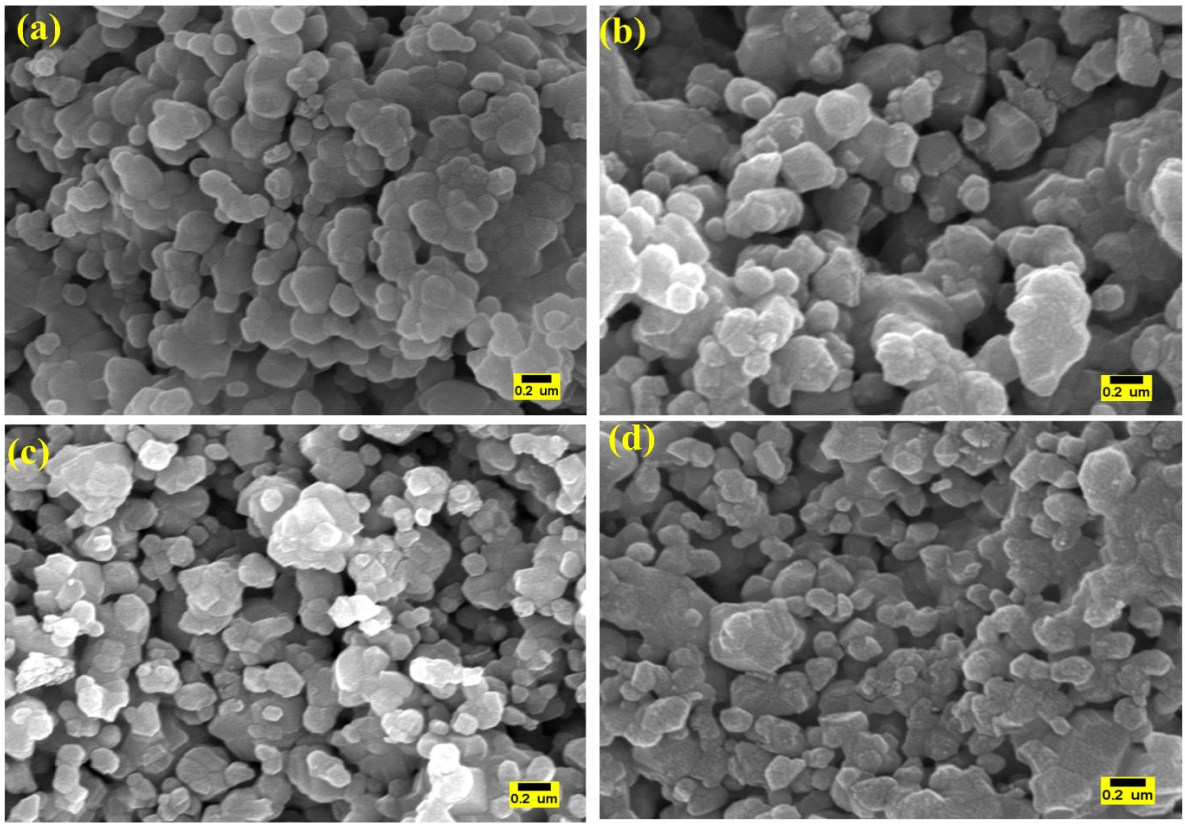

Figure 4.3 SEM micrographs of samples: (a) ZF0 (b) ZF1 (c) ZF2 (d) ZF3 synthesized at 800 ºC for 4 hours using ball milling route.

Furthermore, to confirm the formation of $Zn_{1-x}Mn_xFe_2O_4$ (x = 0.0, 0.01, 0.03, 0.05), elemental mapping has been carried out for ZF0, ZF1, ZF2, and ZF3 samples as shown in Fig. 4.4 (a-d), which confirms that the elemental distribution of Zn, Fe, O, and Mn is almost homogeneous

throughout the sample. Figure 4.5 (a-d) indicates the quantitative analysis for each sample and the spectrum of sample ZF0, ZF1, ZF2 and ZF3. Figure 4.5 (a) shows the peaks of Zn, Fe, and O for ZF0, and Fig. 4.5 (c-d) shows the peaks of Zn, Mn, Fe, and O elements for Mn doped ZF1, ZF2, and ZF3 samples. As can be seen from the graphs, no impurity peak is detected in the prepared sample which confirms the pure form of the synthesized materials.

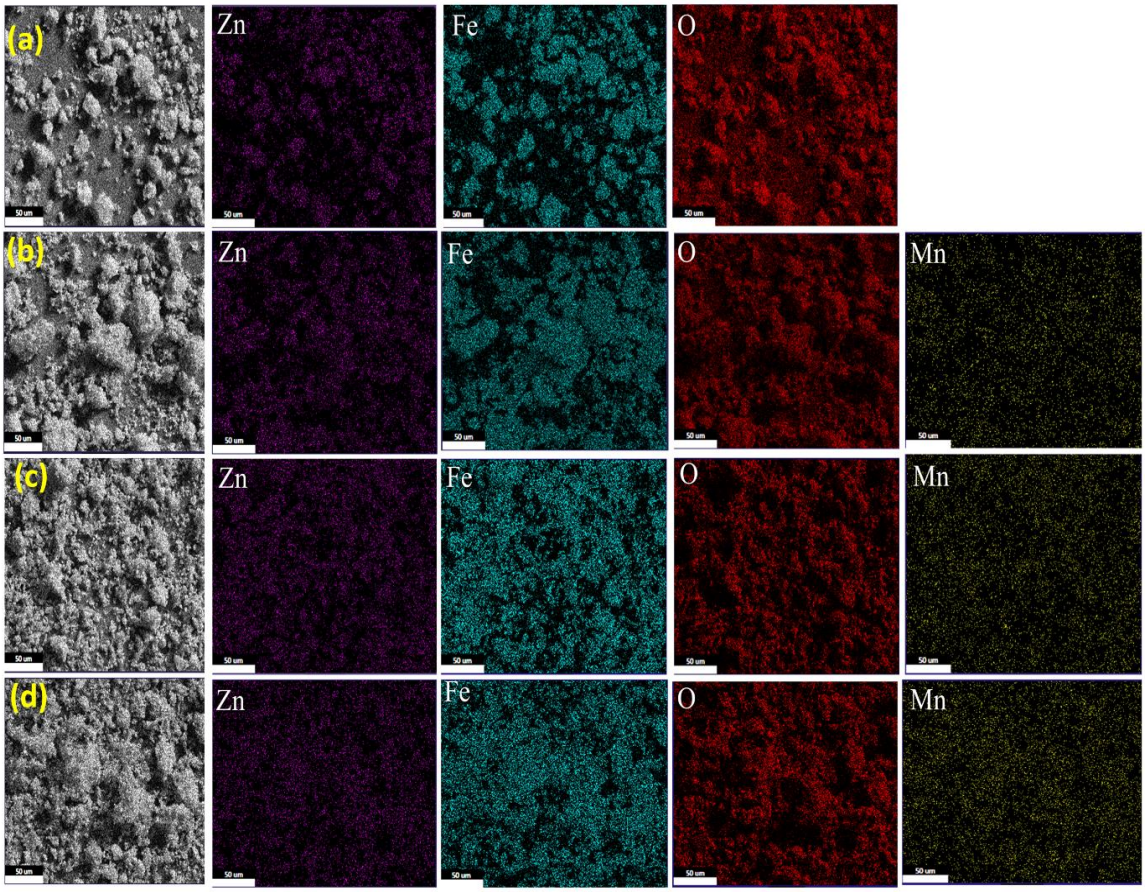

Figure 4.4 Elemental mapping images of Zn (Purple), Fe (Blue), O(Red) and Mn (Yellow) of (a) ZF0, (b) ZF1 (c)ZF2 (d) ZF3 samples.

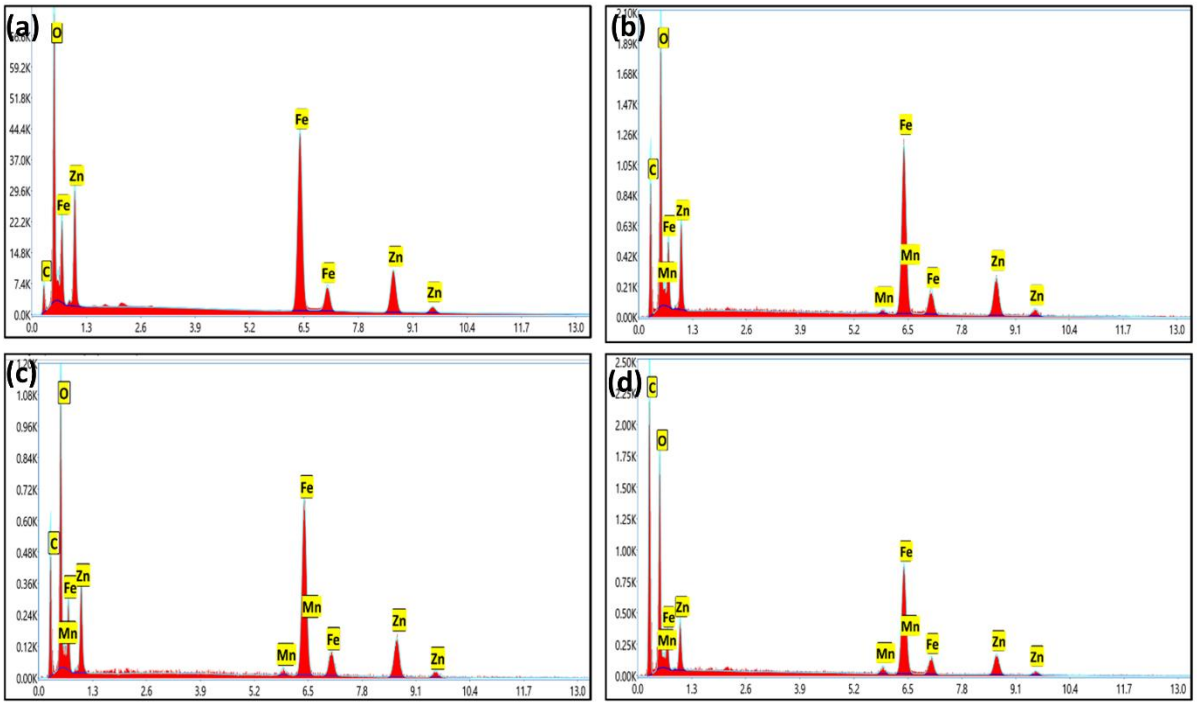

Figure 4.5 EDS analysis spectrum of (a) ZF0 (b) ZF1 (c)ZF2 (d) ZF3 samples.

4.2.1.3 Transmission Electron Microscopy (TEM) Analysis

Figure 4.6 (a-l) displays the HRTEM images and selected area electron diffraction (SAED) patterns of bare sample ZF0 and Mn doped ZF1, ZF2 and ZF3. It can be seen from the TEM micrographs all samples show polyhedron-type morphology as can be seen in Fig. 4.6(a,d,g,j). However, Mn-doped samples show less agglomeration as compared to bare $ZnFe_2O_4$ (ZFO). The average particle size as measured from ImageJ software and it is estimated as ~ 0.1 μm. Among all the prepared samples, Mn doped ZF2 sample shows the most uniform polyhedron-shaped particles with the average smallest particle size. Figure 4.6 (b,e,h,k) depicts the enlarged images of the diffraction fringes pattern of ZF0,ZF1,ZF2, and ZF3 samples showing clear lattice fringes with a lattice spacing of 0.481 nm, 0.483 nm, 0.482 nm and 0.484 nm, respectively, corresponding to (111) plane of XRD pattern, which further confirms the crystalline nature of the sample. Figure 4.6 (c,f,i,l) illustrates the SAED patterns, revealing

diffused rings with small spots resulting from the Bragg's reflection originating from individual crystallites, and the crystalline nature of the samples.

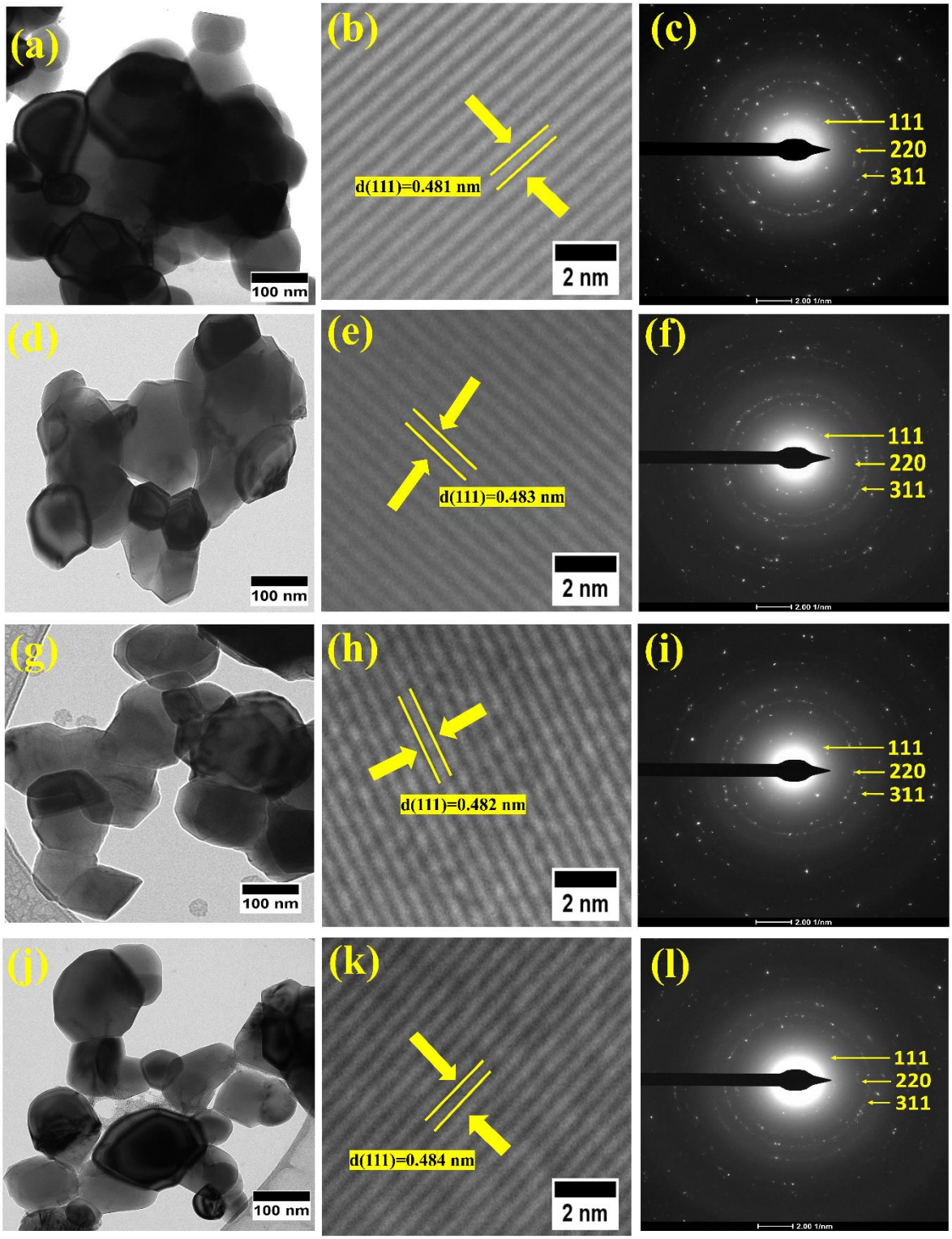

Figure 4.6 HRTEM and SAED images of (a-c) ZF0 (d-f) ZF1(g-i) ZF2 (j-l) ZF3 synthesized at 800 ^{0}C for 4 hours using ball milling route.

4.2.2 Functional Group analysis

4.2.2.1 Fourier Transform Infrared Spectroscopy (FTIR)

The FTIR spectra of ZF0, ZF1, ZF2 and ZF3 samples are shown in Fig. 4.7 these spectra are observed in wide scan range of 400-4000 cm^{-1} in ATR mode. The spectra revealed only the vibration from metal-oxygen stretching in the range of 500-580 cm^{-1} and a small absorption band is noticed at ~ 685 cm^{-1} which could occur due to the cationic interchange between the two sites (octahedral and tetrahedral), which is often observed in Zinc ferrites[162,163].

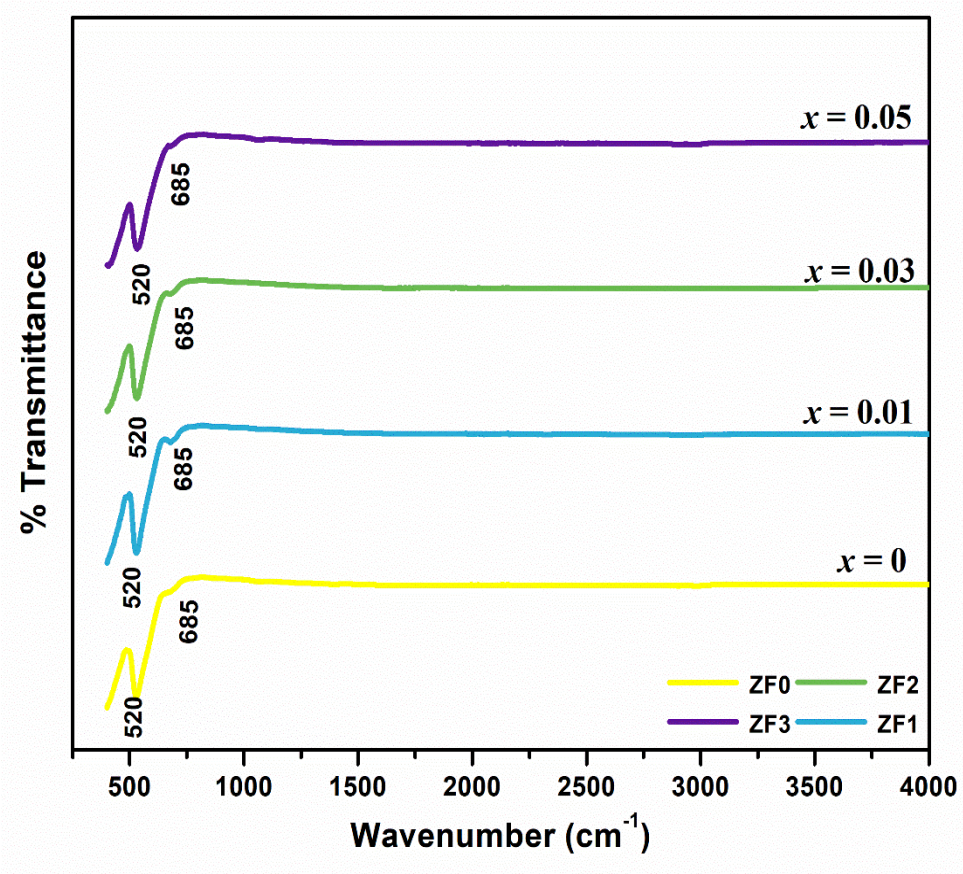

Figure 4.7 FTIR analysis of ZF0, ZF1, ZF2 and ZF3 samples in the range 400-4000 cm^{-1}.

4.2.3 Electrical Measurements

The DC conductivity variation with temperature has been studied for the prepared ZF0, ZF1, ZF2 and ZF3 samples. Figure 4.8 (a) represents the Arrhenius plot for ZF0, ZF1, ZF2, and ZF3 samples in which $ln(\sigma_{DC})$ is plotted against 1000/T. The activation energy (E_a) has been calculated using the slope of the Arrhenius plot. The functional form of the Arrhenius equation can be expressed as[164];

$$\sigma_{DC} = \sigma_0 \, exp \, exp \, \frac{-E_a}{K_B T} \tag{4.4}$$

Where, K_B = Boltzmann's constant (JK^{-1}), σ_{DC} = D.C. conductivity (S/cm), T= Temperature (K), and E_a = Activation energy (eV).

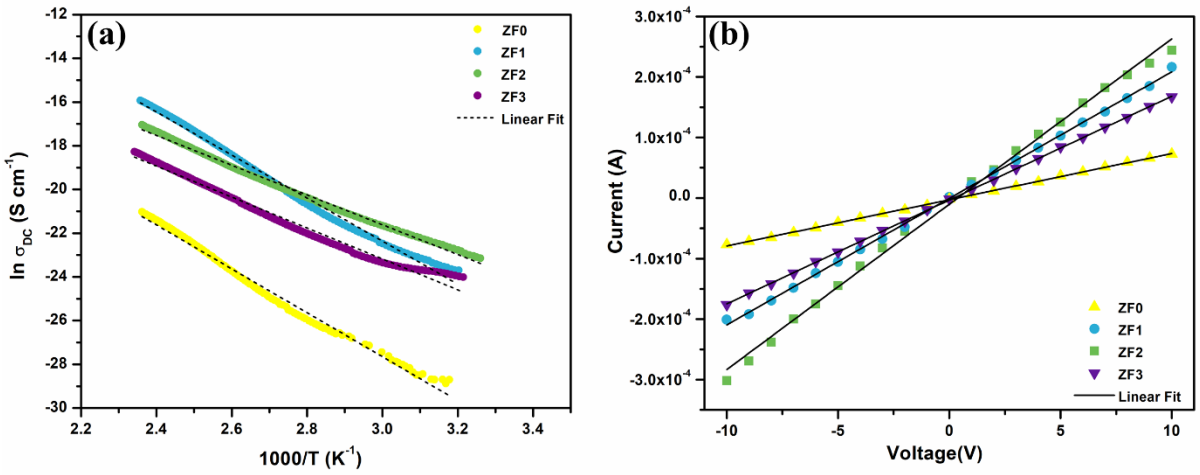

Figure 4.8 (a) Variation of DC conductivity with temperature for ZF0, ZF1, ZF2, and ZF3 (b) I-V curve for ZF0, ZF1, ZF2 and ZF3 at room temperature.

The D.C conductivity (σ_{DC}) was obtained using the following relation:

$$\sigma_{DC} = \frac{l}{R\,A} \tag{4.5}$$

Where σ_{DC}, l, R, and A denote electrical conductivity (S/cm), the thickness of the pellet (cm), DC resistance (Ω), and the pellet area (cm^2), respectively.

Figure 4.8 (b) illustrates the I-V curve for ZF0, ZF1, ZF2, and ZF3 samples at room temperature. The observed values of activation energy (E_a), D.C conductivity (σ_{DC}) ,and DC Resistance (R) are summarized in Table 4.2. It is noticed that as the Mn concentration increases as dopant, the activation energy decreases[165]. Moreover, ZF2 sample shows the lowest values of E_a and R, and the highest value of DC conductivity (σ_{DC}), implying that the ZF2 electrode could be advantageous for enhancing the electrochemical properties.

Table 4.2 Estimated DC Conductivity resistance and activation energy for ZF0, ZF1, ZF2 and ZF3 samples.

Sample	**DC Resistance (R), Ω**	**Activation Energy, E_a eV**	**D.C electrical conductivity, σ_{DC} S/cm**
ZF0	131	0.867	1.35 X 10^{-6}
ZF1	58.3	0.820	3.03 X 10^{-6}
ZF2	36.6	0.5702	4.83 X 10^{-6}
ZF3	47.8	0.6490	3.7 X 10^{-6}

4.2.4 Electrochemical Characterization

4.2.4.1 Electrochemical Impedance Spectroscopy (EIS) Analysis

EIS has been performed to understand the effect of Mn doping on the $ZnFe_2O_4$ electrode impedance. Nyquist plots of prepared samples of ZF0, ZF1, ZF2 and ZF3 observed with fresh cell electrodes at OCV within frequency window of 10 mHz to 100 kHz are illustrated in Fig. 4.9 (a). The Nyquist plot was fitted using EIS analyser software. The fitted equivalent circuit consists of different components such as R_s, R_{ct}, CPE, and Z_w as shown in Fig. 4.9 (b). As depicted in Fig. 4.9 (a), all the Nyquist plot contains a semicircle in high frequency region. Generally, ohmic resistance (R_s) is represented by the intercept at the x-axis. In the high-frequency range, the semicircle represents interfacial resistance occurring at electrode and electrolyte representing the charge transfer impedance (R_{ct}), and CPE represents the double-

layer capacitance which corresponds to the SEI layer generation at the electrode/electrolyte interface. In the low-frequency range, the inclined line denotes the Warburg impedance (Z_w) arising from the diffusion of Li-ions[166]. The parameters obtained from the fitting of the equivalent circuit are recorded in Table 4.3. To calculate the lithium-ion diffusion coefficient for the bulk electrode equation (3.11) has been used as mentioned in chapter 3 section 3.2.2.3

As shown in Fig. 4.9 (c), the Warburg coefficient for different Mn doping is calculated using the slope of Z' vs $\omega^{-0.5}$. The observed values of Li-ion diffusion coefficient are tabulated in Table 4.3. Here, it can be seen that the D_{Li^+} value for ZF2 is the highest among all the other electrodes. Also, the diameter of the semicircle is smallest for ZF2 giving the lowest R_{ct} values among all the other samples implying that the ZF2 electrode has excellent kinetics over other samples which could be due to the more regular polyhedron-shaped morphology and smaller particle size as compared to ZF0, ZF1, and ZF3[167].

Table 4.3 Electrodes kinetic parameter obtained from equivalent circuit fitting for EIS analysis.

	R_s (Ω)	**R_{ct} (Ω)**	**D_{Li^+} (cm^2s^{-1})**
ZF0	3.64	237.08	8.93 X 10^{-18}
ZF1	1.31	211.2	8.60 X 10^{-18}
ZF2	2.79	101.35	4.5 X 10^{-17}
ZF3	2.31	167.91	1.02 X 10^{-17}

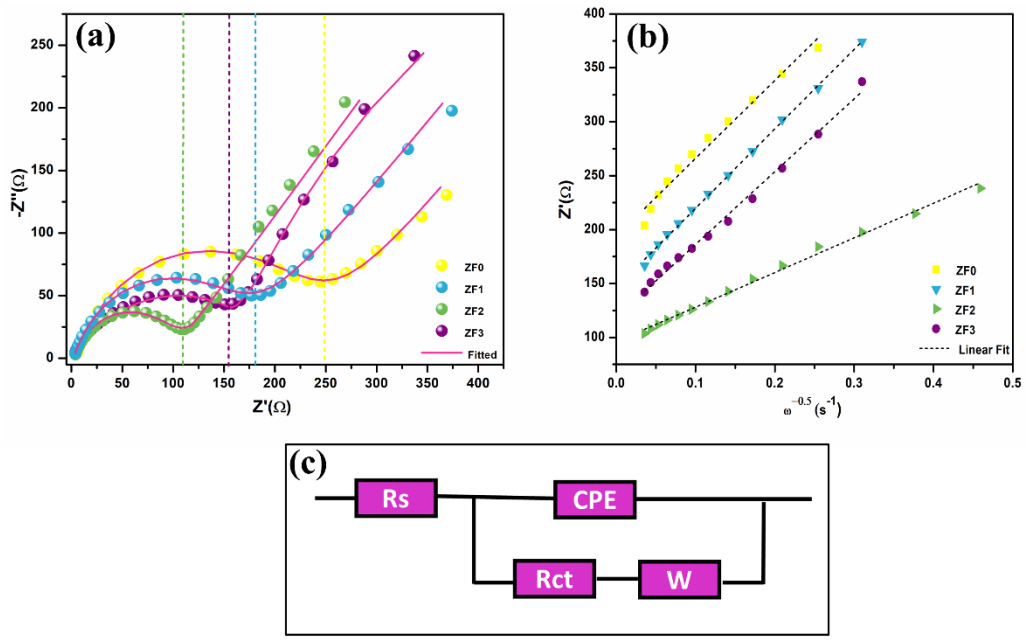

Figure 4.9 (a) Nyquist Plot of ZF0, ZF1, ZF2 and ZF3 sample electrodes, (b) Variation of Z' vs $\omega^{-0.5}$, (c) Fitted equivalent circuit model for EIS analysis.

4.2.4.2 Cyclic Voltammetry (CV) Analysis

Figure 4.10 compares the cyclic voltammograms of ZF0, ZF1, ZF2 and ZF3 samples electrodes at 0.05 mV/s scan rate (0.01-3.00 V). It can be observed from these CV curves that during lithiation/de-lithiation, similar redox reactions are taking place and no extra peaks are present. During the first discharge cycle, there is a cathodic peak around 0.50-0.55 V for all electrodes attributing to the reduction of $Zn_{1-x}Mn_xFe_2O_4$ with Li into Zn and Fe while formation of Li-Zn alloy (lithiation of Zn) with an irreversible decomposition of electrolyte forming Solid Electrolyte Interface (SEI). In the 2nd and 3rd discharge cycles, this cathodic peak shifts to 0.8-0.9 V which is reversible, resulting from the reduction of metal oxides. The shift in the potential suggests the possibility of structural rearrangement. During the first charge process, an anodic peak is noticed nearly around 1.58 -1.62 V corresponding to the oxidation of Zn^0, Mn^0, and Fe^0 to ZnO, MnO, and Fe_2O_3. For the 2nd and 3rd cycles, there is not much shift in the oxidation potential. The charge-discharge mechanism can be explained via the following electrochemical reactions:

$$Zn_{1-x}Mn_xFe_2O_4 + 8Li^+ + 8e^- \rightarrow xMn + (1-x)Zn + 2Fe + 4Li_2O \quad (4.6)$$

$$Zn + Li^+ + e^- \rightarrow LiZn \quad (4.7)$$

$$Zn + Li_2O \rightarrow ZnO + 2Li^+ + 2e^- \quad (4.8)$$

$$Mn + Li_2O \rightarrow MnO + 2Li^+ + 2e^- \quad (4.9)$$

$$2Fe + Li_2O \rightarrow Fe_2O_3 + 8Li^+ + 8e^- \quad (4.10)$$

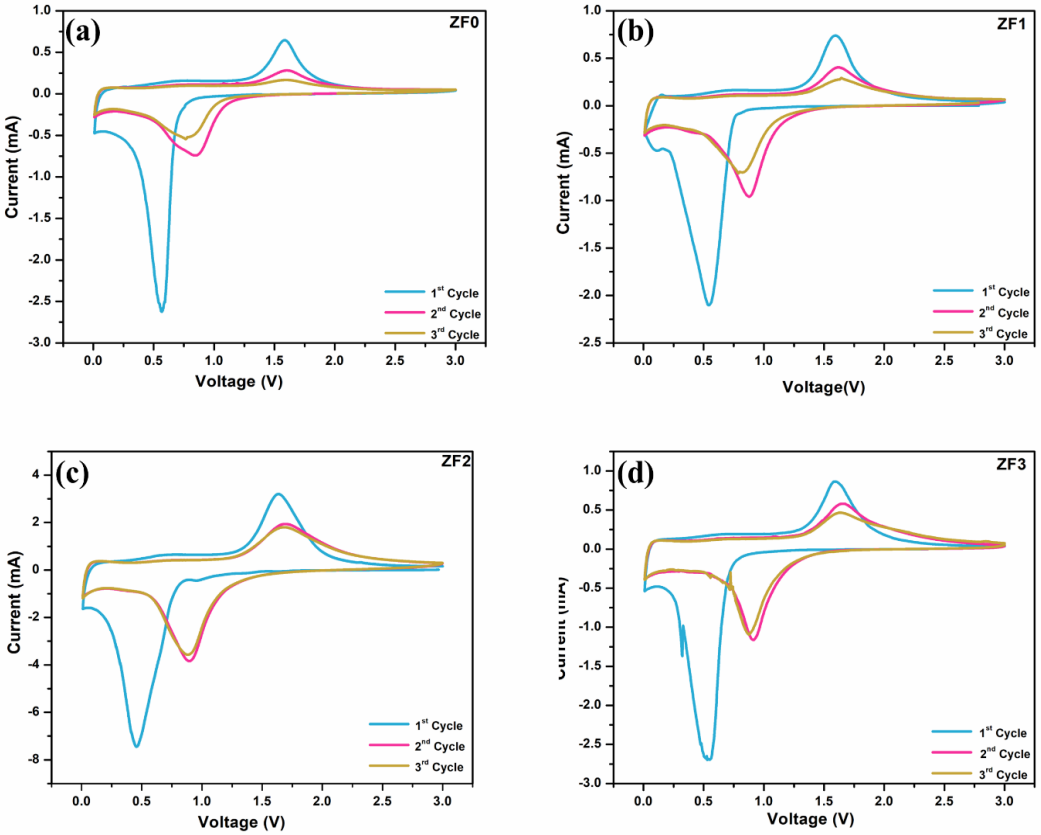

Figure 4.10 Cyclic Voltammograms of (a) ZF0 (b) ZF1 (c) ZF2 (d) ZF3 at a sweep rate of 0.05 mV/s in the voltage range of 0.01-3.0 V.

In sample ZF2, the CV curves of the 2nd and 3rd cycle show maximum coincidence as compared to other electrodes, implying good reversibility. Moreover, the integrated area of the CV profile for subsequent cathodic scans is smaller as compared to the initial cathodic scan suggesting decreasing specific capacity. Whereas, for an anodic scan, the integrated area of the CV is closer to the initial anodic scan, indicating good capacity and reversibility[150,152].

To further investigate the charge storage mechanism in LIBs, with reference to the capacitive and diffusive process, cyclic voltammetry has been performed at various sweep rates (0.1 mV/s, 0.2 mV/s, 0.5mV/s and 1 mV/s) from 0.01 to 3.0 V. It can be seen from Fig. 4.11 (a), that the cathodic peak current and anodic peak current increases with increasing scan rate[168]. The general correlation between peak current (i_p) and scan rate (υ) is demonstrated as;

$$i_p = a\upsilon^b \tag{4.11}$$

$$log\left(i_p\right) = log\, a + b\, log\, (\upsilon) \tag{4.12}$$

Where 'a' and 'b' are variable parameters, the value of 'b' decides the charge storage mechanism, whether it is pseudocapacitive or diffusive. While the 'b' value is nearly 1, the charge storage mechanism is contributed via pseudocapacitive behaviour whereas when the 'b' value is near about 0.5, then the electrochemical process is dominated via diffusive behaviour[169]. Figure 4.11 (a) shows the CV curves for ZF2 sample at various scan rates and Fig. 4.11 (b) shows the relation between log (i_p) and log (υ). The ZF2 electrodes show 'b' values of 0.89 and 0.9 for cathodic and anodic sweep, respectively, indicating that the electrochemical process is dominated via capacitive behaviour.

For the quantitative determination of the pseudocapacitive process $(k_1 v)$ and diffusive process $(k_2 v^{0.5})$ contribution, the following equation can be used:

$$i(V) = k_1 v + k_2 v^{0.5} \tag{4.13}$$

Where v and $i(V)$ represent scan rate and current at a fixed potential, k_1 and k_2 represent potential related coefficients and can be calculated by plotting the $i(V)/v^{0.5}$ vs $v^{0.5}$ curve[167].

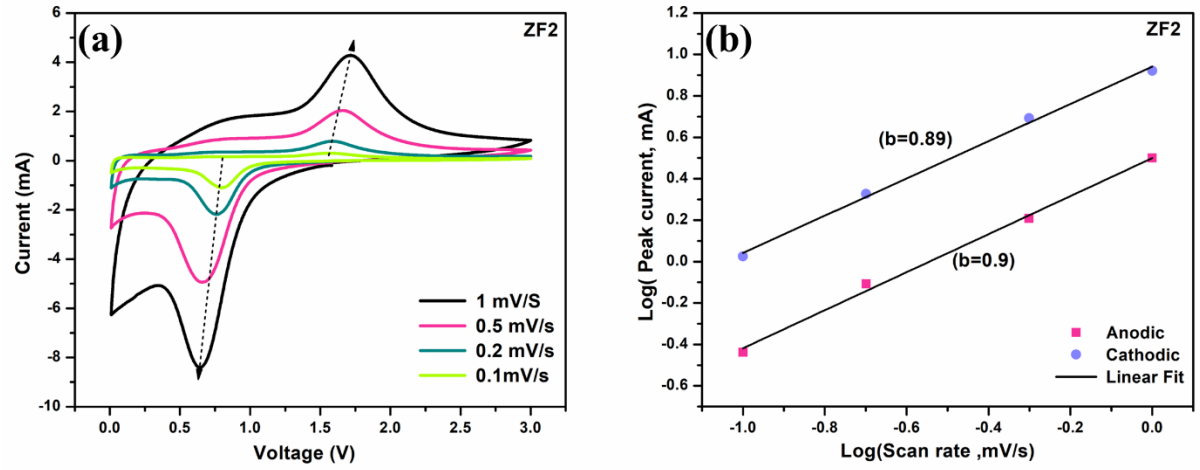

Figure 4.11 (a) CV curves of ZF2 at 0.1 mV/s to 1 mV/s scan rate, (b) relationship between log (i_p) and log (υ) for ZF2.

Figure 4.12 (a-d) shows the calculated capacitive controlled contribution for ZF0, ZF1, ZF2 and ZF3 for a scan rate of 0.5 mV/s. All the prepared electrodes exhibit dominant pseudocapacitive behaviour. Figure 4.12 (e) shows the capacitive and diffusive current for optimised sample ZF2 at various scan rates: 0.1 mV/s, 0.2 mV/s, 0.5 mV/s and 1 mV/s. It has been observed that the capacitive contribution increases as the scan sweep increases. The capacitive contribution to the total capacity for ZF2 is 14%, 28%, 82% and 98 % at scan rates of 0.1 mV/s, 0.2 mV/s, 0.5 mV/s and 1 mV/s. This indicates that capacitive behaviour dominates the charge storage mechanism at higher scan sweeps. The increase in the capacitive process at higher scan rates is attributed to the slow diffusion of Li-ion in active material in comparison to the faster surface capacitive reaction. Since, the surface controlled capacitive process is more stable and faster than the diffusive process. Therefore, the high capacitive contribution plays an important role in delivering excellent cycling stability and rate capability of the prepared electrodes.

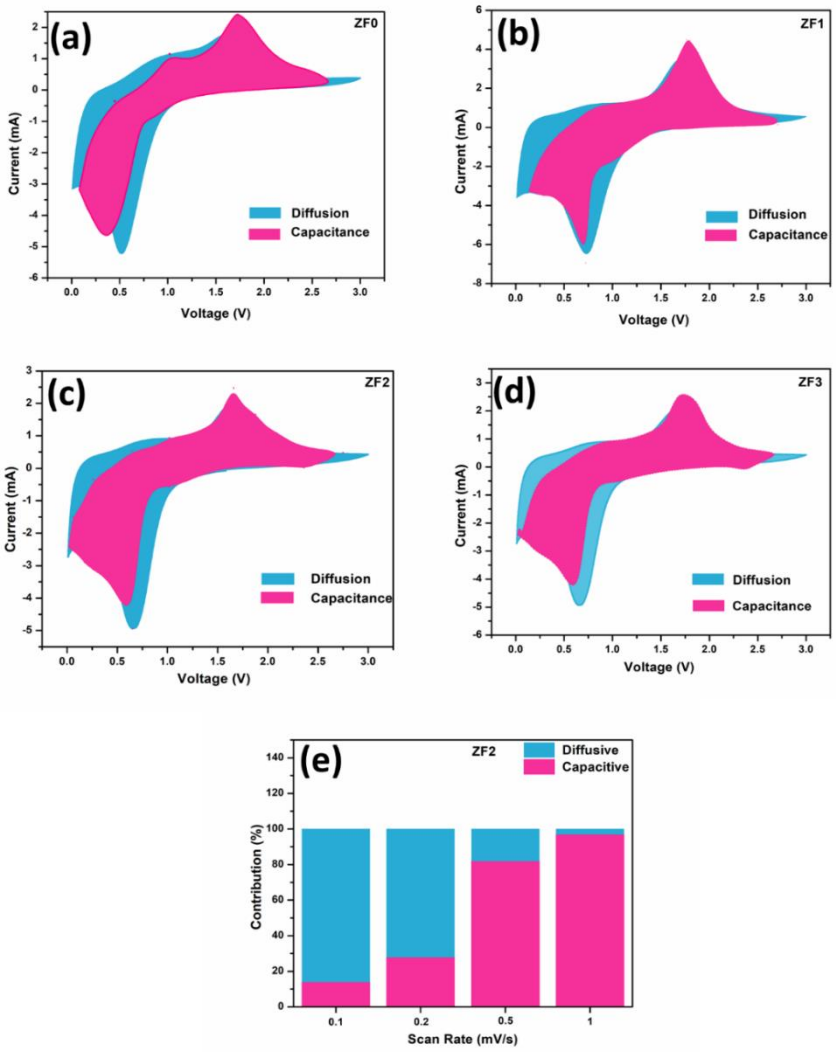

Figure 4.12 The capacitive and diffusive contribution of (a) ZF0 (b) ZF1 (c) ZF2 (d) ZF3 at 0.5 mV/s (e) Capacitive and diffusive contribution of ZF2 at different scan rates.

4.2.4.3 Galvanostatic Charge-Discharge (GCD) Analysis

To further analyze the effect of Mn doping on the electrochemical performance, galvanostatic charge-discharge (GCD) curves are recorded for 1st, 2nd, 5th, 20th and 50th cycles at a current density of 100 mAg^{-1} from 0.01 to 3.0 V as shown in Fig. 4.13. All the samples delivered excellent initial discharge capacity of about 1034 mAhg^{-1}, 1229 mAhg^{-1},1405 mAhg^{-1} and 1220 mAhg^{-1} for ZF0, ZF1, ZF2, and ZF3, respectively. It is clear from the GCD curves that the doping of Mn into zinc ferrite resulted in remarkable enhancement in the initial discharge capacity, and these values are significantly higher than that of bare $ZnFe_2O_4$. It is evident from the GCD curves that ZF2 delivers the best initial discharge and charge capacity of 1405 mAhg^{-}

[1] and 900 $mAhg^{-1}$, respectively, which is equal to 12.6 and 8 mol of Li insertion (coulombic efficiency of 64.2 %). The first irreversible discharge capacity could be due to the disintegration of electrolytes forming the SEI layer and the occurrence of an irreversible Li_2O phase. After the first discharge cycle, ZF2 shows enhanced charge-discharge capacities even after 50 cycles as compared to ZF0. ZF1 and ZF3. The high capacity of ZF2 could be due to the polyhedron-shaped morphology. Moreover, particles with Mn concentration can transform into a new hybrid phase (Fe_2O_3-MnO-ZnO), which could hinder the interfacial resistance and minimize the volume change. Also, the properly amplified lattice constant could play an important role in retarding the capacity loss. A similar phenomenon has been reported for other transition metal oxides[150,152,170].

As depicted in Fig. 4.13 (a-d), the discharge-charge graphs of all the prepared anodes exhibit alike voltage plateaus, indicating the same electrochemical reaction mechanism. During the first discharge cycle of ZF2, the voltage exhibits a sudden fall till the specific capacity is 53 mAh/g forming $Li_{0.47}ZnFe_2O_4$ (0.47 mol of Li^+ insertion), then an obvious longer plateau is observed at 0.8 V with specific capacity reaching up to 800 $mAhg^{-1}$ suggesting consumption of 7.1 mol of Li-ions (reduction of $Fe^{2+}$and Zn^{2+} to Fe^0 and Zn^0). As the potential slowly decreases to 0.01 V, generation of Li-Zn alloy and SEI seems to appear. However, after the first cycle, higher and shorter voltage plateaus stabilize at 0.95 V. For the first charge cycle, increasing plateau at 1.5 to 1.8 V is noticed. After the initial charge-discharge voltage profile, the nature of the plateaus remains the same. However, it is worth mentioning that, the specific capacity of ZF2 is higher than all other electrodes attributed to the additional channel provided by active material for Li-ions diffusion and storage[152,171,172]. Moreover, the enhanced electrochemical performance of Mn-doped $ZnFe_2O_4$ could be attributed to the polyhedron-shaped particles and reduced agglomeration among particles.

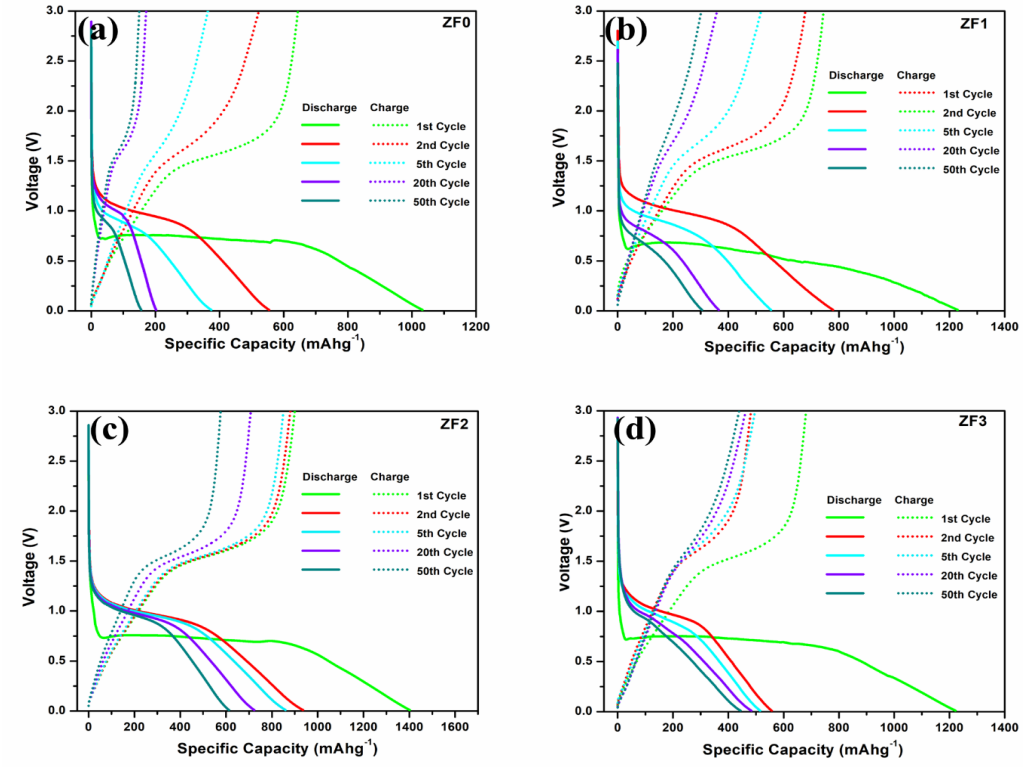

Figure 4.13 Galvanostatic Charge Discharge (GCD) curves of (a) ZF0 (b) ZF1 (c) ZF2 (d) ZF3 electrodes recorded for 1st, 2nd, 5th, 20th and 50th at a current density of 100 mAg^{-1} from 0.01 to 3.0 V.

Figure 4.14 (a) illustrates the cyclic performance and coulombic efficiency of ZF0, ZF1, ZF2, and ZF3 electrodes at a current density of 500 mAg^{-1} for 200 cycles. From Fig. 4.14(a), it is evident that the ZF2 electrode delivers much higher capacity and better cycling performance than ZF0, ZF1, and ZF3. It is worth mentioning that Mn doping in $ZnFe_2O_4$ has significantly improved the cyclic performance. After 200 cycles, ZF1, ZF2, ZF2 and ZF3 electrode exhibit specific capacity of 150 $mAhg^{-1}$, 252 $mAhg^{-1}$, 502 $mAhg^{-1}$, and 397 $mAhg^{-1}$, respectively. Figure 4.14 (b) shows the rate capability of prepared electrodes at different current densities. It can be depicted from the rate performance graph of ZF0, ZF1, ZF2, and ZF3, that rate performance kept decreasing with increasing current density. Mn doping has significantly increased the rate performance as compared to bare $ZnFe_2O_4$. On comparing Mn doped samples, ZF2 shows the best rate capability among all samples. The observed discharge capacity at various current densities has been tabulated in Table 4.4. The overall enhanced

electrochemical performance of Mn-doped electrodes could be attributed to the following reason: (i) the distinctive structural characteristics of spinel Zn ferrite which may hinder the destruction during charging-discharging cycles ;(ii) the coexistence of different oxidation states which is advantageous for fast redox reactions; (iii) the presence of Zn, Mn and Fe metals in Zn-Mn ferrite during charge-discharge catalyzed the decomposition of Li_2O phase and (iv) smaller particle size and the improved morphology of the Mn-doped $ZnFe_2O_4$ as compared to bare $ZnFe_2O_4$.

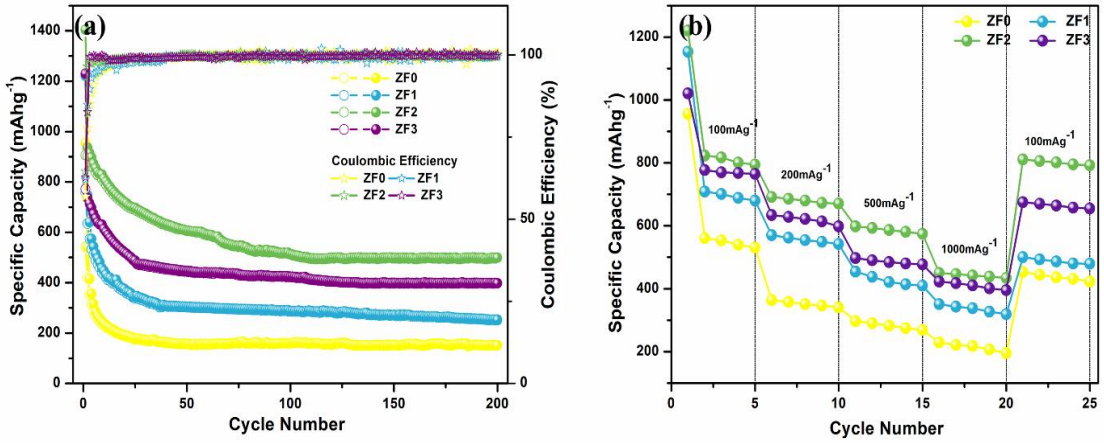

Figure 4.14 (a) Cyclic performance vs specific discharge capacity and Columbic efficiency, (b) Rate capability of ZF0, ZF1, ZF2 and ZF3 electrodes.

Table 4.4 Specific discharge capacity at various current density for ZF0, ZF1, ZF2 and ZF3 electrodes.

Current Densities (mAg^{-1})	**Specific Capacity ($mAhg^{-1}$)**			
	ZF0	**ZF1**	**ZF2**	**ZF3**
100	530	688	800	768
200	340	542	670	598
500	269	410	574	477
1000	195	319	434	395

Therefore, in this chapter, effect of Mn doping in $ZnFe_2O_4$ samples was investigated. The structural analysis revealed the good highly crystalline phase with spinel structures for all the prepared samples. Morphological analysis reveals that with an increase in Mn doping, there is a reduction of ~ 80-100 nm in the size of the particles. The electrochemical studies reveal that $Zn_{0.97}Mn_{0.03}Fe_2O_4$ (ZF2) sample showed improved electrochemical performance as compared to the other electrodes. Moreover, All the prepared electrodes exhibit dominant pseudocapacitive behaviour.

Chapter 5 : Impact of Synthesis Techniques on the Electrochemical Properties of $ZnCo_2O_4$ as Alternative Anode

In this chapter, $ZnCo_2O_4$ spinel anode has been synthesized via two different synthesis routes viz. solid-state high-energy ball milling (ZCB) and urea-assisted combustion (ZCU). The effect of the synthesis method on the physicochemical and electrochemical performance has been analyzed.

5.1 Introduction

Among the various explored anode materials, transition metal oxides (TMOs) like ZnO, NiO, Fe_2O_3, Co_3O_4, and others have been rigorously studied in recent past owing to their high theoretical capacity and cycle life[144]. In the recent past, Co-based anodes have been thoroughly explored in an attempt to replace graphitic anodes. Transition metal oxide, Co_3O_4 has gained much attention due to its high capacity and great cyclic life. However, during 1st discharge cycle, Co_3O_4 suffers irreversible capacity loss and capacity fading in the charge-discharge process due to volume expansion and contraction. To overcome this problem associated with Co_3O_4, one way is to replace a metal ion with some other metal ion that can react with Lithium by means of alloying and de-alloying process[113,173]. One such metal ion is Zn^{2+}, which can partially substitute Co with the formulation of $ZnCo_2O_4$. Since, both Zn and Co are electrochemically active with respect to lithium, $ZnCo_2O_4$ is highly attractive as an anode material for LIBs. In fact, only the bivalent Co^{2+} ions occupying the tetrahedral sites (8a) are replaced by Zn^{2+} ions, while the Co^{3+} ions remain located at the octahedral sites (16d), resulting in $ZnCo_2O_4$ with a 'normal' spinel structure[118,174]. When $ZnCo_2O_4$ is used as the anode in LIBs, it stores Lithium ions through the conversion reaction of Co oxide and also through the reaction between Zn and Li, resulting in a theoretical capacity of approximately 900 mAh/g which is similar to theoretical capacity of Co_3O_4[120]. Therefore, $ZnCo_2O_4$ is an alternative anode material with a high theoretical capacity, environmental benignity, and good recyclability as compared to Co_3O_4. However, simply replacing ions did not resolve the issues of poor Li-ion conductivity and low electronic conductivity[119]. To enhance the cyclability and Li-ion diffusion rate of $ZnCo_2O_4$, researchers have employed various strategies, such as designing different structures using diverse synthesis methods, coating with other conductive agents, or hybridizing with other materials[115,175,176]. It is well known that the synthesis route and morphology have a direct effect on the electrochemical performance.

In this chapter, $ZnCo_2O_4$ has been synthesized via two different synthesis routes viz. solid-state high-energy ball milling (ZCB) and urea-assisted combustion method (ZCU). The effect of the synthesis method on the Physicochemical and electrochemical performance has been analyzed. Synthesis details for the preparation of $ZnCo_2O_4$ via high energy ball milling has been presented in Chapter 2 section 2.1.1.3 and the synthesis process for $ZnCo_2O_4$ via Urea assisted combustion route has been also mentioned in Chapter 2 section 2.2.

5.2 Results and Discussion

5.2.1 Thermal Characterization

5.2.1.1 Thermogravimetric and Differential Thermal Analysis (TGA and DTA) Analysis

Figure 5.1 shows the TGA curves of as-synthesized ZCB and ZCU. TGA is used to determine the decomposition of mass with respect to temperature and hence the reaction route of the precursors. From Fig. 5.1, it can be seen that both ZCB and ZCU synthesis routes show similar nature of mass decomposition. For both ZCB and ZCU mass loss has been recorded in three steps. It is observed that there is a very small mass loss of ~ 5.7 % from 200 ^oC to 245 ^oC for ZCB and ~3.5% from 190 ^oC to 230 ^oC corresponding to the moisture absorbed in the sample. In the temperature interval of 245 ^oC to 350 ^oC, there is a mass loss of 45% for ZCB, and loss of ~ 47 % is observed for ZCU from 230 ^oC to 360 ^oC temperature due to the oxidation of residual carbon present in the sample. The sudden loss of 56% is observed during 350 ^oC to 750 ^oC for ZCB, and for ZCU from 360 ^oC to 650 ^oC mass loss of 50% that can be ascribed to the decomposition of metal salts present in the precursors. After 750 ^oC for ZCB and after 650 ^oC for ZCU the mass decomposition stabilizes, which confirms that there is no mass loss, suggesting the desired temperature for the phase formation of $ZnCo_2O_4$[177,178].

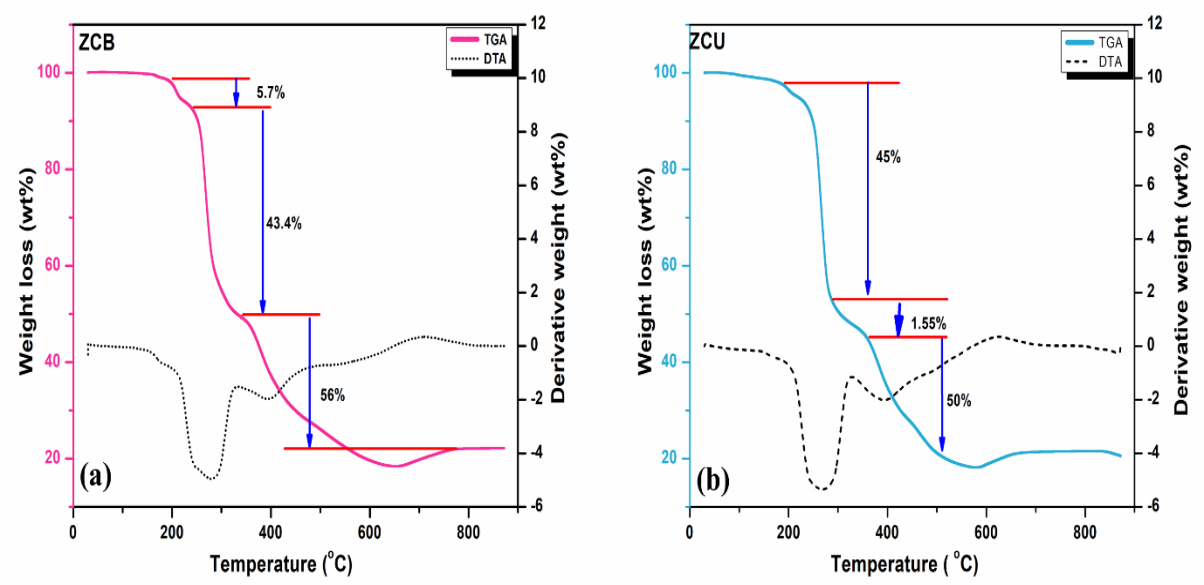

Figure 5.1 TGA curve of as-synthesized $ZnCo_2O_4$ using (a) ball milling method (ZCB) (b) urea assisted combustion method (ZCU) method at temperature interval from 30 ºC to 900 ºC.

5.2.2 Structural and Morphological Characterization

5.2.2.1 X-Ray Diffraction (XRD) Analysis

The XRD patterns of $ZnCo_2O_4$ for both the synthesis routes ZCB and ZCU are shown in Fig 5.2(a-b). All the observed peaks match well with the JCPDS card no. 01-081-2296 belonging to the spinel $ZnCo_2O_4$ structure. Peaks positioned at (111), (220), (311), (222), (400), (422), (511), and (440) are typical reflection planes of XRD patterns of $ZnCo_2O_4$. No traces of impurity are present indicating crystallinity and purity of synthesized by ZCB and ZCU. Although some missing peaks and noise can be detected in the XRD pattern of ZCB route which could be due to the route opted for synthesis[179,180]. Scherrer's formula was used to determine the crystallite size, as;

$$D = k\lambda/\beta\, cos\theta \qquad (5.1)$$

where D, λ (0.154 nm), k (0.9), β, and θ denotes the crystallite size, wavelength of X-ray radiation, Scherrer's constant, FWHM, and diffraction angle, respectively. The crystallite size

as estimated from Scherrer's formula is 70 nm and 57 nm for ZCB and ZCU techniques respectively.

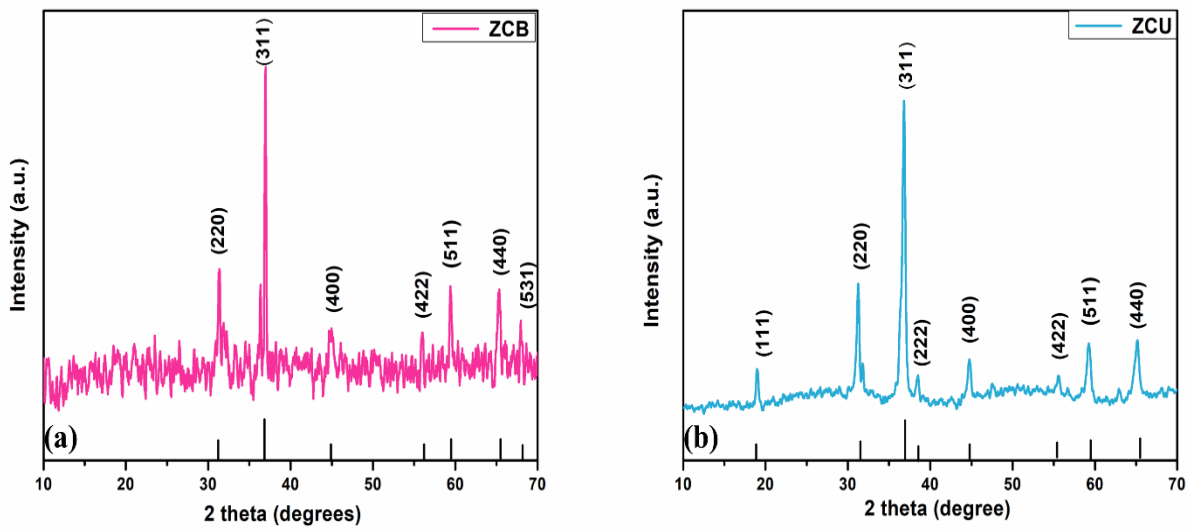

Figure 5.2 Wide range XRD pattern of (a) ZCB (b) ZCU samples recorded from 10º-90º.

5.2.2.2 Scanning Electron Microscopy (SEM) and Energy-dispersive X-ray Spectroscopy (EDX) Analysis

The morphologies of the synthesized anode material, $ZnCo_2O_4$ via high energy ball milling route (ZCB) and urea assisted combustion route (ZCU) are shown in Fig. 5.3(a-d). Fig 5.3(a-b) displays low and high magnification SEM images of ZCB sample. Figure 5.3(b) indicates that ball milled sample of $ZnCo_2O_4$ (ZCB) shows non-uniform agglomerated microstructures with an average particle size of ~49 µm. The ZCB micrograph reveals severely aggregated particles with larger diameter. It is well known that larger particle size in anode material led to poor electrochemical performance because of the long diffusion path for the lithium ions (Li+) transportation during insertion and extraction process of Li-ions. Figure 5.3 (c-d) shows the low and high magnification image of urea assisted combustion route (ZCU) sample of $ZnCo_2O_4$. As shown in Fig 5.3 (d), the morphology of ZCU sample is uniform and nearly spherical in nature. The average particle size for ZCU sample was observed to be ~20 µm. The

small particles offer short pathways for both electrons and Li-ions during the Li-ion insertion/extraction process, leading to improved electrochemical properties

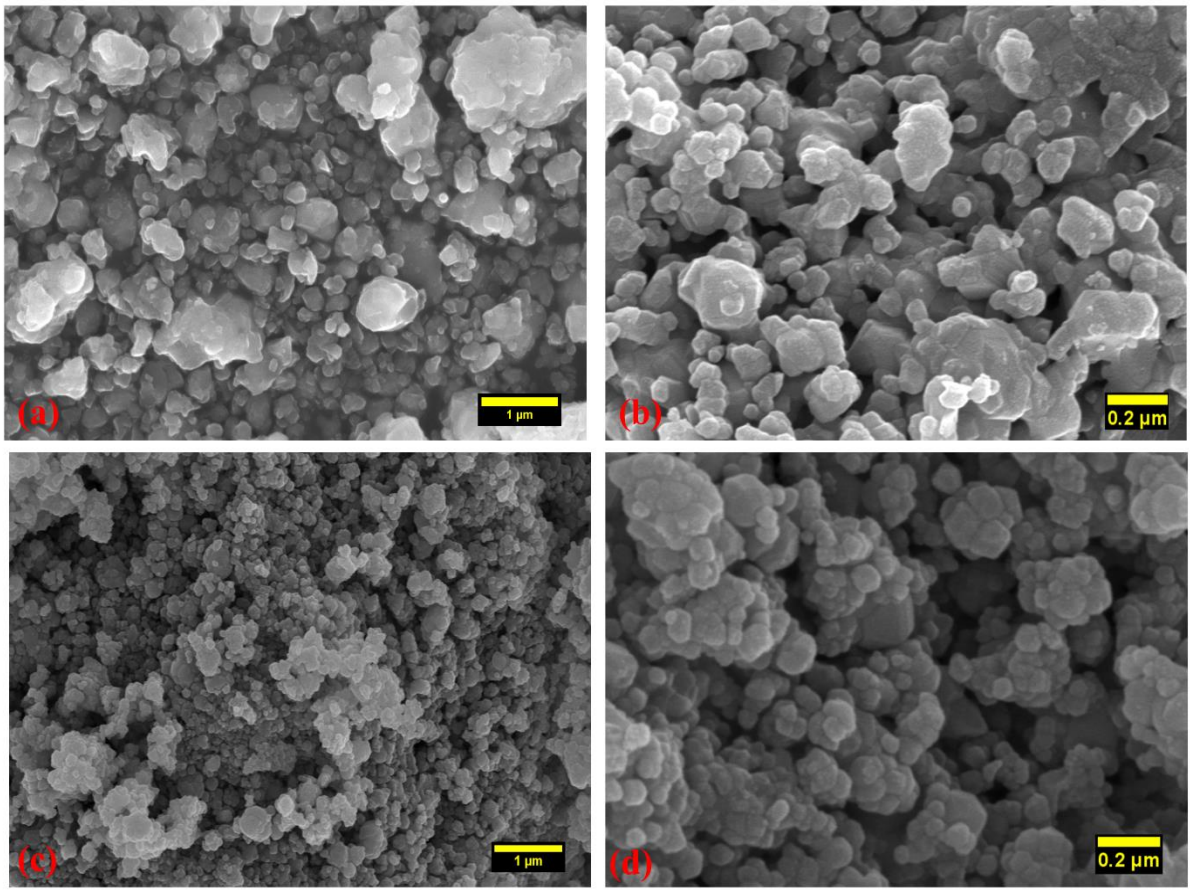

Figure 5.3 SEM micrographs observed at different magnifications for (a-b) ZCB, (c-d) ZCU.

To study the elemental composition and distribution of element in prepared samples, energy dispersive x-ray spectroscopy (EDX) is also performed to both the samples ZCB and ZCU. Figure 5.4 (a-e) and Fig. 5.5 (a-e) shows the elemental mapping and EDS spectrum for ball milled sample (ZCB) and urea assisted combustion sample (ZCU), respectively. As can be seen from the Fig. 5(a-d) and Fig. 5.5 (a-d), there is a homogeneous mixing of Zn, Co and O elements throughout the sample. Figure 5.4 (e) and Fig. 5.5 (e) depicts the quantitative analysis

for ZCB and ZCU samples. It can be seen that the both prepared samples ZCB and ZCU consist of elements Zn, Co, and O only and there are no impurities present in the samples.

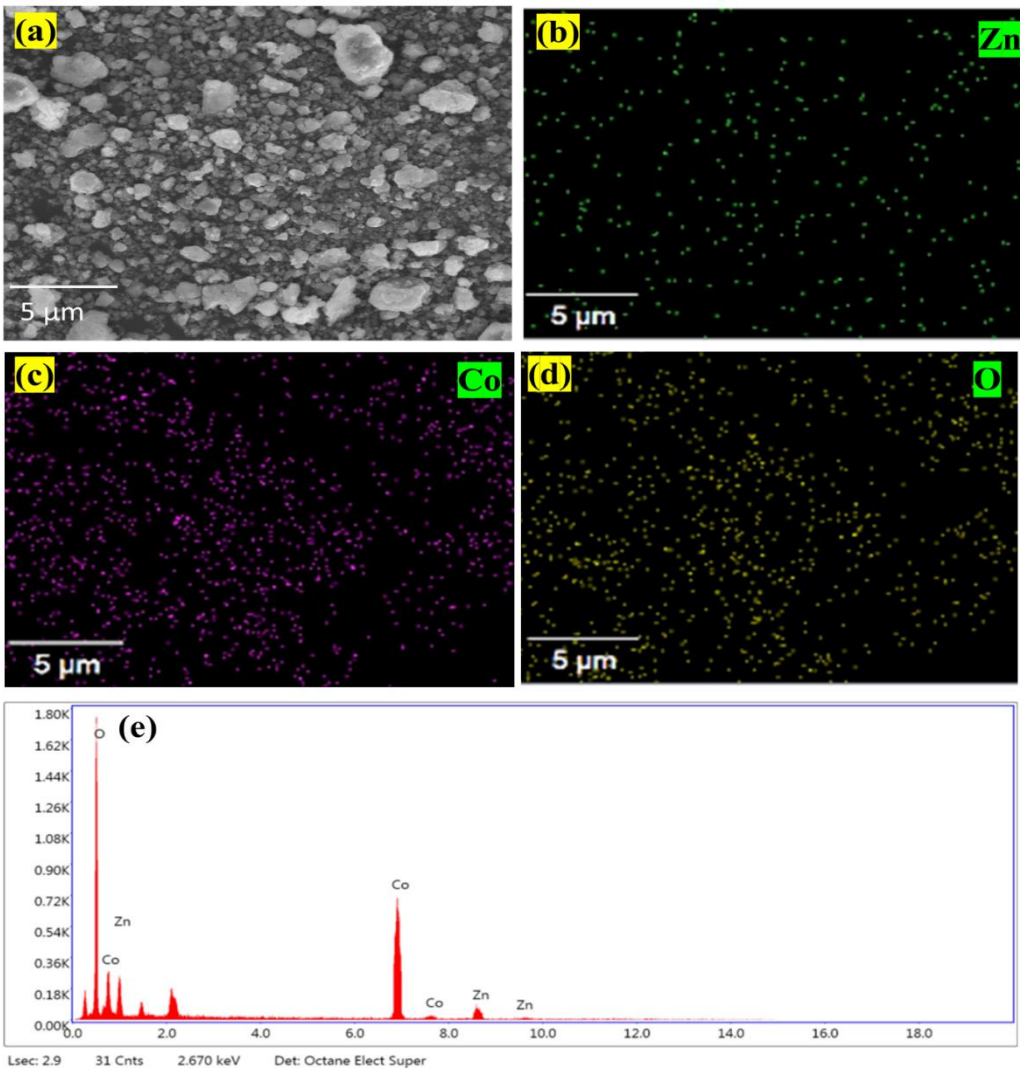

Figure 5.4 (a-d) Elemental mapping of Zn, Co and O and (e) EDX Spectrum of $ZnCo_2O_4$ prepared via ball milling route (ZCB).

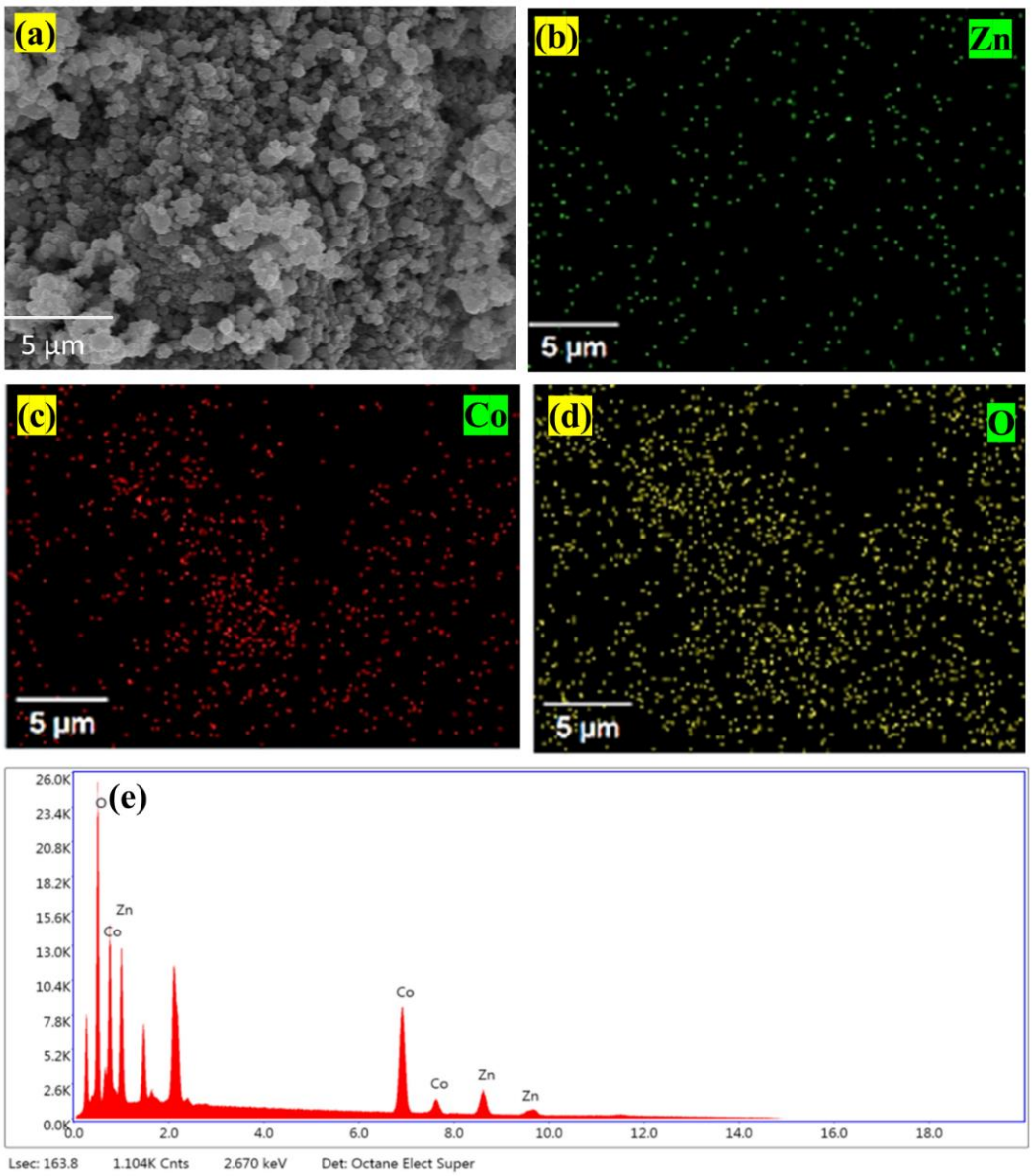

Figure 5. 5 (a-d) Elemental mapping of Zn, Co and O and (e) EDX Spectrum of $ZnCo_2O_4$ prepared via urea assisted combustion route (ZCU).

5.2.3 Vibration Analysis

5.2.3.1 Fourier Transform Infrared Spectroscopy (FTIR) Analysis

The FTIR spectrum of ZCB and ZCU samples has been shown in Fig. 5.6. FTIR is used to obtain information about the surface functional groups of $ZnCo_2O_4$ nanostructures in the range of 400 to 4000 cm^{-1}. Both the sample ZCB and ZCU indicate two intense and sharp peaks at

frequencies of ~560 cm^{-1} (Zn–O) and ~660 cm^{-1} (Co–O) in $ZnCo_2O_4$ are attributed to the strong metal-oxygen bonding in the metal oxide structure. The metal-oxygen bonds in the spinel structure appear within the regions of 560–590 cm^{-1} and 660–685 cm^{-1}, which are attributed to the F1u vibrations of the octahedral groups in $ZnCo_2O_4$[93,181,182].

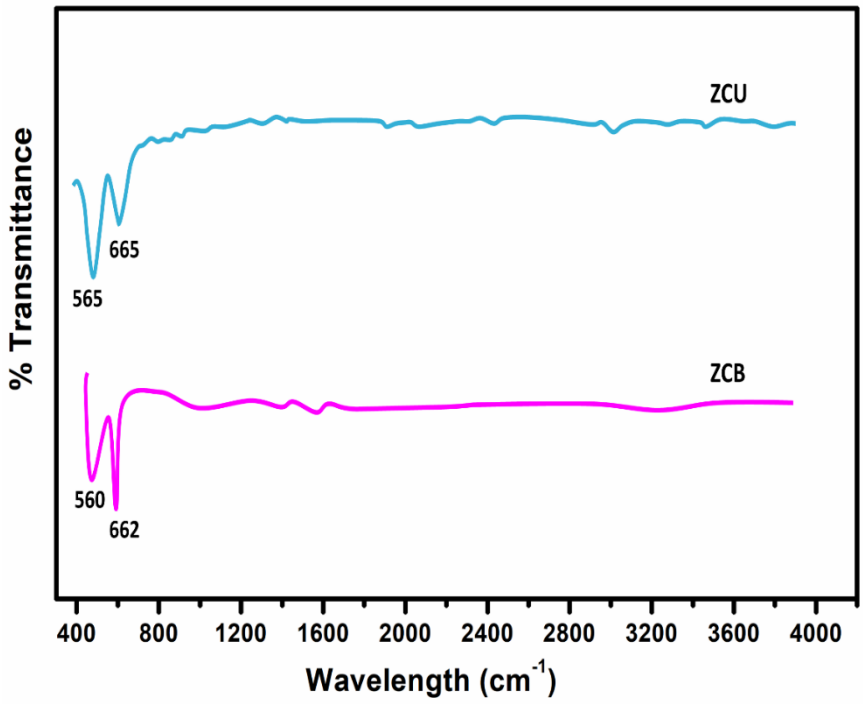

Figure 5.6 FT-IR spectrum of ZCB and ZCU samples recorded in in the range of wavenumber 400 to 4000 cm^{-1}.

5.2.4 Electrochemical Characterization

5.2.4.1 Electrochemical Impedance Spectroscopy (EIS) Analysis

EIS has been attempted at open circuit voltage (OCV) to understand the electrode-electrolyte kinetics of ZCB and ZCU at their interface. EIS is used to examine the internal impedance of a cell, which has a significant effect on the electrochemical properties. Figure 5.7 shows the EIS curves of ZCB and ZCU at OCV. As seen from the graphs, both EIS curves show a semicircular arc at a region of high frequency and an inclined straight line at region of low frequency [183]. To analyze the EIS results, the fitting of the Nyquist plot has been carried out

using an equivalent circuit. Inset of Fig 5.7 shows the equivalent circuit, where R_s, R_{ct}, C, and Z_w represent the resistance occurring due to the electrolyte, the resistance due the electrode/electrolyte interface, double layer capacitance, and Warburg impedance, respectively[184]. Fig. 5.7, shows that ZCU sample has a small diameter of the semicircle than ZCB sample, indicating that the R_{ct} value is lower for ZCU which implies that the kinetic behavior of ZCU is better than ZCB.

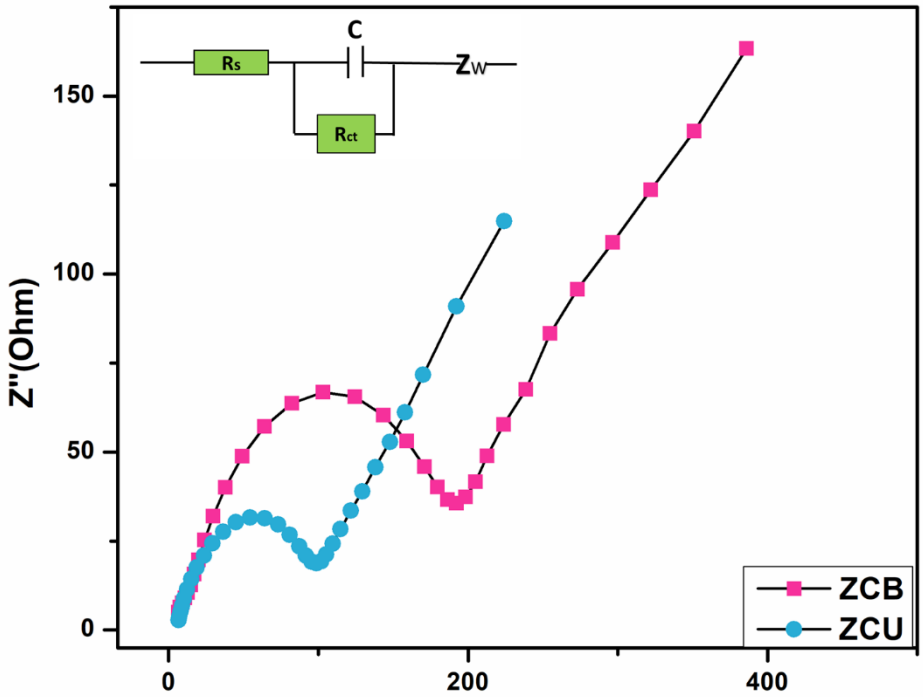

Figure 5.7 Nyquist plots of the ZCB and ZCU recorded in the frequency range 10 mHz to 100 kHz.

Figure 5.8 (a-b) shows the graph between Real impedance (Z') and square root inverse of ω (Bode plot)[185]. The diffusion coefficient for the prepared samples has been calculated using equation (3.11) as given in chapter 3.The calculated values of R_s, R_{ct}, $\sigma_\omega$and $D_{Li^+}$are given in Table 5.1.

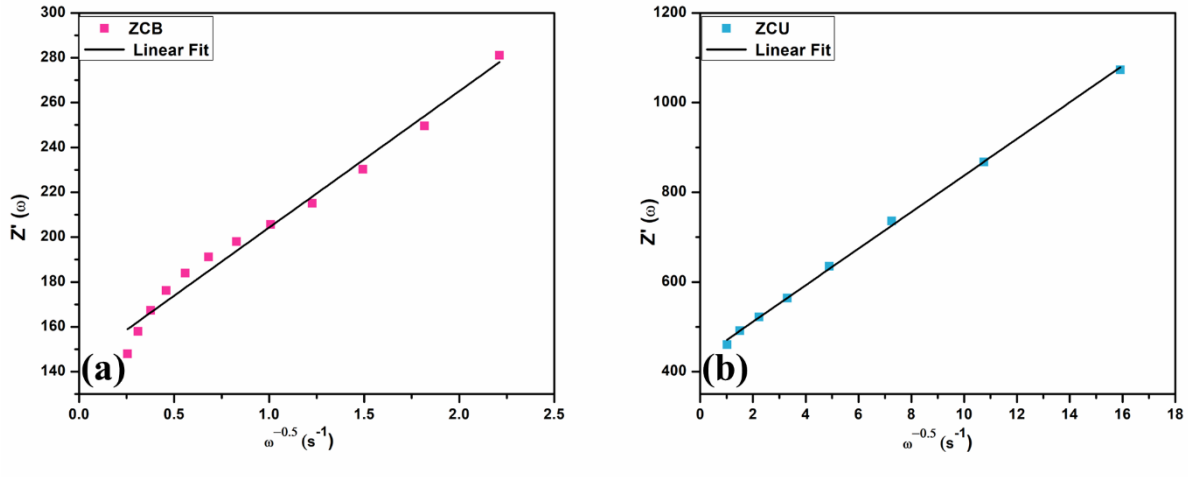

Figure 5.8 Relationship graph between real impedance (Z') and square root inverse of ω for (a) ZCB (b) ZCU.

Table 5.1 EIS Analysis of ZCB and ZCU electrodes recorded from 10 mHz to 100 kHz with the AC amplitude of 5mV

	R_s (Ω)	R_{ct} (Ω)	σ_ω ($\Omega\, s^{-1/2}$)	D_{Li^+} ($cm^2 s^{-1}$)
ZCB	5.69	207	60.56	9.32×10^{-15}
ZCU	5.58	110	40.78	2.63×10^{-14}

5.2.4.2 Cyclic Voltammetry (CV) Analysis

Cyclic Voltammetry study of ZCB and ZCU samples has been investigated at 0.05 mV/s scan rate in the voltage range 0.01 to 3.0 V for the initial 3 cycles as shown in Fig. 5.9(a-b). For ZCB sample, there is an initial cathodic process observed at 0.77 V and a peak occurring at ~ 0.42 V, which could be associated to the reduction of Zn^{2+} and Co^{3+} to $Zn^0$and Co^0. This peak then further shifts to 1.01 V for 2nd and 3rd cycle. In the anodic sweep, strong oxidation peak is present at 1.5 V resulting from the oxidation process of Zn and Co to $Zn^{2+}$and Co^{3+},which then further vanishes in 2nd and 3rd cycle[114].

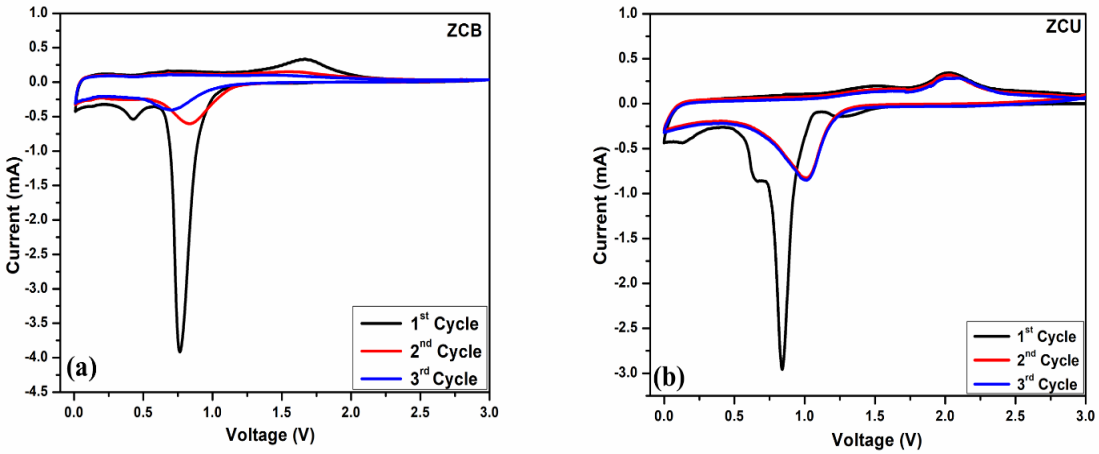

Figure 5.9 CV curves of (a) ZCB (b) ZCU recorded within the potential window (0.01-3.0V) at 0.05 mV/s scan rate.

In ZCU sample, the initial cathodic process is observed at 0.83 V and another small peak occurs at ~ 0.66 V which could be assigned to the reduction of $ZnCo_2O_4$ to the metallic Zn^o and Co^o. This cathodic peak further shifts to1.01 V for 2nd and 3rd cycles. For the anodic sweep, two main peaks are observed at 1.46 and 2.0 V characteristic of the oxidation process of Zn and Co to ZnO and CoO_x. The repeatability of CV graphs is good in ZCU whereas ZCB shows no repeatability implying the better redox activity of ZCU than ZCB. The charge discharge electrochemical reactions can be obtained as[117,186];

$$ZnCo_2O_4 + 8Li^+ + 8e^- \rightarrow Zn + 2Co + 4Li_2O \quad (5.3)$$

$$Zn + Li^+ + e^- \leftrightarrow LiZn \quad (5.4)$$

$$Zn + Li_2O \leftrightarrow ZnO + 2Li^+ + 2e^- \quad (5.5)$$

$$2Co + 2Li_2O \leftrightarrow 2CoO + 4Li^+ + 4e^- \quad (5.6)$$

$$2CoO + \frac{2}{3}Li_2O \leftrightarrow \frac{2}{3}Co_3O_4 + \frac{4}{3}Li^+ + \frac{4}{3}e^- \quad (5.7)$$

5.2.4.3 Galvanostatic Charge-Discharge (GCD) Analysis

The discharge-charge curves for initial 3 cycles for ZCB and ZCU are recorded at a constant current density of 100 mA/g with voltage lying in the range of 0.01 V to 3.0 V as shown in Fig. 5.10 (a-b). For ZCB, the initial discharge and charge capacity are determined to be 1192 mAh/g and 835 mAh/g with an initial coulombic efficiency of 70 %. The initial discharge curve of ZCB electrode exhibits notable plateau at approximately 1.0 V, as indicated by the voltage profiles. These plateaus are subsequently followed by a gradual decline in voltage down to the cut-off potential of 0.01 V. This reduction process corresponds to the reduction of $ZnCo_2O_4$ to Zn and Co, and the subsequent alloying of Zn with Li to form Li-Zn alloy. The large discharge plateau vanishes in subsequent cycles, suggesting irreversible reactions have occurred, such as the decomposition of electrolyte or due to the development of solid electrolyte interphase (SEI) layer. Moreover, the discharge from the second cycle onward, the extended discharge potential plateau is replaced by a long slope between 1.25 and 0.50 V, which is consistent with previous reports. In contrast, during charging, both Zn and Co metals can reversibly react with Li_2O to form metal oxides at potentials above 1.0 V. After initial discharge charge curve, there

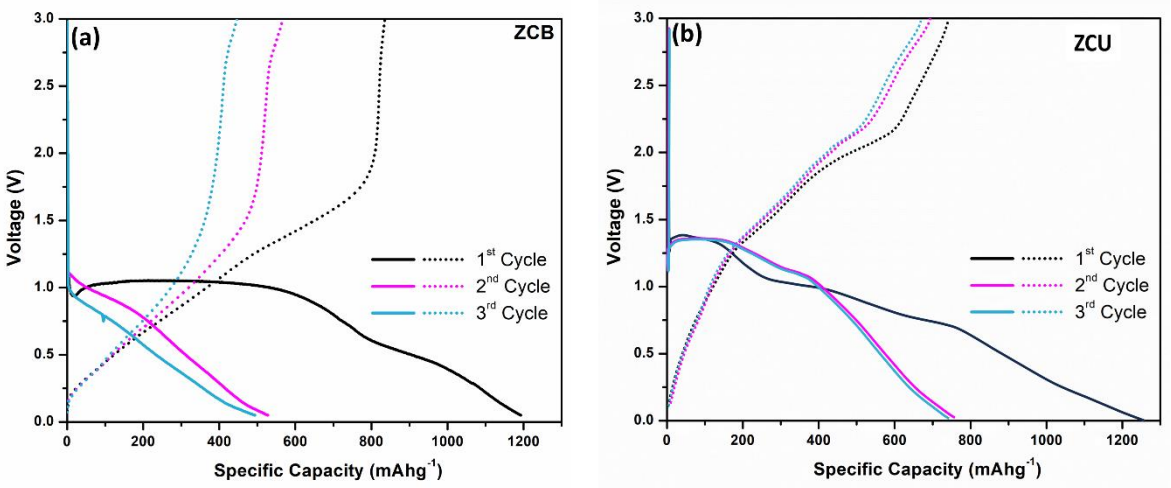

Figure 5.10 Galvanostatic discharge–charge (GCD) curves of samples (a) ZCB (b) ZCU cycled at the 1st, 2nd, and 3rd cycles at a current density of 100 mA g^{-1}.

is 50% decrement in the capacity value. In the case of ZCU (Fig 5.10(b)), during first discharge curve, ZCU electrode shows a significant voltage plateau at approximately 1.2 V. This plateau can be attributed to the decomposition of the $ZnCo_2O_4$ into Zn, Co, and Li_2O, along with the formation of solid electrolyte interphase (SEI) films[179,184,187]. These findings are consistent with the earlier CV results. The first discharge-charge capacity for ZCU is estimated to be 1225 $mAhg^{-1}$ and 735 $mAhg^{-1}$, respectively, with an initial coulombic efficiency of 60 %. After the first cycle, the discharge-charge curves of ZCU electrode overlapped better than that of ZCB implying better cycle stability of ZCU electrode. This improvement in cyclic stability could be due to the smaller particle size and better morphology of urea assisted combustion route as compared to the ball milling route.

Hence, in this chapter, physico-chemical and electrochemical properties of $ZnCo_2O_4$ via different synthesis methods has been explored. The thermal characterization through TGA and DTA reveals that mass loss occurs in three steps, confirming the desired phase formation temperatures for $ZnCo_2O_4$. Structural characterization using XRD patterns matches well with the spinel $ZnCo_2O_4$ structure, indicating crystallinity and purity, with estimated crystallite sizes of 70 nm and 57 nm for ZCB and ZCU, respectively. Bewteen both the synthesis, urea assisted combustion method display better electrochemical performance due to smaller and uniform particle size which allows more Li-ions to interact.

Chapter 6 : Investigation of $CoFe_2O_4$_MWCNT and $CoFe_2O_4$_rGO composite as anode material using sol-gel auto ignition route

This chapter includes synthesis of $CoFe_2O_4$ and its composite with reduced graphene oxide (rGO) and deals with the Multi walled carbon nanotubes (MWCNT) via a simple and cost-effective sol gel auto ignition route. Structural, morphological, and electrochemical properties are investigated for the composite material. Both the composite material exhibits excellent coulombic efficiency (98%) and cyclic stability after initial two cycles.

6.1 Introduction

First transition metal (TM) oxides are recognized as promising materials in Li-ion batteries. This is because of their significant theoretical specific capacities, which rely on conversion mechanisms involving reduction to their metallic constituents and Li_2O. The electrochemical properties of spinel Co_3O_4 have been thoroughly studied as promising Li-ion battery electrode materials because of their good redox and electrochemical properties [188,189]. However, the high cost and toxicity of cobalt restrict its widespread use as an electrode material[190]. To mitigate the cost and toxicity associated with cobalt compounds, researchers have explored various ternary metal oxides, like cobalt ferrite ($CoFe_2O_4$), which is a prominent binary transition metal oxide (TMO) has garnered significant attention for its high theoretical specific capacity (916 $mAhg^{-1}$), affordability, excellent electrical and chemical stability, and environmental friendliness. One of these promising conversion materials under study is spinel-structured cobalt ferrite ($CoFe_2O_4$), which boasts a theoretical capacity as high as 914 $mAhg^{-1}$ assuming full conversion to Co and Fe, equivalent to the insertion of $8Li^+$ per formula unit. However, $CoFe_2O_4$ shows poor electrochemical performance, as it is suffering from low electrical conductivity along with volume expansion and collapse when repeatedly charged/discharged [102,191]. To address these challenges, the construction of nanostructured electrode materials with unique architectures (such as nanofibers[192], nanotubes[193], and porous structures[194]) has been extensively adopted. Moreover, hybridizing nanosized $CoFe_2O_4$ with various carbon materials like carbon nanotubes, graphene, or fibres is considered another effective strategy[195–198]. The presence of carbon enhances the electrical conductivity of the composite and reduces the aggregation tendency of nanosized $CoFe_2O_4$ during synthesis. Additionally, carbon materials improve charge transfer kinetics, mitigate large volume changes, and alleviate structural strain during cycling, thereby enhancing cycling performance and rate capability. Various methods have been employed to produce nanohybrids

through the combination of different materials, aiming to explore their electrochemical properties. Carbonaceous materials such as graphene or carbon nanotubes (CNTs) are utilized in forming nanocomposites to enhance the electrical conductivity and electrochemical performance of ferrite nanoparticles[102,199].

In this chapter, $CoFe_2O_4$ and its composite with reduced graphene oxide (rGO) and Multi walled carbon nanotubes (MWCNT) have been attempted via a simple and cost-effective sol gel auto-combustion route followed by thermal treatment. Herein, in an attempt has been made to overcome the low electrical conductivity problem of $CoFe_2O_4$, two different carbon sources have been used to hybridize with cobalt ferrite. The effect of the addition of rGO and MWCNT on the overall electrochemical performance of $CoFe_2O_4$ have been investigated. Synthesis details of $CoFe_2O_4$ and its composite with rGO and MWCNT have been mentioned in Chapter 2 section 2.1.2.2. and are abbreviated as CFO, CFO_MWCNT and CFO_rGO corresponding to bare $CoFe_2O_4$, $CoFe_2O_4$_MWCNT and $CoFe_2O_4$_rGO samples, respectively. Physicochemical and electrochemical characteristics of synthesized material are performed as mentioned in Chapter 2 section 2.2.

6.2 Results and Discussion

6.2.1 X-ray Diffraction Analysis

The XRD spectroscopy analysis was performed at room temperature for phase identification and structural analysis of the synthesized bare $CoFe_2O_4$/CFO, $CoFe_2O_4$_MWCNT(CFO_MWCNT), and $CoFeO_4$_rGO (CFO-rGO) composites. XRD patterns for MWCNT, rGO, CFO, CFO_MWCNT and CFO_rGO are shown in Fig. 6.1. All the peaks for these three prepared samples are verified with JCPDS pattern of cubic inverse spinel-type $CoFe_2O_4$ (#22-1086) with a space group of Fd-3m[104,199]. As can be seen in the Fig 6.1, the main diffraction peaks at 18.2^o, 30.0^o, 35.4^o, 37.0^o, 43.0^o, 53.4^o,56.9^o and 62.5^o

corresponds to the crystal planes of (111), (220), (311), (222), (400), (422), (511) and (440). The formation of a single phase being cubic crystal structure with inverse spinel structure with space group being Fd-3m, can be confirmed as there are no impurity peaks present in the XRD patterns. Moreover, the XRD patterns of CFO_MWCNT and CFO_rGO are similar to that of CFO and all the characteristic peaks are well maintained, indicating that the addition of MWCNT or rGO does not alter the phase of $CoFe_2O_4$.

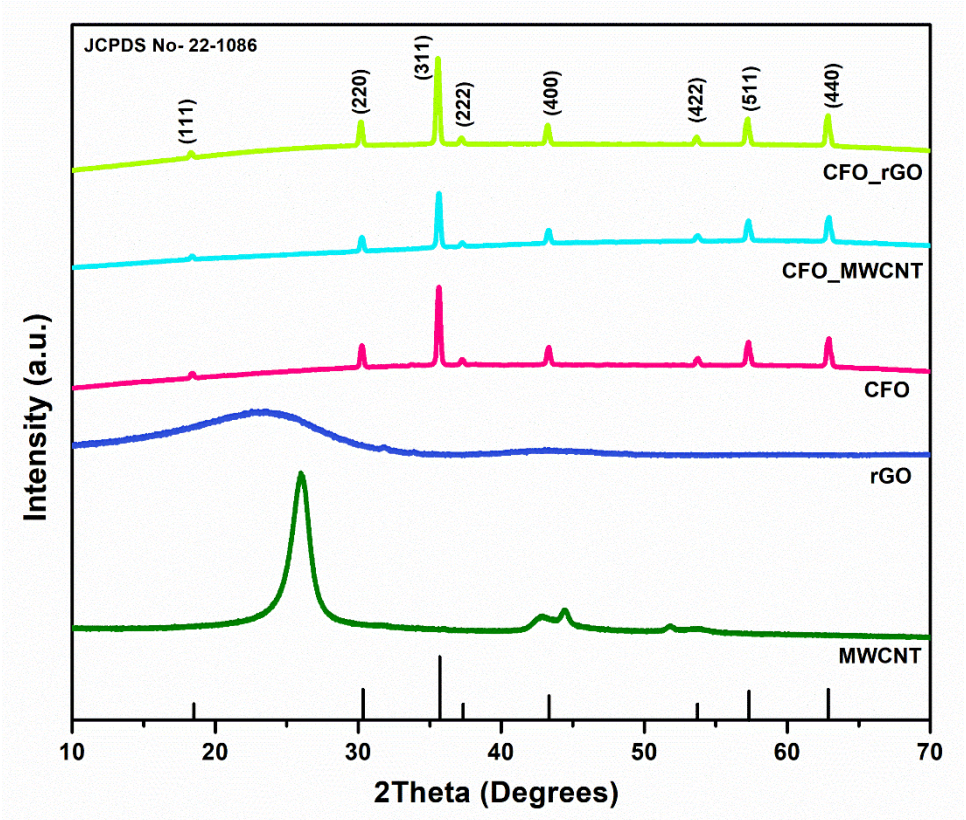

Figure 6.1 Wide angle XRD patterns of MWCNT, rGO, CFO, CFO_MWCNT and CFO_rGO recorded in the range of 10- 90°.

6.2.2 Scanning Electron Microscopy (SEM) and Energy Dispersive X-ray Analysis

FESEM was used to examine the size and morphology of the prepared samples. Figure 6.2 (a-f) shows the FESEM micrographs for CFO, CFO_MWCNT and CFO_rGO samples at low and high magnification. As can be seen from the Fig. 6.2 (a-b), CFO demonstrates the network like structure which is further confirmed by TEM. The average particle size as estimated from

ImageJ software was found to be ~ 0.1 µm for CFO. Figure 6.2 (c-d) shows the FESEM micrographs of CFO_MWCNT composite. As can be depicted from the micrographs, the surface of MWCNT is partially covered with dispersed $CoFe_2O_4$ particles. The cohesive arrangement of $CoFe_2O_4$ particles can be seen in Fig. 6.2(c-d), possibly due to their property to reduce the surface energy. This allied array of $CoFe_2O_4$ particles and MWCNT known for their excellent electrical conductivity, facilitating electron transport, and hence enhancing the electrochemical properties of the CFO_MWCNT composite. The average particle size for CFO_MWCNT composite was found to be ~0.8 µm. The CFO_rGO micrographs are demonstrated in Fig. 6.2 (e-f). It can be seen from the micrographs, $CoFe_2O_4$ particles are homogenously anchored on the surface of rGO sheet[200,201]. The average particle size for CFO_rGO composite was estimated to be around 0.15 um as calculated using ImageJ software

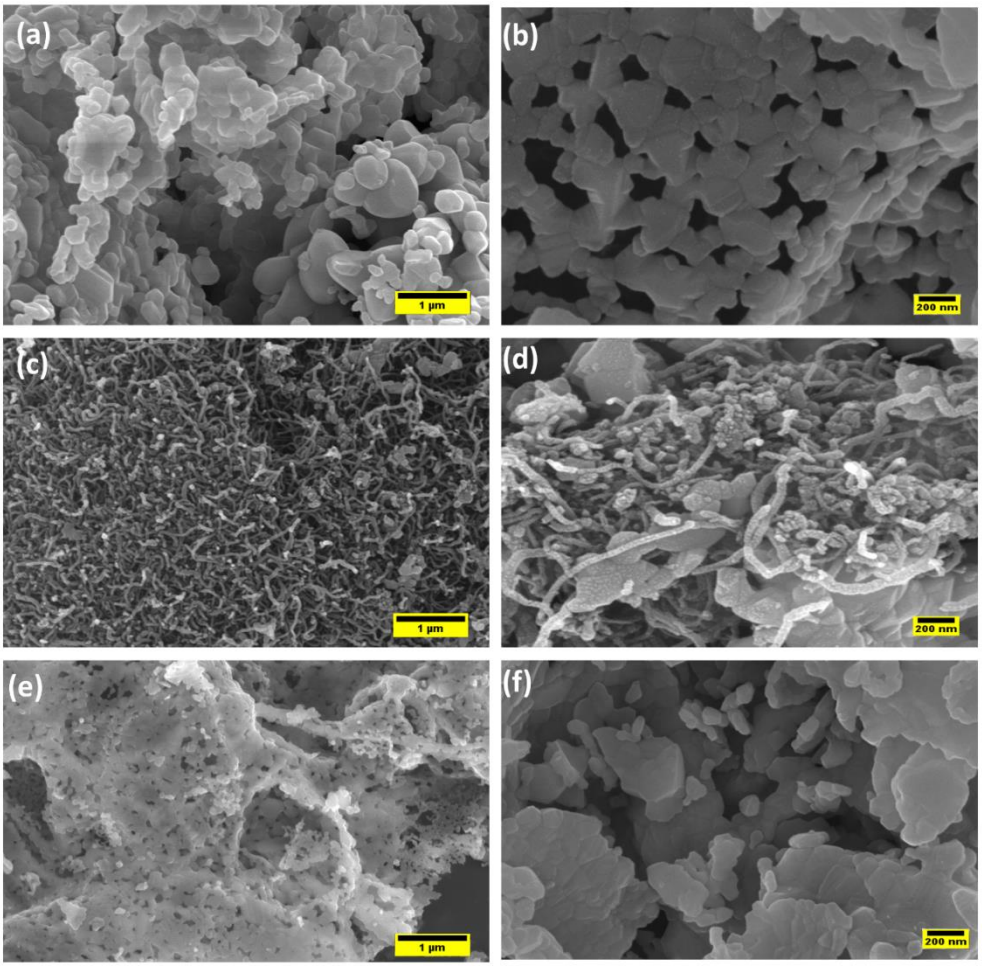

Figure 6.2 FESEM micrographs of (a-b) CFO, (c-d) CFO_MWCNT, (e-f) CFO_rGO.

Energy Dispersive X-ray Spectroscopy (EDX) is also performed for all the prepared samples to study the elemental composition and proper distribution of elements throughout the samples. Figure 6.3 (a-n) depicts the elemental mapping for CFO, CFO_MWCNT and CFO_ rGO samples. As can be seen from the EDX of CFO as shown in Fig. 6.3 (a-d), the sample consist of only Co, Fe, O elements and no other impurity is detected, confirming the homogenous mixing. Moreover, CFO_MWCNT and CFO_ rGO composite sample shows the elements Co, Fe, O and C, confirming the proper mixing of MWCNT and rGO with the $CoFe_2O_4$ sample.

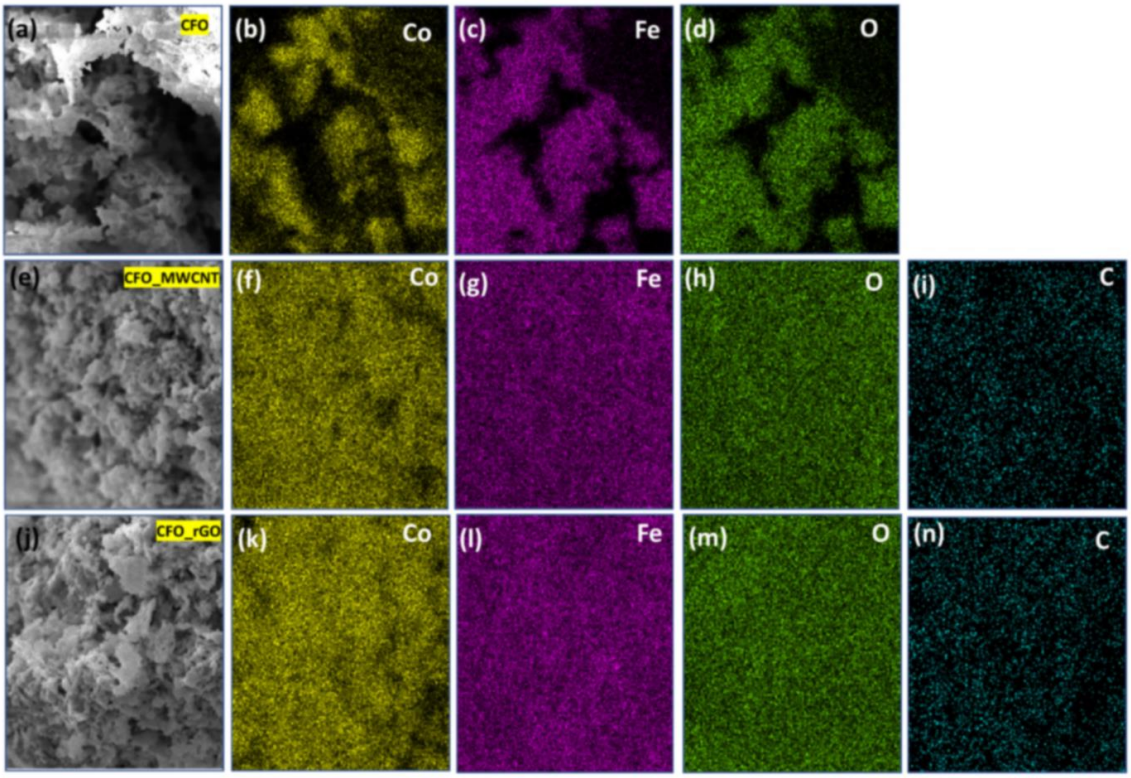

Figure 6.3 Elemental mapping images of Co (yellow), Fe (purple), C (green) of (a-d) CFO (e-i) CFO_MWCNT and (j-n) CFO_rGO.

6.2.3 Transmission Electron Microscopy (TEM) Analysis

TEM analysis has been utilized to further explore the particle size and morphologies of the prepared $CoFe_2O_4$ (CFO) and its composite with MWCNT (CFO_MWCNT) and rGO (CFO_rGO) as depicted in Fig. 6.4 (a-c). As can been seen from the Fig. 6.4(a), CFO sample shows a network like structure with an average particle size of around 40 nm. CFO_MWCNT

composite shows that the CFO particles are embedded on the surface of MWCNT as shown in Fig. 6.4 (b) having an average particle size of 35nm.

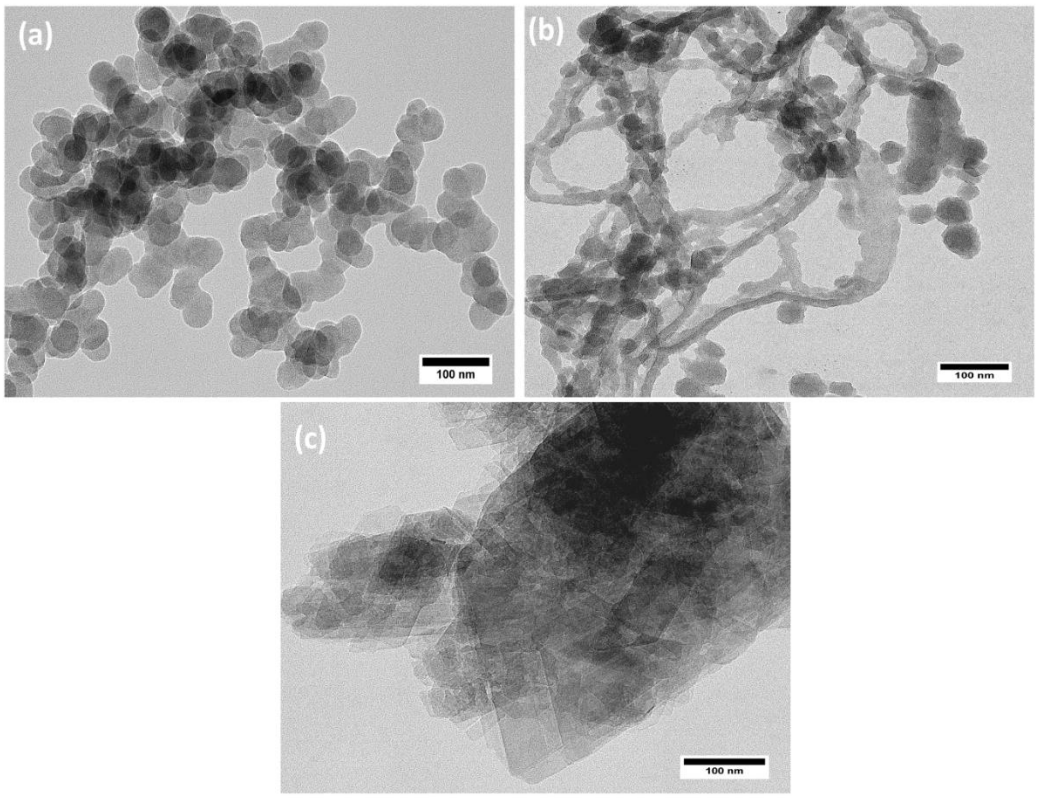

Figure 6.4 TEM micrographs of (a) CFO, (b) CFO_MWCNT, (c) CFO_rGO.

The combination of $CoFe_2O_4$ particles and MWCNT, renowned for their superior electrical conductivity, and it ultimately improve the electron transport, thus enhancing the electrochemical properties of the CFO_MWCNT composite[202]. Figure 6.4 (c) shows the TEM image for the CFO_rGO composite. As depicted in the image, CFO particles are anchored on the surface of rGO as well between the sheets of rGO.

6.2.4 Raman Analysis

The Raman spectrum of MWCNT, rGO, CFO, CFO_MWCNT and CFO_rGO has been shown in Fig. 6.5. The Raman spectrum of CFO mainly depicts four peaks located at 300 (E_g), 468(T_{2g} (2)), 628(A_{1g} (2)) and 701 cm^{-1}(A_{1g} (1)) which corresponds to the Raman active modes of $CoFe_2O_4$. The Raman bands at 300 and 468 cm^{-1} are attributed to the E_g and T_{2g} (2) modes of

$CoFe_2O_4$, resulting from the symmetric and antisymmetric bending of Oxygen atom at the octahedral sites around Fe–O and Co–O bonds. The band at 701 cm^{-1} corresponds to the

octahedral sites around Fe–O and Co–O bonds. The band at 701 cm^{-1} corresponds to the fundamental $A_{1g}(1)$ mode and is attributed to the symmetric stretching of oxygen atoms relative to the metal ions in the tetrahedral voids. The peak at 628 cm^{-1} is attributed to the $A_{1g}(2)$ sub-band mode, resulting from the distribution of Co^{2+} ions at octahedral and tetrahedral sites[203–205].

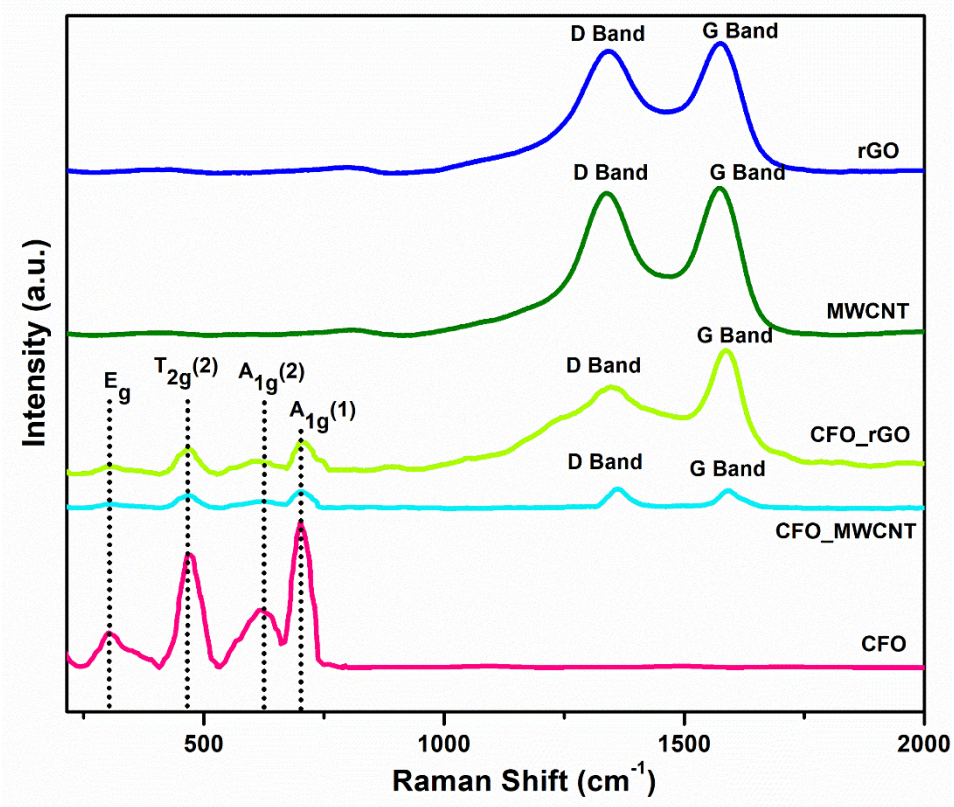

Figure 6.5 Raman spectra of MWCNT, rGO, CFO, CFO_MWCNT and CFO_rGO recorded in the range of 400-2000 cm^{-1}.

The Raman spectrum of CFO_MWCNT and CFO_rGO shows the Raman active modes at 300(E_g), 468($T_{2g}(2)$), 628($A_{1g}(2)$) and 701 cm^{-1}($A_{1g}(1)$) corresponding to cubic spinel structure of $CoFe_2O_4$ along with the carbon D (1340 cm^{-1}) band which corresponds to the disordered

structure or defects in carbon and G band (1580 cm^{-1}) which attributes to the stretching of Carbon-Carbon bond and is found in all sp^2 carbon materials[203]. The Raman analysis confirmed the presence of MWCNT and rGO in the composite material.

6.2.5 Electrochemical Characterization

6.2.5.1 Electrochemical Impedance Spectroscopy (EIS) Analysis

To examine the kinetic process of the prepared electrodes, electrochemical impedance spectroscopy (EIS) has been attempted at open circuit voltage across a frequency range from 10 mHz to 100 kHz. The beginning of the semicircle is linked to the electrode and electrolyte resistance (R_s), the high-frequency semicircle corresponds to the charge transfer resistance (R_{ct}), and the line at the end of the semicircle indicates the diffusion of Li ions. As tabulated in Table 6.1, the value of R_{ct} of the composite CFO_MWCNT and CFO_ rGO are smaller than bare CFO. It indicates that the introduction of MWCNT and rGO in CFO may improve the charge transfer process[195,202]. To further investigate the electrode kinetics, the Li^+ diffusion coefficient has been also calculated using the diffusion coefficient equation 3.11 stated in the previous chapter 3 section 3.2.2.3. The calculated values of D_{Li^+} are tabulated in Table 6.1. It is evident that the composite material shows higher diffusion coefficient that the bare material.

Table 6.1 Electrodes kinetic parameter of CFO, CFO_MWCNT and CFO_rGO samples obtained from equivalent circuit fitting for EIS analysis.

Sample	R_s	$R_{ct}(\Omega)$	$D_{Li^+}(cm^2s^{-1})$
CFO	4	265	0.26 X 10^{-17}
CFO_MWCNT	3.3	123	0.95 X 10^{-16}
CFO_rGO	4.2	63	1.00 X 10^{-15}

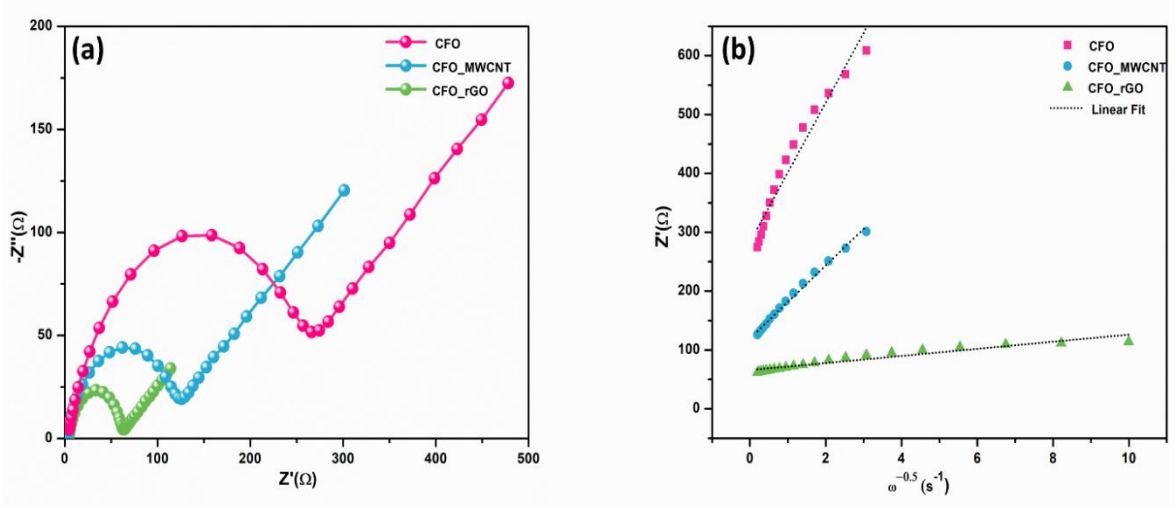

Figure 6. 6 (a) Nyquist plots of CFO, CFO_MWCNT and CFO_rGO (b) relationship between real part of resistance (Z') and inverse square root of angular frequency ($\omega^{-0.5}$).

6.2.5.2 Cyclic Voltammetry (CV) analysis

To investigate the impact of introducing MWCNT and rGO on electrochemical performance of $CoFe_2O_4$, Cyclic Voltammetry (CV) measurement of the CFO, CFO_MWCNT, and CFO_rGO electrodes are performed at a scan rate of 0.05 mV/s in the voltage window of 0.01 V to 3.0 V. Figure 6.7 (a-c) shows the CV curves of CFO, CFO_MWCNT and CFO_rGO electrode for initial three cycles. As it can be seen from the CV curves, all the three electrodes show similar redox peaks indicating the similar electrochemical reactions. During the first discharge, all three electrodes CFO, CFO_MWCNT, and CFO_rGO exhibit a dominating peak at 0.65 V,0.68 V and 0.6 V, respectively, which could be attributed to the reduction of Fe^{3+} and Co^{2+} to metallic Fe^0 and Co^0, the formation of amorphous solid Li_2O, and the irreversible reaction with the electrolyte, resulting in the formation of a solid electrolyte interface (SEI) film[206,207]. Comparing first cycle performance, the cathodic peak intensity diminishes and shifts to higher potential (1.0 V and 1.4 V) in subsequent cycles, indicating an irreversible phase transformation during the first cycle, which can lead to capacity decay or fading during

the electrochemical process. Meanwhile, weaker and broader peaks are observed during first anodic scan at around 1.67 V and 2.0 V, these peaks could be associated with the oxidation of metallic Fe^0 and Co^0 to Fe^{3+} and Co^{2+}, which shifts slightly towards higher potential (1.75 V and 2.15 V) slightly in the subsequent cycles. This shifting in anodic peak could be due to the polarization of electrode materials[202,205,206]. It is worth mentioning that subsequent cycles of CFO_MWCNT and CFO_rGO tend to stabilize and nearly overlap, indicating good electrochemical reversibility and cyclic stability. The overall electrochemical process can be summarized by following chemical reactions:

$$CoFe_2O_4 + 8Li^+ + 8e^- \rightarrow Co + 2Fe + 4Li_2O \quad (6.1)$$

$$Co + Li_2O \leftrightarrow CoO + 2Li^+ + 2e^- \quad (6.2)$$

$$2Fe + 3Li_2O \leftrightarrow Fe_2O_3 + 6Li^+ + 6e^- \quad (6.3)$$

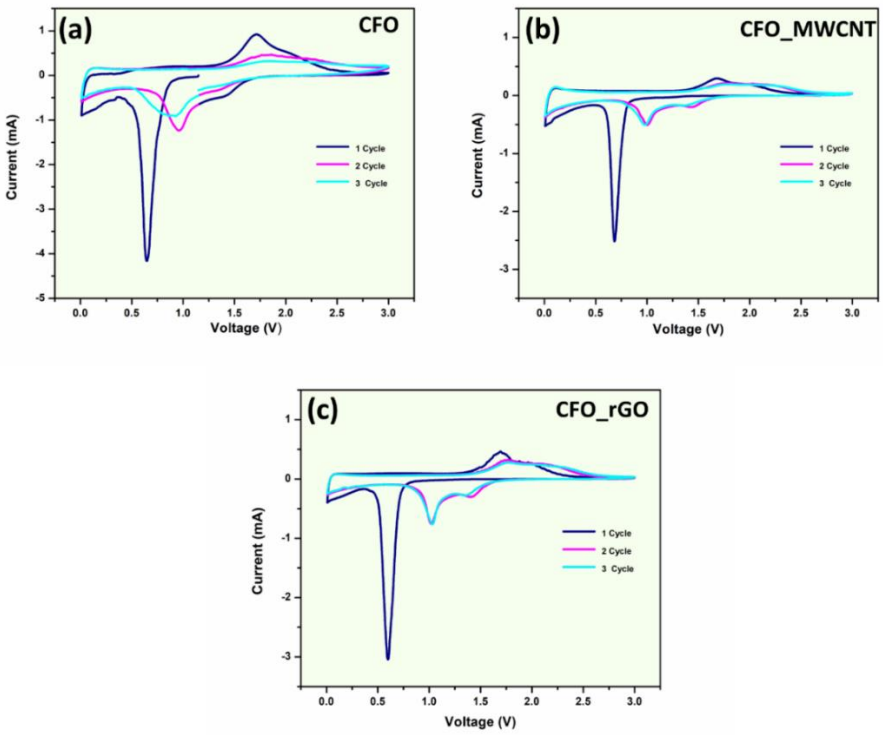

Figure 6. 7 Cyclic voltammograms (CV) curves of (a) CFO, (b) CFO_MWCNT and (c) CFO_rGO at 0.05 mV/s scan rate from 0.01 to 3.0 V.

6.2.5.3 Galvanostatic Charge-Discharge (GCD) Analysis

Figure 6.8 (a-c) presents the galvanostatic charge-discharge curves of the CFO, CFO_MWCNT, and CFO_rGO electrodes for the 1st, 2nd, and 3rd cycle at a current density of 500 mAg^{-1} within a voltage window of 0.01 to 3.00 V. All three electrodes in the initial discharge cycle shows similar voltage profile with a sharp slope at the initial discharge stage, a flat voltage plateau around 0.73 V corresponding to the reduction reaction of $CoFe_2O_4$ with lithium-ions, and an extended slope down to 0.01 V. When discharged to 0.01 V, the initial discharge capacities of the CFO, CFO_MWCNT, and CFO_rGO electrodes are 997 $mAhg^{-1}$, 1314 $mAhg^{-1}$ and 1554 $mAhg^{-1}$, respectively, these are significantly higher than the theoretical value of $CoFe_2O_4$. The increased capacity at lower potentials may be attributed to the small particle size and electrolyte decomposition, which leads to the amorphization of crystallites. The narrow electrochemical window of the electrodes can enhance the risk of electrolyte decomposition, resulting in the formation of a solid electrolyte interface (SEI) layer[192,195,202]. The SEI layer can consume Li ions due to reactions occurring during the electrochemical process. After the first discharge, the plateau at around 0.75 V shifts to 1.05 V for all the three electrodes. For the charge cycles, the voltage profile shows a plateau around 1.77 V attributing to the oxidation of metallic Fe and Co to Fe^{3+} and Co^{2+}, respectively. The first charge capacity for CFO, CFO_MWCNT, and CFO_rGO electrodes are 749 $mAhg^{-1}$, 833 $mAhg^{-1}$ and 1098 $mAhg^{-1}$. As can been seen from the discharge-charge profiles, CFO_MWCNT and CFO_ rGO electrode shows better repeatability after initial discharge/charge as compared to CFO, confirming the better electrochemical properties and kinetics for the composite electrode.

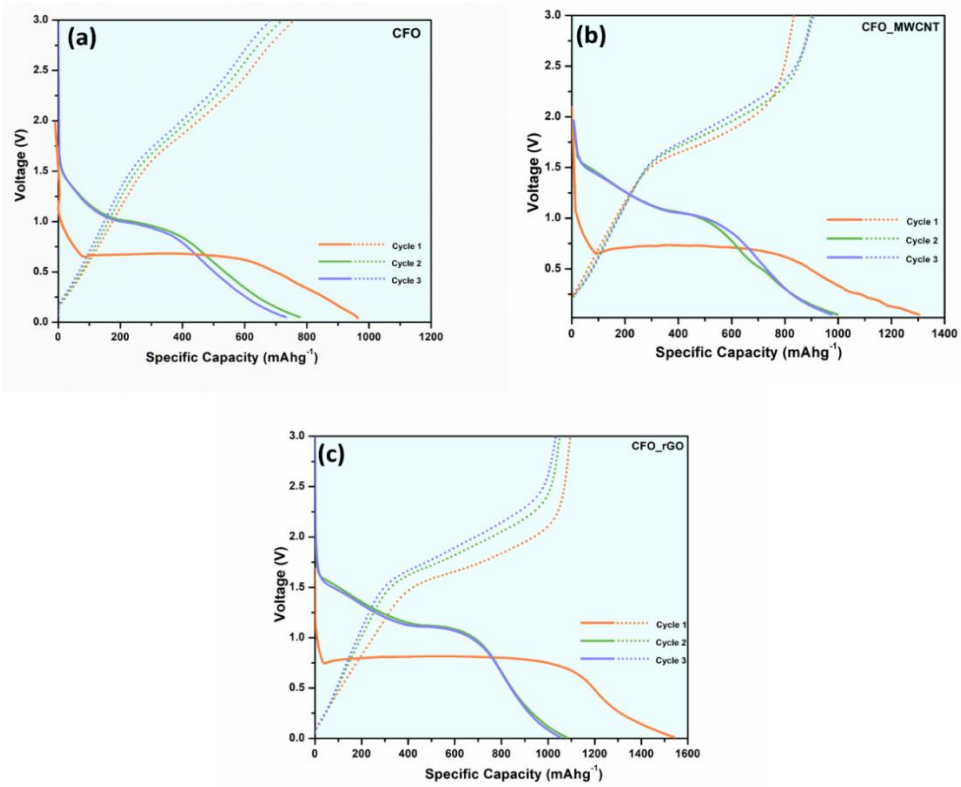

Figure 6.8 Galvanostatic charge-discharge profiles (a) CFO, (b) CFO_MWCNT and (c) CFO_rGO at a current density of 500 mAg^{-1} within a voltage window of 0.01 to 3 V.

Figure 6.9 (a-c) illustrates cyclic stability curves of the CFO, CFO_MWCNT, and CFO_rGO electrodes at 500 mA/g current density for 200 cycles. The initial discharge charge capacity for CFO, CFO_MWCNT, and CFO_rGO is 1055, 1299, and 1329 $mAhg^{-1}$with a coulombic efficiency of 76 %, 77 % and 87 %, respectively. After 200 cycles, the discharge capacities were found to be 284, 495 and 666 $mAhg^{-1}$. The coulombic efficiency after initial cycle is maintained in the range 95-99 % for all the electrodes. The increased storage capacity may be attributed to the highly stabilized interface and synergistic effects between $CoFe_2O_4$ particles and carbon additive (MWCNT and rGO). The conductive MWCNTs or rGO facilitate the transport of electrons and Li ions during charge and discharge cycles.

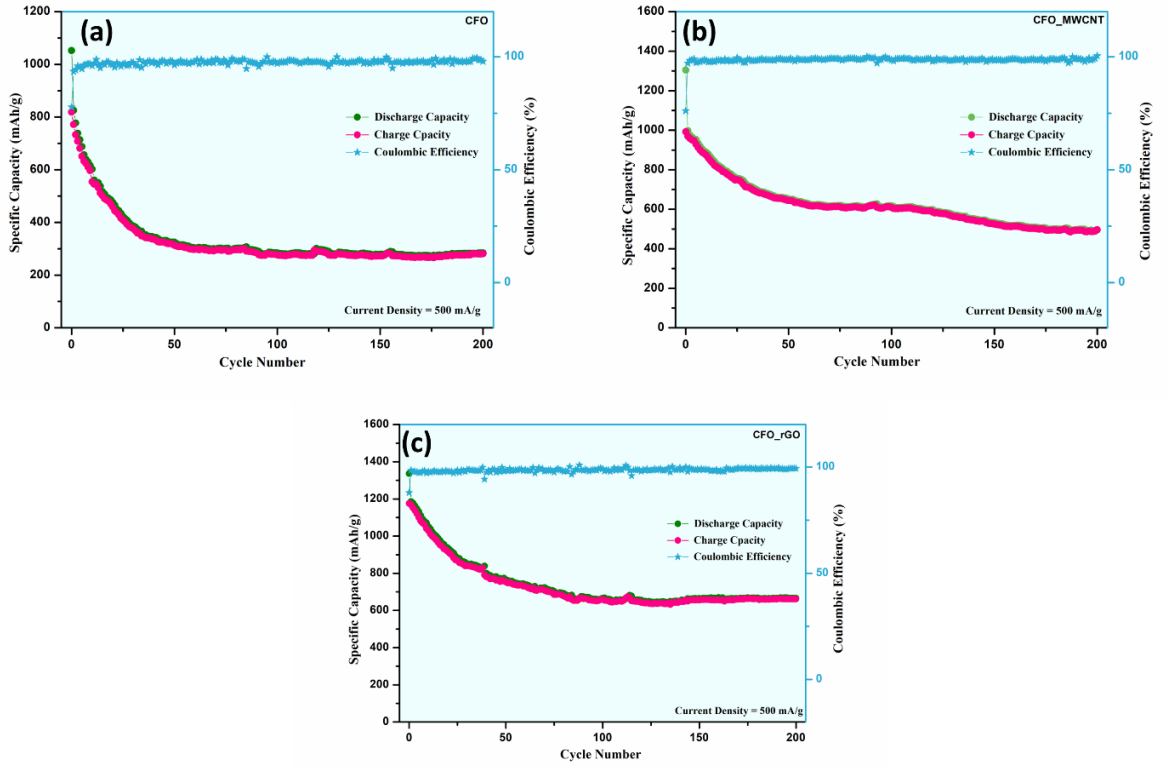

Figure 6.9 Cycling performance of (a) CFO, (b) CFO_MWCNT and (c) CFO_rGO at a current density of 500 mAg^{-1} within a voltage window of 0.01 to 3 V.

In summary, electrochemical performance of $CoFe_2O4$, $CoFe_2O_4$_MWCNT, $CoFe_2O_4$_rGO as an alternative have been investigated. XRD analysis confirm the proper phase formation of the prepared samples. Raman analysis identified characteristic peaks for $CoFe_2O_4$ and carbon materials, validating the successful synthesis and integration of the composites. Electrochemical evaluations showed that both $CoFe_2O_4$_MWCNT and $CoFe_2O_4$_rGO composites exhibit high coulombic efficiency (98%) and good cyclic stability. The composites demonstrated enhanced electrochemical performance due to the improved electrical conductivity and charge transfer kinetics provided by the carbon additives, leading to higher lithium-ion diffusion coefficients and better cycling performance compared to pure $CoFe_2O_4$.

Chapter 7 : Conclusion and Suggestion for future work

This chapter includes the summary of the results obtained in the present research work along with the outline of the future scope of this investigation

7.1 Conclusion

In this research work, a comprehensive study of the physicochemical and electrochemical performance of non-intercalation type alloy anode (SnSe) and conversion based TMOs ($ZnFe_2O$, $CoFe_2O_4$ and $ZnCo_2O_4$) have been investigated using a facile and low-cost synthesis route. Moreover, extensive research has been carried out involving doping, and composite formulations. These studies aim to enhance and analyze the electrochemical properties of the synthesized anode materials.

Initially, synthesis and electrochemical analysis of SnSe based alternative alloy anode and its composites with Super P (SnSe/C) and MWCNT (SnSe/MWCNT) have been attempted via a facile high-energy ball milling (HEBM)method. The X-ray diffraction (XRD) of the synthesized materials has been observed as an orthorhombic structure with space group, pnma without any impurities. The morphological studies have displayed irregularly shaped micro-sized particles of SnSe with the average particle size of 0.65 μm. SnSe/C and SnSe/MWCNT composite SEM shows that the super P and MWCNT are well anchored with the SnSe particles. In contrast, Energy Dispersive Spectroscopy (EDS) and Raman spectroscopy confirm the homogeneous mixing of SnSe with Super P and MWCNT. Electrochemical analysis of all three compositions has been carried to explore the specific capacity, efficiency and cyclic performance. The Li^+ diffusion coefficient is estimated using CV at different scan rates, EIS, and GITT for the SnSe, SnSe/C, and SnSe/MWCNT samples. For all three prepared anodes, the Li^+ diffusion coefficient calculated using EIS, CV, and GITT was found to be in the range of 10^{-15} cm^2s^{-1}, 10^{-14} to 10^{-15} cm^2s^{-1} and 10^{-12} to 10^{-14} cm^2s^{-1}, respectively. Among all three anode materials, SnSe/MWCNT showed higher values of Li^+ diffusion coefficient, indicating that the SnSe/MWCNT electrode has superior kinetics over SnSe/C and SnSe.

To observe the effect of doping on the electrochemical performance of $ZnFe_2O_4$, Mn-doped $ZnFe_2O_4$ in various concentrations have been synthesized via a facile and simple HEBM route. X-ray Diffraction (XRD) analysis revealed the good highly crystalline phase with spinel structures for all the prepared samples with no traces of impurity except for x= 0.05, which shows an impurity peak of α-Fe_2O_3. The morphological studies confirm the polyhedron shape and micron size particle of the prepared samples using SEM and TEM. The average particle size estimated from SEM and TEM was found to be in the range of 100 nm - 200 nm. Energy Dispersive Spectroscopy (EDS) analysis confirms the homogeneous mixing of the elements in the prepared sample. Among all the prepared samples $Zn_{0.97}Mn_{0.03}Fe_2O_4$ (ZF2) stands out the most when used as an anode, $Zn_{0.97}Mn_{0.03}Fe_2O_4$ (ZF2) delivers an excellent initial charge discharge capacity of 1405 $mAhg^{-1}$ and 900 $mAhg^{-1}$ (coulombic efficiency = 64.2 %). After 200 cycles $Zn_{0.97}Mn_{0.03}Fe_2O_4$ (ZF2) delivered a discharge capacity of 502 $mAhg^{-1}$ with a capacity retention of 35%. The rate capability of $Zn_{0.97}Mn_{0.03}Fe_2O_4$ (ZF2) at a current density of 1000 mAg^{-1} was found out to be 434 $mAhg^{-1}$. The EIS analysis reveals that the $Zn_{0.97}Mn_{0.03}Fe_2O_4$ (ZF2) electrode has the lowest resistance which implies the better transfer of Li-ions and electrons, thus resulting in enhanced electrochemical activity. Capacitive and diffusive study revealed that the lithium storage mechanism for $Zn_{1-x}Mn_xFe_2O_4$ (x = 0.0, 0.01, 0.03, 0.05) is dominated by capacitive process. The capacitive contribution of the $Zn_{0.97}Mn_{0.03}Fe_2O_4$ (ZF2) electrode reached 98% at 1 mV/s scan rate showing higher capacitive behaviour at a higher scan rate providing more active sites and transference path, further enhancing the electrochemical behaviour.

To investigate the effect of synthesis route, $ZnCo_2O_4$ is successfully synthesized via two synthesis methods: solid-state high-energy ball milling (ZCB) and urea-assisted combustion (ZCU). X-ray diffraction (XRD) confirmed the formation of a pure spinel $ZnCo_2O_4$ phase in both methods, with average crystallite sizes of 70 nm for ZCB and 57 nm for ZCU. Scanning

electron microscopy (SEM) and energy-dispersive X-ray spectroscopy (EDX) analysis showed that ZCU had a more uniform particle distribution with an average size of approximately 20 µm, compared to the more agglomerated particles of ZCB, which has average particle size of 49 µm. Fourier transform infrared spectroscopy (FTIR) identified the characteristic Zn–O and Co–O bonds in both samples, confirming the expected chemical bonding in the spinel structure. Electrochemical impedance spectroscopy (EIS) indicated that ZCU had a lower charge transfer resistance, implying better conductivity and electrochemical kinetics. Cyclic voltammetry (CV) results for ZCU displayed more consistent and stable redox peaks, indicative of reliable electrochemical activity. Galvanostatic charge-discharge (GCD) testing demonstrated that ZCU had an initial discharge capacity of 1255 $mAhg^{-1}$and a charge capacity of 910 $mAhg^{-1}$, outperforming ZCB, which had capacities of 1192 $mAhg^{-1}$and 835 $mAhg^{-1}$, respectively. This highlights the superior electrochemical performance of ZCU, suggesting it as a highly effective, stable anode material for lithium-ion batteries, with potential for high capacity and long cycle life.

Lastly, the effect of carbon additive in $CoFe_2O_4$ have been studied. $CoFe_2O_4$ and its composites with multi-walled carbon nanotubes (MWCNT) and reduced graphene oxide (rGO) have been successfully synthesized via a sol-gel auto ignition route as alternative anode materials for LIBs. The synthesis involved standard procedures, with characterization conducted using various techniques. X-ray Diffraction (XRD) confirmed the cubic inverse spinel-type structure of $CoFe_2O_4$, $CoFe_2O_4$_MWCNT and $CoFe_2O_4$_rGO with characteristic peaks indicative of pure phase formation. Scanning Electron Microscopy (SEM) and Energy Dispersive X-ray (EDX) analysis revealed the homogenous mixing of $CoFe_2O_4$ particles with MWCNT and rGO. The average particle sizes were ~0.1 µm for CFO, ~0.8 µm for CFO_MWCNT, and ~0.15 µm for CFO_rGO. Transmission electron microscopy (TEM) showed a network-like structure for CFO and a homogeneous distribution on MWCNT and rGO surfaces. Electrochemical

analysis, including cyclic voltammetry (CV) and galvanostatic charge-discharge (GCD) testing, revealed enhanced electrochemical properties for the composites. The initial discharge capacities for CFO, CFO_MWCNT, and CFO_rGO were 1055 $mAhg^{-1}$, 1299 $mAhg^{-1}$, and 1329 $mAhg^{-1}$, respectively, with corresponding charge capacities of 749 $mAhg^{-1}$, 833 $mAhg^{-1}$, and 1098 $mAhg^{-1}$. After 200 cycles, the discharge capacities decreased to 284 $mAhg^{-1}$ for CFO, 495 $mAhg^{-1}$ for CFO_MWCNT, and 666 $mAhg^{-1}$ for CFO_rGO, with coulombic efficiencies ranging from 95% to 99%. These results indicate that the addition of MWCNT and rGO significantly improves the electrochemical performance of CFO, making these composites promising anode materials for LIBs.

Based on the electrochemical performance of all the non-intercalation type anode material, it can be suggested that non-intercalation type alternative anode material have the potential to replace low-capacity intercalation anodes or materials.

7.2 Future Scope

- Coating with different materials/carbon could be achieved to improve its electrical conductivity and restrict indirect side reactions.
- All materials can be tested in full cell assembly to test the overall performance of Lithium-ion Batteries and to promote the prototype/industrial application.
- Efforts will be made to enhance the electrical conductivity and electrochemical properties by multi-doping SnSe material.
- The morphology could be enhanced in case of conversion based, $ZnFe_2O_4$ material by using different synthesis route in order to achieve nanostructures and stability of electrode.

References

[1] D. Meierrieks, Weather shocks, climate change and human health, World Dev. 138 (2021) 105228. https://doi.org/10.1016/j.worlddev.2020.105228.

[2] J. Wang, W. Azam, Natural resource scarcity, fossil fuel energy consumption, and total greenhouse gas emissions in top emitting countries, Geosci. Front. 15 (2024) 101757. https://doi.org/10.1016/j.gsf.2023.101757.

[3] L. Bruhwiler, S. Basu, J.H. Butler, A. Chatterjee, E. Dlugokencky, M.A. Kenney, A. McComiskey, S.A. Montzka, D. Stanitski, Observations of greenhouse gases as climate indicators, Clim. Change 165 (2021) 12. https://doi.org/10.1007/s10584-021-03001-7.

[4] P. Knippertz, M.J. Evans, P.R. Field, A.H. Fink, C. Liousse, J.H. Marsham, The possible role of local air pollution in climate change in West Africa, Nat. Clim. Change 5 (2015) 815–822. https://doi.org/10.1038/nclimate2727.

[5] L. Lu, X. Han, J. Li, J. Hua, M. Ouyang, A review on the key issues for lithium-ion battery management in electric vehicles, J. Power Sources 226 (2013) 272–288. https://doi.org/10.1016/j.jpowsour.2012.10.060.

[6] V. Etacheri, R. Marom, R. Elazari, G. Salitra, D. Aurbach, Challenges in the development of advanced Li-ion batteries: a review, Energy Environ. Sci. 4 (2011) 3243–3262. https://doi.org/10.1039/c1ee01598b.

[7] L. Ji, Z. Lin, M. Alcoutlabi, X. Zhang, Recent developments in nanostructured anode materials for rechargeable lithium-ion batteries, Energy Environ. Sci. 4 (2011) 2682–2699. https://doi.org/10.1039/c0ee00699h.

[8] Q. Zhang, E. Uchaker, S.L. Candelaria, G. Cao, Nanomaterials for energy conversion and storage, Chem. Soc. Rev. 42 (2013) 3127–3171. https://doi.org/10.1039/c3cs00009e.

[9] Md.H. Hossain, M.A. Chowdhury, N. Hossain, Md.A. Islam, M.H. Mobarak, Advances of lithium-ion batteries anode materials—A review, Chem. Eng. J. Adv. 16 (2023) 100569. https://doi.org/10.1016/j.ceja.2023.100569.

[10] H. Chang, Y.-R. Wu, X. Han, T.-F. Yi, Recent developments in advanced anode materials for lithium-ion batteries, Energy Mater. 1 (2021). https://doi.org/10.20517/energymater.2021.02.

[11] P. Selinis, F. Farmakis, A Review on the Anode and Cathode Materials for Lithium-Ion Batteries with Improved Subzero Temperature Performance, J. Electrochem. Soc. 169 (2022) 010526. https://doi.org/10.1149/1945-7111/ac49cc.

[12] B. Dibner, Alessandro Volta and the electric battery, New York, F. Watts, 1964. http://archive.org/details/alessandrovoltae0000dibn.

[13] C.L. Heth, Energy on demand: A brief history of the development of the battery, Substantia 1 (2019) 73–82. https://doi.org/10.13128/Substantia-280.

[14] A. Volta, On the Electricity Excited by the Mere Contact of Conducting Substances of Different Kinds, Philos. Trans. R. Soc. Lond. 90 (1800) 403–31. http://www.jstor.org/stable/107060.

[15] E. Oakes, A to Z of STS Scientists, Infobase Publishing, 2014.

[16] E. Mananga, Lithium-ion Battery and the Future, Recent Prog. Mater. 3 (2021) 1–5. https://doi.org/10.21926/rpm.2102012.

[17] D. Linden, T.B. Reddy, eds., Handbook of batteries, 3rd ed, McGraw-Hill, New York, 2002.

[18] M.S. Whittingham, Electrical energy storage and intercalation chemistry, Science 192 (1976) 1126–1127. https://doi.org/10.1126/science.192.4244.1126.

[19] J.O. Besenhard, G. Eichinger, High energy density lithium cells: Part I. Electrolytes and anodes, J. Electroanal. Chem. Interfacial Electrochem. 68 (1976) 1–18. https://doi.org/10.1016/S0022-0728(76)80298-7.

[20] N.A. Godshall, Lithium transport in ternary lithium-copper-oxygen cathode materials, Solid State Ion. 18–19 (1986) 788–793. https://doi.org/10.1016/0167-2738(86)90263-8.

[21] R. Yazami, Ph. Touzain, A reversible graphite-lithium negative electrode for electrochemical generators, J. Power Sources 9 (1983) 365–371. https://doi.org/10.1016/0378-7753(83)87040-2.

[22] A. Manthiram, J.B. Goodenough, Lithium insertion into $Fe_2(SO_4)_3$ frameworks, J. Power Sources 26 (1989) 403–408. https://doi.org/10.1016/0378-7753(89)80153-3.

[23] A. Yoshino, K. Sanechika, T. Nakajima, Secondary battery, US4668595A, 1987. https://patents.google.com/patent/US4668595A/en.

[24] C.E.L. Foss, Thermal Stability and Electrochemical Performance of Graphite Anodes in Li-ion Batteries, 2014.

[25] J.B. Goodenough, Y. Kim, Challenges for Rechargeable Li Batteries, Chem. Mater. 22 (2010) 587–603. https://doi.org/10.1021/cm901452z.

[26] C.M. Hayner, X. Zhao, H.H. Kung, Materials for Rechargeable Lithium-Ion Batteries, Annu. Rev. Chem. Biomol. Eng. 3 (2012) 445–471. https://doi.org/10.1146/annurev-chembioeng-062011-081024.

[27] A.R. Armstrong, P.G. Bruce, Synthesis of layered $LiMnO_4$ as an electrode for rechargeable lithium batteries, Nature 381 (1996) 499–500. https://doi.org/10.1038/381499a0.

[28] K. Kang, Y.S. Meng, J. Bréger, C.P. Grey, G. Ceder, Electrodes with high power and high capacity for rechargeable lithium batteries, Science 311 (2006) 977–980. https://doi.org/10.1126/science.1122152.

[29] N. Yabuuchi, T. Ohzuku, Novel lithium insertion material of $LiCo_{1/3}Ni_{1/3}Mn_{1/3}O_2$ for advanced lithium-ion batteries, J. Power Sources 119–121 (2003) 171–174. https://doi.org/10.1016/S0378-7753(03)00173-3.

[30] M. Okubo, E. Hosono, J. Kim, M. Enomoto, N. Kojima, T. Kudo, H. Zhou, I. Honma, Nanosize Effect on High-Rate Li-Ion Intercalation in $LiCoO_2$ Electrode, J. Am. Chem. Soc. 129 (2007) 7444–7452. https://doi.org/10.1021/ja0681927.

[31] J. Lu, Z. Chen, F. Pan, Y. Cui, K. Amine, High-Performance Anode Materials for Rechargeable Lithium-Ion Batteries, Electrochem. Energy Rev. 1 (2018). https://doi.org/10.1007/s41918-018-0001-4.

[32] P. Roy, S.K. Srivastava, Nanostructured anode materials for lithium-ion batteries, J. Mater. Chem. A 3 (2015) 2454–2484. https://doi.org/10.1039/C4TA04980B.

[33] R. Mukherjee, R. Krishnan, T.-M. Lu, N. Koratkar, Nanostructured Electrodes for High-Power Lithium-Ion Batteries, Nano Energy 1 (2012) 518. https://doi.org/10.1016/j.nanoen.2012.04.001.

[34] P.U. Nzereogu, A.D. Omah, F.I. Ezema, E.I. Iwuoha, A.C. Nwanya, Anode materials for lithium-ion batteries: A review, Appl. Surf. Sci. Adv. 9 (2022) 100233. https://doi.org/10.1016/j.apsadv.2022.100233.

[35] H. Cheng, J. Shapter, Y. Li, G. Gao, Recent progress of advanced anode materials of lithium-ion batteries, J. Energy Chem. 57 (2020). https://doi.org/10.1016/j.jechem.2020.08.056.

[36] N. Nitta, G. Yushin, High-Capacity Anode Materials for Lithium-Ion Batteries: Choice of Elements and Structures for Active Particles, Part. Part. Syst. Charact. 31 (2014). https://doi.org/10.1002/ppsc.201300231.

[37] S. Goriparti, E. Miele, F. De angelis, E. Di Fabrizio, R. Zaccaria, C. Capiglia, Review on recent progress of nanostructured anode materials for Li-ion batteries, J. Power Sources 257 (2014). https://doi.org/10.1016/j.jpowsour.2013.11.103.

[38] K. Mizushima, P.C. Jones, P.J. Wiseman, J.B. Goodenough, Li_xCoO_2 ($0<x<1$): A new cathode material for batteries of high energy density, Mater. Res. Bull. 15 (1980) 783–789. https://doi.org/10.1016/0025-5408(80)90012-4.

[39] J. Schwenzel, V. Thangadurai, W. Weppner, New Trends in Intercalation Compounds for Energy Storage and Conversion, 2003.

[40] A. Du Pasquier, I. Plitz, S. Menocal, G. Amatucci, A comparative study of Li-ion battery, supercapacitor and nonaqueous asymmetric hybrid devices for automotive applications, J. Power Sources 115 (2003) 171–178. https://doi.org/10.1016/S0378-7753(02)00718-8.

[41] L.-X. Yuan, Z. Wang, W.-X. Zhang, X. Hu, J. Chen, Y. Huang, J. Goodenough, Development and challenges of $LiFePO_4$ cathode material for lithium-ion batteries, Energy Environ. Sci. 4 (2010) 269–284. https://doi.org/10.1039/c0ee00029a.

[42] S. Kainat, J. Anwer, A. Hamid, N. Gull, S.M. Khan, Electrolytes in Lithium-Ion Batteries: Advancements in the Era of Twenties (2020's), Mater. Chem. Phys. 313 (2024) 128796. https://doi.org/10.1016/j.matchemphys.2023.128796.

[43] J. Xing, S. Bliznakov, L. Bonville, M. Oljaca, R. Maric, A Review of Nonaqueous Electrolytes, Binders, and Separators for Lithium-Ion Batteries, Electrochem. Energy Rev. 5 (2022) 14. https://doi.org/10.1007/s41918-022-00131-z.

[44] F.A. Soto, Y. Ma, J.M. Martinez De La Hoz, J.M. Seminario, P.B. Balbuena, Formation and Growth Mechanisms of Solid-Electrolyte Interphase Layers in Rechargeable Batteries, Chem. Mater. 27 (2015) 7990–8000. https://doi.org/10.1021/acs.chemmater.5b03358.

[45] Y. Song, L. Sheng, L. Wang, H. Xu, X. He, from separator to membrane: Separators can function more in lithium-ion batteries, Electrochem. Commun. 124 (2021) 106948. https://doi.org/10.1016/j.elecom.2021.106948.

[46] T. Zhang, J. Chen, T. Tian, B. Shen, Y. Peng, Y. Song, B. Jiang, L. Lu, H. Yao, S.-H. Yu, Sustainable Separators for High-Performance Lithium-Ion Batteries Enabled by Chemical Modifications, Adv. Funct. Mater. 29 (2019) 1902023. https://doi.org/10.1002/adfm.201902023.

[47] R. Raccichini, A. Varzi, S. Passerini, B. Scrosati, The role of graphene for electrochemical energy storage, Nat. Mater. 14 (2015) 271–279. https://doi.org/10.1038/nmat4170.

[48] C. Liu, F. Li, L.-P. Ma, H.-M. Cheng, Advanced Materials for Energy Storage, Adv. Mater. 22 (2010) 28–62. https://doi.org/10.1002/adma.200903328.

[49] E. Yoo, J. Kim, E. Hosono, H. Zhou, T. Kudo, I. Honma, Large Reversible Li Storage of Graphene Nanosheet Families for Use in Rechargeable Lithium-Ion Batteries, Nano Lett. 8 (2008) 2277–2282. https://doi.org/10.1021/nl800957b.

[50] L. Yang, J. Hu, A. Dong, D. Yang, Novel Fe_3O_4-CNTs nanocomposite for Li-ion batteries with enhanced electrochemical performance, Electrochimica Acta 144 (2014) 235–242. https://doi.org/10.1016/j.electacta.2014.08.099.

[51] A. Moretti, G.-T. Kim, D. Bresser, K. Renger, E. Paillard, R. Marassi, M. Winter, S. Passerini, Investigation of different binding agents for nanocrystalline anatase TiO2 anodes and its application in a novel, green lithium-ion battery, J. Power Sources 221 (2013) 419–426. https://doi.org/10.1016/j.jpowsour.2012.07.142.

[52] J. Gao, C. Jiang, J. Ying, C. Wan, Preparation and characterization of high-density spherical $Li_4Ti_5O_{12}$ anode material for lithium secondary batteries, J. Power Sources 155 (2006) 364–367. https://doi.org/10.1016/j.jpowsour.2005.04.008.

[53] B. Wang, B. Luo, X. Li, L. Zhi, The dimensionality of Sn anodes in Li-ion batteries, Mater. Today 15 (2012) 544–552. https://doi.org/10.1016/S1369-7021(13)70012-9.

[54] X. Su, Q. Wu, J. Li, X. Xiao, A. Lott, W. Lu, B.W. Sheldon, J. Wu, Silicon-Based Nanomaterials for Lithium-Ion Batteries: A Review, Adv. Energy Mater. 4 (2014) 1300882. https://doi.org/10.1002/aenm.201300882.

[55] M.N. Obrovac, V.L. Chevrier, Alloy Negative Electrodes for Li-Ion Batteries, Chem. Rev. 114 (2014) 11444–11502. https://doi.org/10.1021/cr500207g.

[56] D. Larcher, J.-M. Tarascon, Towards greener and more sustainable batteries for electrical energy storage, Nat. Chem. 7 (2015) 19–29. https://doi.org/10.1038/nchem.2085.

[57] K. Zhang, X. Han, Z. Hu, X. Zhang, Z. Tao, J. Chen, Nanostructured Mn-based oxides for electrochemical energy storage and conversion, Chem. Soc. Rev. 44 (2015) 699–728. https://doi.org/10.1039/C4CS00218K.

[58] Y. Zhang, L. Li, H. Su, W. Huang, X. Dong, Binary metal oxide: advanced energy storage materials in supercapacitors, J. Mater. Chem. A 3 (2014) 43–59. https://doi.org/10.1039/C4TA04996A.

[59] C. Yuan, H.B. Wu, Y. Xie, X.W. (David) Lou, Mixed Transition-Metal Oxides: Design, Synthesis, and Energy-Related Applications, Angew. Chem. Int. Ed. 53 (2014) 1488–1504. https://doi.org/10.1002/anie.201303971.

[60] M. Winter, J.O. Besenhard, Electrochemical lithiation of tin and tin-based intermetallics and composites, Electrochimica Acta 45 (1999) 31–50. https://doi.org/10.1016/S0013-4686(99)00191-7.

[61] H. Li, Z. Wang, L. Chen, X. Huang, Research on Advanced Materials for Li-ion Batteries, Adv. Mater. 21 (2009) 4593–4607. https://doi.org/10.1002/adma.200901710.

[62] W. Sun, H. Li, Y. Wang, Microwave-assisted synthesis of graphene nanocomposites: recent developments on lithium-ion batteries, Rep. Electrochem. 5 (2015) 1–19. https://doi.org/10.2147/RIE.S65118.

[63] L. Xue, Z. Fu, Y. Yao, T. Huang, A. Yu, Three-dimensional porous Sn–Cu alloy anode for lithium-ion batteries, Electrochimica Acta 55 (2010) 7310–7314. https://doi.org/10.1016/j.electacta.2010.07.015.

[64] J. Hassoun, G. Mulas, S. Panero, B. Scrosati, Ternary Sn-Co-C Li-ion battery electrode material prepared by high energy ball milling, Electrochem. Commun. 9 (2007) 2075–2081. https://doi.org/10.1016/j.elecom.2007.05.033.

[65] Q. Fan, P. Chupas, M. Whittingham, Characterization of Amorphous and Crystalline Tin–Cobalt Anodes, Electrochem. Solid State Lett. - Electrochem Solid State Lett 10 (2007). https://doi.org/10.1149/1.2789418.

[66] X.-L. Wang, W.-Q. Han, J. Chen, J. Graetz, Single-crystal intermetallic M-Sn (M = Fe, Cu, Co, Ni) nanospheres as negative electrodes for lithium-ion batteries, ACS Appl. Mater. Interfaces 2 (2010) 1548–1551. https://doi.org/10.1021/am100218v.

[67] C. Yang, D. Zhang, Y. Zhao, Y. Lu, L. Wang, J. Goodenough, Nickel foam supported Sn–Co alloy film as anode for lithium-ion batteries, Lancet 196 (2011) 10673–10678. https://doi.org/10.1016/j.jpowsour.2011.08.089.

[68] C. Marino, M.T. Sougrati, A. Darwiche, J. Fullenwarth, B. Fraisse, J. Jumas, L. Monconduit, Study of the series $Ti_{1-y}N$ by SnSb with $0 < y < 1$ as anode material for Li-ion batteries, J Power Sources 244 (2013) 736–741.

[69] C.-M. Park, J.-H. Kim, H. Kim, H.-J. Sohn, Li-alloy based anode materials for Li secondary batteries, Chem. Soc. Rev. 39 (2010) 3115–3141. https://doi.org/10.1039/B919877F.

[70] D. Guan, J. Li, X. Gao, C. Yuan, A comparative study of enhanced electrochemical stability of tin–nickel alloy anode for high-performance lithium-ion battery, J. Alloys Compd. 617 (2014) 464–471. https://doi.org/10.1016/j.jallcom.2014.08.036.

[71] P. Nithyadharseni, M.V. Reddy, B. Nalini, M. Kalpana, B.V.R. Chowdari, Sn-based Intermetallic Alloy Anode Materials for the Application of Lithium-Ion Batteries, Electrochimica Acta 161 (2015) 261–268. https://doi.org/10.1016/j.electacta.2015.02.057.

[72] L. D, J. S, N. B, P.C. Selvin, Compound semiconducting SnSb alloy anodes for Li ion batteries: effect of elemental composition of Sn–Sb, Semicond. Sci. Technol. 35 (2020) 045008. https://doi.org/10.1088/1361-6641/ab708d.

[73] C. Tan, G. Qi, Y. Li, J. Guo, X. Wang, D. Kong, H. Wang, S. Zhang, Performance enhancement of Sn–Co alloys for lithium-ion battery by electrochemical dissolution treatment, J. Alloys Compd. 574 (2013) 206–211. https://doi.org/10.1016/j.jallcom.2013.03.291.

[74] H.S. Im, Y.R. Lim, Y.J. Cho, J. Park, E.H. Cha, H.S. Kang, Germanium and Tin Selenide Nanocrystals for High-Capacity Lithium-Ion Batteries: Comparative Phase Conversion of Germanium and Tin, J. Phys. Chem. C 118 (2014) 21884–21888. https://doi.org/10.1021/jp507337c.

[75] H.X. Dang, K.C. Klavetter, M.L. Meyerson, A. Heller, C.B. Mullins, Tin microparticles for a lithium-ion battery anode with enhanced cycling stability and efficiency derived from Se-doping, J. Mater. Chem. A 3 (2015) 13500–13506. https://doi.org/10.1039/C5TA02131F.

[76] M. Kumar, S. Rani, Y. Singh, K. Singh Gour, V. Nand Singh, Tin-selenide as a futuristic material: properties and applications, RSC Adv. 11 (2021) 6477–6503. https://doi.org/10.1039/D0RA09807H.

[77] M.Z. Xue, J. Yao, S.-C. Cheng, Z.-W. Fu, Lithium Electrochemistry of a Novel SnSe Thin-Film Anode, J. Electrochem. Soc. 153 (2006) A270–A274. https://doi.org/10.1149/1.2139871.

[78] J. Choi, J. Jin, I. Jung, J. Kim, S. Son, SnSe2 nanoplate-graphene composites as anode materials for lithium-ion batteries, Chem. Commun. Camb. Engl. 47 (2011) 5241–3. https://doi.org/10.1039/c1cc10317b.

[79] Z. Zhang, X. Zhao, J. Li, SnSe/carbon nanocomposite synthesized by high energy ball milling as an anode material for sodium-ion and lithium-ion batteries, Electrochimica Acta 176 (2015) 1296–1301. https://doi.org/10.1016/j.electacta.2015.07.140.

[80] P. Poizot, S. Laruelle, S. Grugeon, L. Dupont, J.M. Tarascon, Nano-sized transition-metal oxides as negative-electrode materials for lithium-ion batteries, Nature 407 (2000) 496–499. https://doi.org/10.1038/35035045.

[81] J. Cabana, L. Monconduit, D. Larcher, M.R. Palacín, Beyond Intercalation-Based Li-Ion Batteries: The State of the Art and Challenges of Electrode Materials Reacting Through Conversion Reactions, Adv. Mater. 22 (2010) E170–E192. https://doi.org/10.1002/adma.201000717.

[82] F. Cheng, Z. Tao, J. Liang, J. Chen, Template-Directed Materials for Rechargeable Lithium-Ion Batteries, Chem. Mater. 20 (2008) 667–681. https://doi.org/10.1021/cm702091q.

[83] A.S. Aricò, P. Bruce, B. Scrosati, J.-M. Tarascon, W. van Schalkwijk, Nanostructured materials for advanced energy conversion and storage devices, Nat. Mater. 4 (2005) 366–377. https://doi.org/10.1038/nmat1368.

[84] B. Das, M.V. Reddy, S. Tripathy, B.V.R. Chowdari, A disc-like Mo-metal cluster compound, $Co_2Mo_3O_8$, as a high-capacity anode for lithium-ion batteries, RSC Adv. 4 (2014) 33883–33889. https://doi.org/10.1039/C4RA05620E.

[85] S. Yuvaraj, R.K. Selvan, Y.S. Lee, An overview of AB_2O_4 and A_2BO_4-structured negative electrodes for advanced Li-ion batteries, RSC Adv. 6 (2016) 21448–21474. https://doi.org/10.1039/C5RA23503K.

[86] C.N. Chinnasamy, A. Narayanasamy, N. Ponpandian, K. Chattopadhyay, K. Shinoda, B. Jeyadevan, K. Tohji, K. Nakatsuka, T. Furubayashi, I. Nakatani, Mixed spinel structure in nanocrystalline $NiFe_2O_4$ Phys. Rev. B 63 (2001) 184108. https://doi.org/10.1103/PhysRevB.63.184108.

[87] D. Carta, M.F. Casula, A. Falqui, D. Loche, G. Mountjoy, C. Sangregorio, A. Corrias, A Structural and Magnetic Investigation of the Inversion Degree in Ferrite Nanocrystals MFe_2O_4 (M = Mn, Co, Ni), J. Phys. Chem. C 113 (2009) 8606–8615. https://doi.org/10.1021/jp901077c.

[88] C.W. Jung, P. Jacobs, Physical and chemical properties of superparamagnetic iron oxide MR contrast agents: ferumoxides, ferumoxtran, ferumoxsil, Magn. Reson. Imaging 13 (1995) 661–674. https://doi.org/10.1016/0730-725x(95)00024-b.

[89] N. Ikenaga, Y. Ohgaito, H. Matsushima, T. Suzuki, Preparation of Zinc Ferrite in the Presence of Carbon Material and Its Application to Hot-Gas Cleaning, Fuel 83 (2004) 661–669. https://doi.org/10.1016/j.fuel.2003.08.019.

[90] J. Liu, O. Gutfleisch, E. Fullerton, D.J. Sellmyer, Nanoscale Magnetic Materials and Applications, 2009. https://doi.org/10.1007/978-0-387-85600-1.

[91] Y. Yin, B. Zhang, X. Zhang, J. Xu, S. Yang, Nano $MgFe_2O_4$ synthesized by sol–gel auto-combustion method as anode materials for lithium-ion batteries, J. Sol-Gel Sci. Technol. 66 (2013) 540–543. https://doi.org/10.1007/s10971-013-2967-z.

[92] D.S. Mathew, R.-S. Juang, An overview of the structure and magnetism of spinel ferrite nanoparticles and their synthesis in microemulsions, Chem. Eng. J. 129 (2007) 51–65. https://doi.org/10.1016/j.cej.2006.11.001.

[93] A. Shanmugavani, R. Kalai Selvan, S. Layek, C. Sanjeeviraja, Size dependent electrical and magnetic properties of $ZnFe_2O_4$ nanoparticles synthesized by the combustion method: Comparison between aspartic acid and glycine as fuels, J. Magn. Magn. Mater. 354 (2014) 363–371. https://doi.org/10.1016/j.jmmm.2013.11.018.

[94] Y. Sharma, N. Sharma, G.V.S. Rao, B.V.R. Chowdari, Li-storage and cyclability of urea combustion derived $ZnFe_2O_4$ as anode for Li-ion batteries, Electrochimica Acta 53 (2008) 2380–2385. https://doi.org/10.1016/j.electacta.2007.09.059.

[95] P.F. Teh, Y. Sharma, S.S. Pramana, M. Srinivasan, Nanoweb anodes composed of one-dimensional, high aspect ratio, size tunable electrospun $ZnFe_2O_4$ nanofibers for lithium-ion batteries, J. Mater. Chem. 21 (2011) 14999–15008. https://doi.org/10.1039/C1JM12088C.

[96] X. Yao, J. Kong, D. Zhou, C. Zhao, R. Zhou, X. Lu, Mesoporous zinc ferrite/graphene composites: Towards ultra-fast and stable anode for lithium-ion batteries, Carbon 79 (2014) 493–499. https://doi.org/10.1016/j.carbon.2014.08.007.

[97] Z. Xing, Z. Ju, J. Yang, H. Xu, Y. Qian, One-step hydrothermal synthesis of $ZnFe_2O_4$ nano-octahedrons as a high-capacity anode material for Li-ion batteries, Nano Res. 5 (2012) 477–485. https://doi.org/10.1007/s12274-012-0233-2.

[98] Y. Deng, Q. Zhang, S. Tang, L. Zhang, S. Deng, Z. Shi, G. Chen, One-pot synthesis of $ZnFe_2O_4$/C hollow spheres as superior anode materials for lithium-ion batteries, Chem. Commun. 47 (2011) 6828–6830. https://doi.org/10.1039/C0CC05001F.

[99] W. Song, J. Xie, S. Liu, G. Cao, T. Zhu, X. Zhao, Self-assembly of a $ZnFe_2O_4$/graphene hybrid and its application as a high-performance anode material for Li-ion batteries, New J. Chem. 36 (2012) 2236–2241. https://doi.org/10.1039/C2NJ40534B.

[100] R.M. Thankachan, M.M. Rahman, I. Sultana, A.M. Glushenkov, S. Thomas, N. Kalarikkal, Y. Chen, Enhanced lithium storage in $ZnFe_2O_4$–C nanocomposite produced by a low-energy ball milling, J. Power Sources 282 (2015) 462–470. https://doi.org/10.1016/j.jpowsour.2015.02.039.

[101] D. Bresser, E. Paillard, R. Schmuch, S. Krueger, M. Fiedler, R. Schmitz, D. Baither, M. Winter, S. Passerini, Carbon Coated $ZnFe_2O_4$ Nanoparticles for Advanced Lithium-Ion Anodes, Adv. Energy Mater. 3 (2013) 513. https://doi.org/10.1002/aenm.201200735.

[102] P.R. Kumar, P. Kollu, C. Santhosh, K.E.V. Rao, D.K. Kim, A.N. Grace, Enhanced properties of porous $CoFe_2O_4$–reduced graphene oxide composites with alginate binders for Li-ion battery applications, New J. Chem. 38 (2014) 3654–3661. https://doi.org/10.1039/C4NJ00419A.

[103] P. Lavela, J.L. Tirado, M. Womes, J.C. Jumas, Elucidation of Capacity Fading on $CoFe_2O_4$ Conversion Electrodes for Lithium Batteries Based on Mössbauer Spectroscopy, J. Electrochem. Soc. 156 (2009) A589. https://doi.org/10.1149/1.3129691.

[104] S. Ren, X. Zhao, R. Chen, M. Fichtner, A facile synthesis of encapsulated $CoFe_2O_4$ into carbon nanofibres and its application as conversion anodes for lithium-ion batteries, J. Power Sources 260 (2014) 205–210. https://doi.org/10.1016/j.jpowsour.2014.03.012.

[105] Z. Zhang, Y. Wang, M. Zhang, Q. Tan, X. Lv, Z. Zhong, F. Su, Mesoporous $CoFe_2O_4$ nanospheres cross-linked by carbon nanotubes as high-performance anodes for lithium-ion batteries, J. Mater. Chem. A 1 (2013) 7444–7450. https://doi.org/10.1039/C3TA10762K.

[106] Q.Q. Xiong, J.P. Tu, S.J. Shi, X.Y. Liu, X.L. Wang, C.D. Gu, Ascorbic acid-assisted synthesis of cobalt ferrite ($CoFe_2O_4$) hierarchical flower-like microspheres with enhanced lithium storage properties, J. Power Sources 256 (2014) 153–159. https://doi.org/10.1016/j.jpowsour.2014.01.038.

[107] Y. Sharma, N. Sharma, G.V.S. Rao, B.V.R. Chowdari, Lithium recycling behaviour of nano-phase-$CuCo_2O_4$ as anode for lithium-ion batteries, J. Power Sources 173 (2007) 495–501. https://doi.org/10.1016/j.jpowsour.2007.06.022.

[108] C. Zhu, D. Wen, S. Leubner, M. Oschatz, W. Liu, M. Holzschuh, F. Simon, S. Kaskel, A. Eychmüller, Nickel cobalt oxide hollow nanosponges as advanced electrocatalysts for the oxygen evolution reaction, Chem. Commun. 51 (2015) 7851–7854. https://doi.org/10.1039/C5CC01558H.

[109] H. Wang, X. Wang, Growing Nickel Cobaltite Nanowires and Nanosheets on Carbon Cloth with Different Pseudocapacitive Performance, ACS Appl. Mater. Interfaces 5 (2013) 6255–6260. https://doi.org/10.1021/am4012484.

[110] M. Prabu, K. Ketpang, S. Shanmugam, Hierarchical nanostructured $NiCo_2O_4$ as an efficient bifunctional non-precious metal catalyst for rechargeable zinc–air batteries, Nanoscale 6 (2014) 3173–3181. https://doi.org/10.1039/C3NR05835B.

[111] S. Vijayanand, P.A. Joy, H.S. Potdar, D. Patil, P. Patil, Nanostructured spinel $ZnCo_2O_4$ for the detection of LPG, Sens. Actuators B Chem. 152 (2011) 121–129. https://doi.org/10.1016/j.snb.2010.09.001.

[112] Y. Sharma, N. Sharma, G.V. Subba Rao, B.V.R. Chowdari, Nanophase $ZnCo_2O_4$ as a High-Performance Anode Material for Li-Ion Batteries, Adv. Funct. Mater. 17 (2007) 2855–2861. https://doi.org/10.1002/adfm.200600997.

[113] W. Luo, X. Hu, Y. Sun, Y. Huang, Electrospun porous $ZnCo_2O_4$ nanotubes as a high-performance anode material for lithium-ion batteries, J. Mater. Chem. 22 (2012) 8916–8921. https://doi.org/10.1039/C2JM00094F.

[114] B. Liu, J. Zhang, X. Wang, G. Chen, D. Chen, C. Zhou, G. Shen, Hierarchical three-dimensional $ZnCo_2O_4$ nanowire arrays/carbon cloth anodes for a novel class of high-performance flexible lithium-ion batteries, Nano Lett. 12 (2012) 3005–3011. https://doi.org/10.1021/nl300794f.

[115] L. Hu, B. Qu, C. Li, Y. Chen, L. Mei, D. Lei, L. Chen, Q. Li, T. Wang, Facile synthesis of uniform mesoporous $ZnCo_2O_4$ microspheres as a high-performance anode material for Li-ion batteries, J. Mater. Chem. A 1 (2013) 5596–5602. https://doi.org/10.1039/C3TA00085K.

[116] J. Li, J. Wang, D. Wexler, D. Shi, J. Liang, H. Liu, S. Xiong, Y. Qian, Simple synthesis of yolk-shelled $ZnCo_2O_4$ microspheres towards enhancing the electrochemical performance of lithium-ion batteries in conjunction with a sodium carboxymethyl

cellulose binder, J. Mater. Chem. A 1 (2013) 15292–15299. https://doi.org/10.1039/C3TA13787B.

[117] A.K. Rai, T.V. Thi, B.J. Paul, J. Kim, Synthesis of nano-sized $ZnCo_2O_4$ anchored with graphene nanosheets as an anode material for secondary lithium-ion batteries, Electrochimica Acta 146 (2014) 577–584. https://doi.org/10.1016/j.electacta.2014.09.079.

[118] X. Song, Q. Ru, B. Zhang, S. Hu, B. An, Flake-by-flake $ZnCo_2O_4$ as a high-capacity anode material for lithium-ion battery, J. Alloys Compd. 585 (2014) 518–522. https://doi.org/10.1016/j.jallcom.2013.09.182.

[119] S.G. Mohamed, T.F. Hung, C.J. Chen, C.K. Chen, S.F. Hu, R.S. Liu, K.C. Wang, X.K. Xing, H.M. Liu, A.-S. Liu, M.-H. Hsieh, B.-J. Lee, Flower-like $ZnCo_2O_4$ nanowires: toward a high-performance anode material for Li-ion batteries, RSC Adv. 3 (2013) 20143–20149. https://doi.org/10.1039/C3RA42625D.

[120] N. Du, Y. Xu, H. Zhang, J. Yu, C. Zhai, D. Yang, Porous $ZnCo_2O_4$ Nanowires Synthesis via Sacrificial Templates: High-Performance Anode Materials of Li-Ion Batteries, Inorg. Chem. 50 (2011) 3320–3324. https://doi.org/10.1021/ic102129w.

[121] M.-G. Park, D.-H. Lee, H. Jung, J.-H. Choi, C.-M. Park, Sn-Based Nanocomposite for Li-Ion Battery Anode with High Energy Density, Rate Capability, and Reversibility, ACS Nano 12 (2018) 2955–2967. https://doi.org/10.1021/acsnano.8b00586.

[122] R. Zhang, S. Upreti, M.S. Whittingham, Tin-Iron Based Nano-Materials as Anodes for Li-Ion Batteries, J. Electrochem. Soc. 158 (2011) A1498. https://doi.org/10.1149/2.108112jes.

[123] G. Xiao, Y. Wang, J. Ning, Y. Wei, B. Liu, W.W. Yu, G. Zou, B. Zou, Recent advances in IV–VI semiconductor nanocrystals: synthesis, mechanism, and applications, RSC Adv. 3 (2013) 8104–8130. https://doi.org/10.1039/C3RA23209C.

[124] W. Qi, J.G. Shapter, Q. Wu, T. Yin, G. Gao, D. Cui, Nanostructured anode materials for lithium-ion batteries: principle, recent progress and future perspectives, J. Mater. Chem. A 5 (2017) 19521–19540. https://doi.org/10.1039/C7TA05283A.

[125] H. Tian, F. Xin, X. Wang, W. He, W. Han, High-capacity group-IV elements (Si, Ge, Sn) based anodes for lithium-ion batteries, J. Materiomics 1 (2015) 153–169. https://doi.org/10.1016/j.jmat.2015.06.002.

[126] A. Mauger, H. Xie, C.M. Julien, A. Mauger, H. Xie, C.M. Julien, Composite anodes for lithium-ion batteries: status and trends, AIMS Mater. Sci. 3 (2016) 1054–1106. https://doi.org/10.3934/matersci.2016.3.1054.

[127] Y. Xu, Q. Liu, Y. Zhu, Y. Liu, A. Langrock, M.R. Zachariah, C. Wang, Uniform Nano-Sn/C Composite Anodes for Lithium-Ion Batteries, Nano Lett. 13 (2013) 470–474. https://doi.org/10.1021/nl303823k.

[128] L. Yu, L. Qin, X. Xu, K. Kim, J. Liu, J. Kang, K. Ho Kim, $SnSe_x$ (x = 1, 2) nanoparticles encapsulated in carbon nanospheres with reversible electrochemical behaviors for lithium-ion half/full cells, Chem. Eng. J. 431 (2022) 133463. https://doi.org/10.1016/j.cej.2021.133463.

[129] Y. Kim, Y. Kim, Y. Park, Y.N. Jo, Y.-J. Kim, N.-S. Choi, K.T. Lee, SnSe alloy as a promising anode material for Na-ion batteries, Chem. Commun. 51 (2014) 50–53. https://doi.org/10.1039/C4CC06106C.

[130] R. Saroha, A.K. Panwar, Effect of in situ pyrolysis of acetylene (C2H2) gas as a carbon source on the electrochemical performance of $LiFePO_4$ for rechargeable lithium-ion batteries, J. Phys. Appl. Phys. 50 (2017) 255501. https://doi.org/10.1088/1361-6463/aa708c.

[131] A. Gurung, R. Naderi, B. Vaagensmith, G. Varnekar, Z. Zhou, H. Elbohy, Q. Qiao, Tin Selenide – Multi-Walled Carbon Nanotubes Hybrid Anodes for High Performance Lithium-Ion Batteries, Electrochimica Acta 211 (2016) 720–725. https://doi.org/10.1016/j.electacta.2016.06.065.

[132] H. Chen, B.-E. Jia, X. Lu, Y. Guo, R. Hu, R. Khatoon, L. Jiao, J. Leng, L. Zhang, J. Lu, Two-Dimensional $SnSe_2$/CNTs Hybrid Nanostructures as Anode Materials for High-Performance Lithium-Ion Batteries, Chem. – Eur. J. 25 (2019) 9973–9983. https://doi.org/10.1002/chem.201901487.

[133] T. Moon, C. Kim, S.-T. Hwang, B. Park, Electrochemical Properties of Disordered-Carbon-Coated SnO_2 Nanoparticles for Li Rechargeable Batteries, Electrochem. Solid-State Lett. 9 (2006) A408. https://doi.org/10.1149/1.2214332.

[134] D. Lakshmi, B. Nalini, Performance of SnSb:Ce, Co alloy as anode for lithium-ion batteries, J. Solid State Electrochem. 21 (2017) 1027–1034. https://doi.org/10.1007/s10008-016-3456-4.

[135] Y.S. Lee, K.S. Ryu, Study of the lithium diffusion properties and high-rate performance of $TiNb_6O_{17}$ as an anode in lithium secondary battery, Sci. Rep. 7 (2017) 16617. https://doi.org/10.1038/s41598-017-16711-9.

[136] Q. Yu, B. Wang, J. Wang, S. Hu, J. Hu, Y. Li, Flowerlike Tin Diselenide Hexagonal Nanosheets for High-Performance Lithium-Ion Batteries, Front. Chem. 8 (2020). https://doi.org/10.3389/fchem.2020.00590.

[137] R. Saroha, A. Gupta, A.K. Panwar, Electrochemical performances of Li-rich layered-layered Li_2MnO_3-$LiMnO_2$ solid solutions as cathode material for lithium-ion batteries, J. Alloys Compd. 696 (2017) 580–589. https://doi.org/10.1016/j.jallcom.2016.11.199.

[138] Y. Cheng, J. Huang, L. Cao, Y. Wang, Y. Ma, S. Xi, B. Shi, H. Xie, J. Li, Investigation of Electrochemical Performance on $SnSe_2$ and SnSe Nanocrystals as Anodes for Lithium Ions Batteries, Nano 14 (2019) 1950155. https://doi.org/10.1142/S1793292019501558.

[139] X. Cao, A. Li, Y. Yang, J. Chen, ZnSe nanoparticles dispersed in reduced graphene oxides with enhanced electrochemical properties in lithium/sodium ion batteries, RSC Adv. 8 (2018) 25734–25744. https://doi.org/10.1039/C8RA03479F.

[140] N. Ding, J. Xu, Y.X. Yao, G. Wegner, X. Fang, C.H. Chen, I. Lieberwirth, Determination of the diffusion coefficient of lithium ions in nano-Si, Solid State Ion. 180 (2009) 222–225. https://doi.org/10.1016/j.ssi.2008.12.015.

[141] W. Weppner, R.A. Huggins, Determination of the Kinetic Parameters of Mixed-Conducting Electrodes and Application to the System Li3Sb, J. Electrochem. Soc. 124 (1977) 1569. https://doi.org/10.1149/1.2133112.

[142] N. Böckenfeld, A. Balducci, Determination of sodium ion diffusion coefficients in sodium vanadium phosphate, J. Solid State Electrochem. 18 (2014) 959–964. https://doi.org/10.1007/s10008-013-2342-6.

[143] I. Quinzeni, V. Berbenni, D. Capsoni, M. Bini, Ca- and Al-doped $ZnFe_2O4$ nanoparticles as possible anode materials, J. Solid State Electrochem. 22 (2018) 2013–2024. https://doi.org/10.1007/s10008-018-3901-7.

[144] K. Cao, T. Jin, L. Yang, L. Jiao, Recent progress in conversion reaction metal oxide anodes for Li-ion batteries, Mater. Chem. Front. 1 (2017) 2213–2242. https://doi.org/10.1039/C7QM00175D.

[145] N. Sivakumar, S.R.P. Gnanakan, K. Karthikeyan, S. Amaresh, W.S. Yoon, G.J. Park, Y.S. Lee, Nanostructured $MgFe_2O_4$ as anode materials for lithium-ion batteries, J. Alloys Compd. 509 (2011) 7038–7041. https://doi.org/10.1016/j.jallcom.2011.03.123.

[146] D. Feng, H. Yang, X. Guo, 3-Dimensional hierarchically porous $ZnFe_2O_4$/C composites with stable performance as anode materials for Li-ion batteries, Chem. Eng. J. 355 (2019) 687–696. https://doi.org/10.1016/j.cej.2018.08.202.

[147] Z. Fang, L. Zhang, H. Qi, H. Yue, T. Zhang, X. Zhao, G. Chen, Y. Wei, C. Wang, D. Zhang, Nanosheet assembled hollow $ZnFe_2O_4$ microsphere as anode for lithium-ion batteries, J. Alloys Compd. 762 (2018) 480–487. https://doi.org/10.1016/j.jallcom.2018.05.259.

[148] P.F. Teh, S.S. Pramana, Y. Sharma, Y.W. Ko, S. Madhavi, Electrospun $Zn_{1-x}Mn_xFe_2O_4$ Nanofibers as Anodes for Lithium-Ion Batteries and the Impact of Mixed Transition Metallic Oxides on Battery Performance, ACS Appl. Mater. Interfaces 5 (2013) 5461–5467. https://doi.org/10.1021/am400497v.

[149] M. Bini, M. Ambrosetti, D. Spada, $ZnFe_2O_4$, a Green and High-Capacity Anode Material for Lithium-Ion Batteries: A Review, Appl. Sci. 11 (2021) 11713. https://doi.org/10.3390/app112411713.

[150] L. Liao, T. Fang, S. Zhan, D. Weng, Mn-doped Fe_2O_3-$ZnFe_2O_4$ Composites for High Performance Lithium-Ion Battery Anodes, Int. J. Electrochem. Sci. 11 (2016) 8221–8228. https://doi.org/10.20964/2016.10.99.

[151] K.-T. Chen, H.-Y. Chen, C.-J. Tsai, Mesoporous Sn/Mg doped $ZnFe_2O_4$ nanorods as anode with enhanced Li-ion storage properties, Electrochimica Acta 319 (2019) 577–586. https://doi.org/10.1016/j.electacta.2019.06.137.

[152] X. Tang, X. Hou, L. Yao, S. Hu, X. Liu, L. Xiang, Mn-doped $ZnFe_2O_4$ nanoparticles with enhanced performances as anode materials for lithium-ion batteries, Mater. Res. Bull. 57 (2014) 127–134. https://doi.org/10.1016/j.materresbull.2014.05.038.

[153] H. Cheema, V. Yadav, R.S. Maurya, V. Yadav, A. Kumar, N. Sharma, P.A. Alvi, U. Kumar, Structural, optical and electrical properties of Mn-doped $ZnFe_2O_4$ synthesized using sol–gel method, J. Mater. Sci. Mater. Electron. 32 (2021) 23578–23600. https://doi.org/10.1007/s10854-021-06847-w.

[154] G. Padmapriya, A. Manikandan, V. Krishnasamy, S.K. Jaganathan, S.A. Antony, Enhanced Catalytic Activity and Magnetic Properties of Spinel $Mn_xZn_{1-x}Fe_2O_4$ ($0.0 \leq x \leq 1.0$) Nano-Photocatalysts by Microwave Irradiation Route, J. Supercond. Nov. Magn. 29 (2016) 2141–2149. https://doi.org/10.1007/s10948-016-3527-x.

[155] S. Kour, R. Jasrotia, P. Puri, A. Verma, B. Sharma, V.P. Singh, R. Kumar, S. Kalia, Improving photocatalytic efficiency of MnFe2O4 ferrites via doping with Zn_{2+}/La_{3+}

ions: photocatalytic dye degradation for water remediation, Environ. Sci. Pollut. Res. 30 (2023) 71527–71542. https://doi.org/10.1007/s11356-021-13147-7.

[156] M.I.A. Abdel Maksoud, G.S. El-Sayyad, A. Abokhadra, L.I. Soliman, H.H. El-Bahnasawy, A.H. Ashour, Influence of Mg^{2+} substitution on structural, optical, magnetic, and antimicrobial properties of Mn–Zn ferrite nanoparticles, J. Mater. Sci. Mater. Electron. 31 (2020) 2598–2616. https://doi.org/10.1007/s10854-019-02799-4.

[157] R. Sharma, P. Thakur, M. Kumar, P.B. Barman, P. Sharma, V. Sharma, Enhancement in A-B super-exchange interaction with Mn^{2+} substitution in *Mg-Zn* ferrites as a heating source in hyperthermia applications, Ceram. Int. 43 (2017) 13661–13669. https://doi.org/10.1016/j.ceramint.2017.07.076.

[158] A. Ashok, L.J. Kennedy, J.J. Vijaya, Structural, optical and magnetic properties of $Zn_{1-x}Mn_xFe_2O_4$ ($0 \leq x \leq 0.5$) spinel nano particles for transesterification of used cooking oil, J. Alloys Compd. 780 (2019) 816–828. https://doi.org/10.1016/j.jallcom.2018.11.390.

[159] P. Falak, S.A. Hassanzadeh-Tabrizi, A. Saffar-Teluri, Synthesis, characterization, and magnetic properties of ZnO-$ZnFe_2O_4$ nanoparticles with high photocatalytic activity, J. Magn. Magn. Mater. 441 (2017) 98–104. https://doi.org/10.1016/j.jmmm.2017.05.044.

[160] M. Ansari, A. Bigham, S.A. Hassanzadeh-Tabrizi, H. Abbastabar Ahangar, Synthesis and characterization of $Cu_{0.3}Zn_{0.5}Mg_{0.2}Fe_2O_4$ nanoparticles as a magnetic drug delivery system, J. Magn. Magn. Mater. 439 (2017) 67–75. https://doi.org/10.1016/j.jmmm.2017.04.084.

[161] S.A. Hassanzadeh-Tabrizi, S. Behbahanian, J. Amighian, Synthesis and magnetic properties of $NiFe_{2-x}Sm_xO_4$ nanopowder, J. Magn. Magn. Mater. 410 (2016) 242–247. https://doi.org/10.1016/j.jmmm.2016.03.015.

[162] A. Aridi, R. Awad, A. Khalaf, Synthesis and characterization of $ZnFe_2O_4$/ Mn_2O_3 nanocomposites, Appl. Phys. A 127 (2021) 206. https://doi.org/10.1007/s00339-021-04362-7.

[163] P. Samoila, C. Cojocaru, I. Cretescu, C.D. Stan, V. Nica, L. Sacarescu, V. Harabagiu, Nanosized Spinel Ferrites Synthesized by Sol-Gel Autocombustion for Optimized Removal of Azo Dye from Aqueous Solution, J. Nanomater. 2015 (2015) 1–13. https://doi.org/10.1155/2015/713802.

[164] A. Jain, A.K. Panwar, P.K. Tyagi, Effect of Cr doping on $Li_2ZnTi_3O_8$ as alternative anode material to enhance electrochemical properties of lithium-ion batteries, Appl. Phys. A 128 (2022) 302. https://doi.org/10.1007/s00339-022-05440-0.

[165] M. Qayoom, R. Bhat, K. Asokan, M.A. Shah, G.N. Dar, Unary doping effect of A^{2+} (A = Zn, Co, Ni) on the structural, electrical and magnetic properties of substituted iron oxide nanostructures, J. Mater. Sci. Mater. Electron. 31 (2020) 8268–8282. https://doi.org/10.1007/s10854-020-03362-2.

[166] R. Saroha, A.K. Panwar, Y. Sharma, Physicochemical and electrochemical performance of $LiFe_{1-x}Ni_xPO_4$ ($0 \leq x \leq 1.0$) solid solution as potential cathode material for rechargeable lithium-ion battery, Ceram. Int. 43 (2017) 5734–5742. https://doi.org/10.1016/j.ceramint.2017.01.115.

[167] Z. Li, J. Nie, J. Zhao, S. Yao, J. Wang, X. Feng, Prussian blue-derived transition metal oxide $ZnO/ZnFe_2O_4$ microcubes as anode materials for lithium-ion batteries, J. Mater. Sci. Mater. Electron. 30 (2019) 21416–21424. https://doi.org/10.1007/s10854-019-02520-5.

[168] J. Yao, Y. Li, J. Yan, J. Jiang, S. Xiao, $ZnFe_2O_4$ nanoparticles imbedding in carbon prepared from leaching liquor of jarosite residue as anode material for lithium-ion batteries, Ionics 26 (2020) 4373–4380. https://doi.org/10.1007/s11581-020-03583-9.

[169] Q. Wang, Y. Wu, N. Pan, C. Yang, S. Wu, D. Li, S. Gu, G. Zhou, J. Chai, Preparation of rambutan-like $Co_{0.5}Ni_{0.5}Fe_2O_4$ as anode for high–performance lithium–ion batteries, Front. Chem. 10 (2022). https://doi.org/10.3389/fchem.2022.1052560.

[170] C. Wang, Y. Li, Y. Ruan, J. Jiang, Q.-H. Wu, $ZnFe_2O_4$-nanocrystal-assembled microcages as an anode material for high performance lithium-ion batteries, Mater. Today Energy 3 (2017) 1–8. https://doi.org/10.1016/j.mtener.2016.12.001.

[171] Y. Qu, D. Zhang, X. Wang, H. Qiu, T. Zhang, M. Zhang, G. Tian, H. Yue, S. Feng, G. Chen, Porous $ZnFe_2O_4$ nanospheres as anode materials for Li-ion battery with high performance, J. Alloys Compd. 721 (2017) 697–704. https://doi.org/10.1016/j.jallcom.2017.06.031.

[172] A.S. Hameed, H. Bahiraei, M.V. Reddy, M.Z. Shoushtari, J.J. Vittal, C.K. Ong, B.V.R. Chowdari, Lithium Storage Properties of Pristine and (Mg,Cu) Codoped $ZnFe_2O_4$ Nanoparticles, ACS Appl. Mater. Interfaces 6 (2014) 10744–10753. https://doi.org/10.1021/am502605s.

[173] A.K. Rai, J. Gim, L.T. Anh, J. Kim, partially reduced Co_3O_4/graphene nanocomposite as an anode material for secondary lithium-ion battery, Electrochimica Acta 100 (2013) 63–71. https://doi.org/10.1016/j.electacta.2013.03.140.

[174] L. Guo, Q. Ru, X. Song, S. Hu, Y. Mo, Pineapple-shaped $ZnCo_2O_4$ microspheres as anode materials for lithium-ion batteries with prominent rate performance, J. Mater. Chem. A 3 (2015) 8683–8692. https://doi.org/10.1039/C5TA00830A.

[175] Y. Qiu, S. Yang, H. Deng, L. Jin, W. Li, A novel nanostructured spinel $ZnCo_2O_4$ electrode material: morphology conserved transformation from a hexagonal shaped nano disk precursor and application in lithium-ion batteries, J. Mater. Chem. 20 (2010) 4439–4444. https://doi.org/10.1039/C0JM00101E.

[176] J. Bai, X. Li, G. Liu, Y. Qian, S. Xiong, Unusual Formation of $ZnCo_2O_4$ 3D Hierarchical Twin Microspheres as a High-Rate and Ultralong-Life Lithium-Ion Battery Anode Material, Adv. Funct. Mater. 24 (2014) 3012–3020. https://doi.org/10.1002/adfm.201303442.

[177] V. Venkatachalam, A. Alsalme, A. Alghamdi, R. Jayavel, Hexagonal-like $NiCo_2O_4$ nanostructure based high-performance supercapacitor electrodes, Ionics 23 (2017). https://doi.org/10.1007/s11581-016-1868-x.

[178] A. Nedunchezhian, S. Duraisamy, R. Rajavel, N. Devi, K. Maeda, M. Arivanandhan, K. Fujiwara, G. Anbalagan, R. Jayavel, Enhancing the thermoelectric power factor of nanostructured $ZnCo_2O_4$ by Bi substitution, RSC Adv. 10 (2020) 18769–18775. https://doi.org/10.1039/D0RA01542C.

[179] X. Xuechun, G. Wang, M. Zhang, Z. Wang, Z. Rongjun, Y. Wang, Electrochemical performance of mesoporous $ZnCo_2O_4$ nanosheets as an electrode material for supercapacitor, Ionics 24 (2018). https://doi.org/10.1007/s11581-017-2354-9.

[180] L. Wang, D. Li, J. Zhang, C. Song, H. Xin, X. Qin, Porous flower-like $ZnCo_2O_4$ and $ZnCo_2O_4$@C composite: a facile controllable synthesis and enhanced electrochemical performance, Ionics 26 (2020) 1–9. https://doi.org/10.1007/s11581-020-03609-2.

[181] S. Chakrabarty, A. Mukherjee, wei-nien su, S. Basu, improved bi-functional ORR and OER catalytic activity of reduced graphene oxide supported $ZnCo_2O_4$ microsphere, Int. J. Hydrog. Energy 44 (2018). https://doi.org/10.1016/j.ijhydene.2018.11.163.

[182] S. Mu, P. Ramesh, D. Geetha, K. Ravikumar, H. Elhosiny Ali, H. Algarni, P. Soundhirarajan, K. Chandekar, M. Shkir, A Facile Preparation of Zinc Cobaltite ($ZnCo_2O4$) Nanostructures for Promising Supercapacitor Applications, J. Inorg. Organomet. Polym. Mater. 31 (2021). https://doi.org/10.1007/s10904-021-02077-z.

[183] L. Zhang, J. Zheng, P. Dou, W. Wang, J. Cheng, X. Xu, Bubble-induced lychee-shaped hollow $ZnCo_2O_4$@polypyrrole/sodium alginate ternary microsphere as novel anode

materials for lithium-ion batteries, J. Mater. Sci. Mater. Electron. 28 (2017) 1–9. https://doi.org/10.1007/s10854-017-6806-9.

[184] L. Zhang, S. Zhu, X. Li, H. Fang, L. Wang, Y. Song, X. Jia, 3D porous $ZnCo_2O_4$@NiO on nickel foam as advanced electrodes for lithium storage, Ionics 26 (2020). https://doi.org/10.1007/s11581-019-03355-0.

[185] X. Yang, P. Wang, Y. Tang, C. Peng, Y. Lai, J. Li, Z. Zhang, Bimetallic ZIF–derived polyhedron $ZnCo_2O_4$ anchored on the reduced graphene oxide as an anode for sodium-ion battery, Ionics 25 (2019) 2945–2950. https://doi.org/10.1007/s11581-019-02982-x.

[186] Q. Gan, K. Zhao, S. Liu, Z. He, MOF-derived carbon coating on self-supported $ZnCo_2O_4$–ZnO nanorod arrays as high-performance anode for lithium-ion batteries, J. Mater. Sci. 52 (2017) 1–13. https://doi.org/10.1007/s10853-017-1043-4.

[187] X. Tan, Y. Wu, X. Lin, A. Zeb, X. Xu, Y. Luo, J. Liu, Application of MOF-derived transition metal oxides and composites as anodes for lithium-ion batteries, Inorg. Chem. Front. 7 (2020) 4939–4955. https://doi.org/10.1039/D0QI00929F.

[188] S.K. Behera, Facile synthesis and electrochemical properties of Fe_3O_4 nanoparticles for Li ion battery anode, J. Power Sources 196 (2011) 8669–8674. https://doi.org/10.1016/j.jpowsour.2011.06.067.

[189] H. Lv, X. Feng, H. Bi, X. Song, Anemone-shaped Fe_3O_4 Micro-structures as the Anode Materialsin High Electrochemical PerformanceLi-ion Batteries, Int. J. Electrochem. Sci. 17 (2022) 220663. https://doi.org/10.20964/2022.06.70.

[190] F. Di Lupo, A. Tuel, C. Francia, G. Meligrana, S. Bodoardo, C. Gerbaldi, Tunable Ordered Nanostructured α-Fe_2O_3 Lithium Battery Anodes by Nanocasting Technique Using SBA-15 Hard Silica Templates, Int. J. Electrochem. Sci. 7 (2012) 10865–10883. https://doi.org/10.1016/S1452-3981(23)16909-4.

[191] X. Liu, N. Wu, C. Cui, P. Zhou, Y. Sun, Enhanced rate capability and cycling stability of core/shell structured $CoFe_2O_4$/onion-like C nanocapsules for lithium-ion battery anodes, J. Alloys Compd. 644 (2015) 59–65. https://doi.org/10.1016/j.jallcom.2015.04.097.

[192] Y. Hwangbo, J.-H. Yoo, Y. Lee, Electrospun $CoFe_2O_4$ nanofibers as high-capacity anode materials for Li-Ion batteries, J. Nanosci. Nanotechnol. 17 (2017) 7632–7635. https://doi.org/10.1166/jnn.2017.14763.

[193] H. Wang, D. Liu, Y. Li, Q. Duan, Single-spinneret electrospinning fabrication of $CoFe_2O_4$ nanotubes as high-performance anode materials for lithium-ion batteries, Mater. Lett. 172 (2016) 64–67. https://doi.org/10.1016/j.matlet.2016.02.133.

[194] Z.H. Li, T.P. Zhao, X.Y. Zhan, D.S. Gao, Q.Z. Xiao, G.T. Lei, High capacity three-dimensional ordered macroporous CoFe2O4 as anode material for lithium-ion batteries, Electrochimica Acta 55 (2010) 4594–4598. https://doi.org/10.1016/j.electacta.2010.03.015.

[195] X. Sun, X. Zhu, X. Yang, J. Sun, Y. Xia, D. Yang, $CoFe_2O_4$/carbon nanotube aerogels as high-performance anodes for lithium-ion batteries, Green Energy Environ. 2 (2017) 160–167. https://doi.org/10.1016/j.gee.2017.01.008.

[196] S. Ren, X. Zhao, R. Chen, M. Fichtner, Carbon-Nanofibers Encapsulated Metal Oxide Nanocomposite and Its Application as Conversion Anode Material for Lithium-Ion Batteries, ECS Trans. 64 (2015) 155. https://doi.org/10.1149/06422.0155ecst.

[197] L. Wang, L. Zhuo, C. Zhang, F. Zhao, Carbon dioxide-induced homogeneous deposition of nanometer-sized cobalt ferrite ($CoFe_2O_4$) on graphene as high-rate and cycle-stable anode materials for lithium-ion batteries, J. Power Sources 275 (2015) 650–659. https://doi.org/10.1016/j.jpowsour.2014.11.051.

[198] L. Zhang, T. Wei, Z. Jiang, C. Liu, H. Jiang, J. Chang, L. Sheng, Q. Zhou, L. Yuan, Z. Fan, Electrostatic interaction in electrospun nanofibers: Double-layer carbon protection of $CoFe_2O_4$ nanosheets enabling ultralong-life and ultrahigh-rate lithium-ion storage, Nano Energy 48 (2018) 238–247. https://doi.org/10.1016/j.nanoen.2018.03.053.

[199] Mubasher, M. Mumtaz, M. Hassan, S. Ullah, Z. Ahmad, Nanohybrids of multi-walled carbon nanotubes and cobalt ferrite nanoparticles: High performance anode material for lithium-ion batteries, Carbon 171 (2021) 179–187. https://doi.org/10.1016/j.carbon.2020.08.080.

[200] B. Rani, N.K. Sahu, Electrochemical properties of $CoFe_2O_4$ nanoparticles and its rGO composite for supercapacitor, Diam. Relat. Mater. 108 (2020) 107978. https://doi.org/10.1016/j.diamond.2020.107978.

[201] S. Permien, S. Indris, G. Neubüser, A. Fiedler, L. Kienle, S. Zander, S. Doyle, B. Richter, W. Bensch, The Role of Reduced Graphite Oxide in Transition Metal Oxide Nanocomposites Used as Li Anode Material: An Operando Study on $CoFe_2O_4$/rGO, Chem. – Eur. J. 22 (2016) 16929–16938. https://doi.org/10.1002/chem.201603160.

[202] M. Zhao, J. Xiong, Y. Yang, J. Zhao, Template-Assisted Synthesis of Honeycomb-Like $CoFe_2O_4$/CNTs/rGO Composite as Anode Material for Li/Na-Ion Batteries, ChemElectroChem 6 (2019) 3468–3477. https://doi.org/10.1002/celc.201900800.

[203] P. Seal, C. Borgohain, N. Paul, P.D. Babu, J. Prasad borah, Effect of Annealing in tuning Magnetic Hyperthermic Efficiency of MWCNT/CoFe2O4 Nanocomposites, J. Phys. Appl. Phys. 53 (2020). https://doi.org/10.1088/1361-6463/ab8de5.

[204] A. Meidanchi, Cobalt ferrite nanoparticles supported on reduced graphene oxide sheets: optical, magnetic and magneto-antibacterial studies, Nanotechnology 31 (2020) 445704. https://doi.org/10.1088/1361-6528/aba7e2.

[205] H. Ngo, H. Nguyen, H. Le, T. Le, T. Vu, K. Pham, T. Phung, Enhancement of electrochemical properties of porous rGO by controlled growth $CoFe_2O_4$ nanoparticles, J. Mater. Sci. Mater. Electron. 34 (2023). https://doi.org/10.1007/s10854-023-11071-9.

[206] C. Wu, J. Wang, Q. Deng, M. Li, K. Jiang, L. Shang, Z. Hu, J. Chu, Pseudocapacitive Li-ion storage boosts high-capacity and long-life performance in multi-layer $CoFe_2O_4$/rGO/C composite, Nanotechnology 30 (2018) 045401. https://doi.org/10.1088/1361-6528/aaed56.

[207] Y. Xiao, X. Li, J. Zai, K. Wang, Y. Gong, B. Li, Q. Han, X. Qian, $CoFe_2O_4$-Graphene Nanocomposites Synthesized through An Ultrasonic Method with Enhanced Performances as Anode Materials for Li-ion Batteries, Nano-Micro Lett. 6 (2014) 307–315. https://doi.org/10.1007/s40820-014-0003-7.